Second-Epoch, High-Resolution Observations of a

Low-Redshift Radio Quasar Sample

by

Matthew Leigh Lister

B.Sc., University of Toronto, 1991

A Thesis Submitted in Partial Fulfillment of the

Requirements for the Degree of

MASTER OF SCIENCE

in the Department of Physics and Astronomy

We accept this thesis as conforming to the required standard

[redacted]

Dr. A.C. Gower, Supervisor (Department of Physics and Astronomy)

[redacted]

Dr. C.J. Pritchet, Departmental Member (Department of Physics and Astronomy)

[redacted]

Dr. J.B. Hutchings, Outside Member (Dominion Astrophysical Observatory)

[redacted]

Dr. R. A. Ring, Outside Member (Department of Biology)

[redacted]

Dr. T.K. Menon, External Examiner (University of British Columbia)

University of Victoria

Supervisor: Dr. Ann C. Gower

Abstract

Second-epoch VLA observations made at 2 and 6 cm are presented for a sample of 38 low-redshift radio loud quasars. The sample, first observed by Gower and Hutchings (1984), contains a variety of source morphologies, including classical double-lobed, one-sided, and compact structures, and has extensive optical data published by John Hutchings.

Variability of the central core component at 6 cm is examined and found to be present in 9 out of 23 double-sided sources, 0 out of 6 one-sided sources, and 3 out of 4 core-dominated sources. No apparent differences in the spectral index distributions of the variable and non-variable cores were found. This is most likely due to the inclusion of weak ($< 10^{24.5}$ W Hz^{-1} at 6 cm), variable cores in the sample, all of which had steep spectral indices.

It is currently unclear to what extent the observed properties of radio quasars are affected by orientation and relativistic beaming effects, with some authors proposing that quasars are objects lying close to the line of sight (eg. Barthel 1989). Numerical modelling experiments are carried out which show that many of the morphological properties of this class can be explained by a randomly-oriented quasar sample containing a bias which excludes objects lying near the plane of the sky.

The ratio of core to extended luminosity, generally considered to be a strong indicator of beaming, is shown not to correlate with the orientation of the lobe structure, but rather is found to be consistent with the evolutionary scheme of Hutchings, Price and Gower(1988). No correlations between this luminosity ratio and core variability were found.

Correlations were found between the radio core luminosity and host galaxy/nuclear magnitudes, with a weaker correlation found between radio core luminosity and host galaxy colour. The ratio of the optical luminosity of the nucleus to that of the host galaxy was not found to correlate with the other radio properties of the sample.

Finally, the high-resolution maps made at 1.3 and 2 cm reveal examples of small-scale structure in several sources that would be good candidates for VLBI study.

Examiners:

Dr. A.C. Gower, Supervisor (Department of Physics and Astronomy)

Dr. C.J. Pritchet, Departmental Member (Department of Physics and Astronomy)

Dr. J.B. Hutchings, External Member (Dominion Astrophysical Observatory)

Dr. R. A. Ring, Outside Member (Department of Biology)

Dr. T.K. Menon, External Examiner (University of British Columbia)

Contents

List of Tables

List of Figures

Acknowledgements

I would like to thank everyone in the astronomy department and especially the Blue Stragglers for making my stay in Victoria so enjoyable. I owe special thanks to Ann Gower and John Hutchings for their time spent in making helpful suggestions during the writing of this thesis, and am also greatly appreciative of the support given to me by Don Vanden-Berg, David Hartwick, and Chris Pritchet.

Chapter One:

Introduction

1.1. Historical Overview

The history of radio quasar research has followed a trend common to many branches of astronomy, in that advances in understanding have nearly always been a result of advances in technology. For millennia, astronomical research had been based only on observations of the visible part of the electromagnetic spectrum, but this limitation disappeared in the 1930's and 40's with the development of radio astronomy by Karl Jansky and others. Early observations made in the 1950's with radio telescopes in Great Britain, Australia, and the United States revealed for the first time a radio sky that was dominated by two objects: our own galaxy and the sun.

In addition to these bright sources, a large number of fainter, compact objects were discovered to be scattered randomly across the sky. A few of these sources were found to be associated with supernova remnants (e.g. the Crab Nebula, Cassiopeia A), or galaxies (e.g. M87, Cygnus A, Centaurus A); however, the majority of these compact objects could not be identified at optical wavelengths due to uncertainties in their absolute sky positions. The situation was soon improved by the construction of multi-element interferometers by Sir Martin Ryle at Cambridge and others in the late 50's and early 1960's. The superior resolving power of this class of instrument led to the discovery that many of the compact radio sources in fact had extended structures composed of two diametrically-opposed radio-emitting lobes. Meanwhile, searches at optical wavelengths using the newly-obtained source positions had revealed that some of the sources were associated with unresolved, stellar-like objects.

One of these sources, 3C 273, caused an immense deal of excitement in 1963 when Martin Schmidt discovered it to have a redshift of $z = 0.16$, implying that it was as far away from us as other distant galaxies. Since 3C 273 had an apparent visual magnitude

similar to other stars in our galaxy, this finding meant that it was extremely luminous. Furthermore, analysis of historical light curves showed that it was highly variable, which from light-travel-time arguments suggested that it also had a very small intrinsic diameter. As other observations of these 'quasi-stellar' radio sources began to indicate that they had similar properties to 3C 273, the name was shortened to 'quasar' and a new class of object was recognized.

The birth of quasar astronomy posed a formidable challenge for theorists of the day, as it was difficult to imagine how the most luminous objects in the universe could create so much radiation in such a small volume. An important clue to the puzzle was provided by the broad emission-line features seen in the spectra of quasars. The width and strength of these lines implied that quasars contained vast amounts of hot gas moving at high velocity. This observation, combined with the need for a very efficient means of releasing energy from matter, led theorists to conclude that the source of energy had to be gravitational.

The model for the central 'engine' of a quasar that has survived to this day consists of a super-massive black hole of $\sim 10^8$ solar masses, surrounded by a massive accretion region of hot gas (Rees 1984). As matter flows into the central region, it will likely have some initial angular momentum, and will settle into a rotating accretion disk around the black hole. This disk will soon heat up and expand due to the viscosity of the gas, and some of its gravitational potential energy will be released in the form of radiation. The final shape of the accretion region is thought to be toroidal or 'doughnut'-shaped. The hole of this torus is aligned with the spin axis of the accretion disk, and corresponds to the region where particles can either be accelerated out of or drawn into the vicinity of the central black hole by virtue of their low angular momentum.

The introduction of the accretion-disk model also provided a very good explanation for the double-lobe structures seen in radio-loud galaxies and quasars. Since the time of their discovery, it was realized that the lobes required a continuous, stable power supply to sustain their large luminosity. In 1971, Martin Rees had suggested that the lobes were re-supplied by a continuous stream of particles from a central source, but it was not until 1974 that Roger Blandford and Martin Rees incorporated this idea into the accretion disk

model. They proposed that the hole of the torus could provide a channel in which electrons could be accelerated out of the nuclear region by a strong electric field aligned perpendicular to the accretion disk. The flow would be highly collimated, and would travel away from the quasar until it reached the dense intergalactic medium, where it would disrupt and form a radio lobe.

In the years since it was first proposed, strong evidence has been gathered in support of the accretion disk / jet model with the help of several new radio telescopes and observational techniques.

The first of these was Very Long Baseline Interferometry (VLBI), a technique by which data from different telescopes, scattered around the surface of the earth, are combined to make radio images. The advantage of this method is that the very large antenna separations allow details on the milliarcsecond scale to be resolved. Early VLBI observations of the central regions of radio galaxies and quasars showed that they consisted of a bright, stationary 'core' component, and a series of equally bright, expanding components, all moving away from the core in a preferred direction. The latter features were found to have the interesting property that they were apparently moving faster than the speed of light. Various explanations for this 'superluminal motion' phenomenon were put forward, but the model which has survived is that of Rees (1967), who proposed that superluminal motion was merely a line-of-sight effect caused by the finite speed of light. If the expanding components are travelling at relativistic speeds very close to the line of sight, they will be continuously chasing the light signals that they emitted when there were at a previous position. To an observer on Earth therefore, signals emitted by a component at two different positions will arrive very closely spaced in time, and the component will appear to 'jump' very rapidly between them.

The existence of superluminal motion provided a strong pillar for the accretion disk / jet model, as it implied the existence of extremely energetic matter flows (jets) in the central regions of radio galaxies and quasars. True confirmation of these jets did not come until many years later, with the construction of the Very Large Array (VLA) telescope (see Chapter 2) in 1980. Hints of large, kiloparsec-scale jets had been previously been

observed in sources such as M87 (Turland 1975), but the high signal-to-noise, high-resolution images made with the VLA revealed that large scale jets were in fact quite common features in extragalactic radio sources.

The commissioning of the VLA brought with it a new era in the study of radio quasars. For the first time, the complex morphology of radio lobes could be studied in detail, and the heightened sensitivity of the maps allowed the detection of faint central cores previously unseen in many sources.

It is in these cores that the accretion disk and central engine are believed to reside. Observations made at various wavelengths have shown that the spectra of the majority of cores can be described by a power law of the form $S_\nu \propto \nu^\alpha$, where S_ν is the flux at frequency ν, and α is the spectral index. This power law is thought to reflect the energy distribution of the relativistic electrons in the core. These electrons are responsible for most of the quasar's energy output at radio wavelengths as they spiral around strong magnetic field lines, giving off synchrotron radiation.

The observed spectral indices of the core components span a wide range, and often vary for individual sources as one moves to higher or lower wavelength regions of the spectrum. Some sources display steep spectra with $\alpha < 0$, which would be expected of a simple power-law distribution of electrons that decays with increasing energy. However, there are a great many sources that display flat ($\alpha \approx 0$) or inverted $\alpha > 0$ spectra which are most likely due to opacity effects in the core. The most important of these effects is synchrotron self-absorption (also called the synchrotron self-Compton process) in which the synchrotron photons are boosted to high energies following collisions with the relativistic electrons. The existence of this process has led to the so-called 'brightness temperature problem', which is concerned with differences between the predicted and observed x-ray fluxes for many radio quasars. The current status of this problem, along with a possible solution, will be discussed in Chapter 4.

The radiation from the extended, lobe components is also believed to be synchrotron in origin. These structures are generally observed to have similar spectral indices (approximately, $\alpha \approx -0.8$, Kellermann and Owen 1988).

Early VLA studies of large samples of radio quasars (e.g. Hintzen and Owen 1981, Neff 1982a, Hintzen, Ulvestad and Owen 1983) revealed a large variety of lobe morphologies. Instead of having the classical lobe-core-lobe or 'triple' structure, many sources were found to be either embedded in large haloes or possessed a radio lobe on one side of the core only. Others showed no signs of any extended structure, and were composed entirely of an unresolved core component.

These different morphological classes are thought to be the result of both orientation and evolutionary effects. Hutchings, Price and Gower (1988) have found evidence for an evolutionary scenario in which radio quasars start out as core-dominated, a radio lobe forms on one side, and then the other side, while the core continuously fades. Since quasars in this model would have a wide range of linear sizes, it is not feasible to 'de-project' the observed angular sizes of individual sources to determine their orientation.

In spite of the uncertainties regarding the relative importance of intrinsic source evolution and orientation, there appears to be at least one class of object where we know the viewing angle to the source, namely the BL Lacertae objects. BL Lacs have very similar properties to normal radio quasars, with the notable exception that they do not possess broad emission-line features in their optical spectra. They are also distinguished as a class by their strong variability at all wavelengths, high degree of optical polarization and their core-dominated radio structure. These characteristics have led many researchers to come to the conclusion that BL Lacs are oriented in such a way that we are looking down through the hole in the accretion disk into the central engine itself.

There are many important consequences of this conclusion, the first of which being the high probability of superluminal motion occurring in these sources. So far, this has been observed in five objects of this class, including the prototype source BL Lacertae. The second important effect is that the radiation from the core will be greatly enhanced by a Dop-

pler beaming effect. This effect, which will be discussed in more detail in Chapter 4, is due to the relativistic velocity of the jet flow. Relativistic aberration causes radiation to be preferentially swung forward towards the flow direction in the observer's frame, so to an observer looking down the jet the flux will be greatly amplified. Since the radiation from the lobes does not originate in a collimated, relativistic flow, it is not predicted to be affected by this effect. Therefore the ratio of core to extended flux, or 'core fraction', will be higher for beamed sources, which is generally true of BL Lacs (Antonucci and Ulvestad 1985). Finally, the variability timescale of the core will appear to be much shorter due to the same effects responsible for superluminal motion.

The interpretation of BL Lacs as beamed objects has led to considerable debate over the 'unified scheme' of Barthel (1989). He suggested that radio galaxies and radio-loud quasars are in fact the same object, but appear different only due to beaming and orientation effects. Radio quasars, having generally stronger cores and smaller apparent sizes, would be objects aligned near the line of sight, with BL Lacs representing the cases of extreme alignment. Radio galaxies meanwhile would lie much closer to the plane of the sky and would tend to be seen face on. Although the relative number densities of these objects tend to support this scheme, there have been legitimate concerns raised over how beaming may have altered the number counts in the flux-limited surveys that are used to find extragalactic radio sources. Additionally, the unified model has had trouble reconciling observed differences in some properties of the two populations that are expected to be orientation-independent.

One such property involves the host galaxies of quasars. For many years very little was known about the immediate environments of quasar nuclei. Optical observations of radio galaxies and faint nebulosities around sources such as 3C 273 had suggested that quasars resided at the center of average-luminosity galaxies, but it was not until the early 1980's that definite proof was obtained (Hutchings *et al.* 1981, Wyckoff *et al.* 1981). The host galaxies were found to have a variety of morphologies, including elliptical, spiral, and distorted structures. Many sources also showed signs of interaction with other galax-

ies, which has widely been interpreted as a means of triggering nuclear activity in quasars (Hutchings and Neff, 1990).

The reasons why only a small fraction of galaxies appear to have active nuclei have yet to be fully understood. In particular, it is unknown why only $\sim 10\%$ of all quasars are found to be radio-loud, with the rest having the bulk of their luminosity at optical , and/or x-ray wavelengths. To fully explain the connection between the optical and radio activity of quasars, a large set of high-quality observations is required. The VLA has been an invaluable tool in this regard at radio wavelengths, but there are still many technological difficulties that limit progress on the optical side. The effects of atmospheric seeing, combined with the enormous luminosity contrast between the host galaxy and the active core region make it extremely difficult to obtain high-quality optical images of quasars. The situation is improving however with the current advances in telescope design and adaptive optics methods. The Hubble Space Telescope will no doubt provide an excellent means of probing the interior regions of active galaxies once it receives its optical correction package, as the observation of an accretion disk structure in the nucleus of the radio galaxy 3C 270 with this instrument has recently shown (Ford *et al.*, 1993)

1.2. Thesis Outline

As we have seen, there are many interesting, unanswered questions in the field of radio quasars that still need to be addressed, which made it somewhat difficult to decide which areas to focus on in this thesis. The data that were kindly made available to me by Ann Gower consisted of a series of second-epoch VLA observations made in 1984 of the core components of a sample of roughly 40 low-redshift quasars. In addition to being a well-representative sample of the low-z population, many of the objects had been optically imaged by John Hutchings using the Canada France Hawaii Telescope. Although Gower and Hutchings (1984) originally explored correlations between their first epoch VLA data taken in 1982 and the optical properties, since that time newer, more accurate optical data have been published. Their work also focussed more on the extended, lobe structures of

the sample objects since the original VLA observations were made at longer wavelengths that are more sensitive to these features (see Chapter 2).

With these optical and two-epoch radio data at my disposal, I have decided to concentrate on three separate aspects of the low-z sample.

Very few studies to date have focussed on the variability and spectral indices of low-luminosity radio cores, making the radio data for this sample extremely valuable in this regard. In Chapter 4 I investigate the variability properties of these sources and discuss the possible implications they have on the relativistic beaming model.

Chapter 5 is concerned with the effects of orientation on the observed properties of radio quasars. By using simple numerical models, I show how radio-lobe morphology can be used as a statistical indicator of orientation, and provide evidence that quasars may be in fact be objects that are seen close to the line of sight. In Chapter 6, I use the results of these experiments to investigate the usefulness of the core fraction statistic as an indicator of relativistic beaming.

For the last part of my investigation, in Chapter 7 I re-assess the findings of Gower and Hutchings (1984) using the new optical data, and look for new correlations between the optical and radio properties of the sample.

Finally, in Appendix A I present optical and radio maps and discuss new details in the small-scale morphology of some sources that were revealed by the higher resolution of the 2 cm VLA data.

Chapter Two:

Introduction to Radio Astronomical Concepts

The data presented in this thesis were obtained with the Very Large Array (VLA), a radio telescope operated by the National Radio Astronomy Observatory[1]. The concepts of interferometry upon which the VLA is based are somewhat different from conventional astronomical imaging techniques, and may be unfamiliar to some readers.

The purpose of this chapter, therefore, is to provide background material that will be useful for interpreting the description and analysis of the data presented in later chapters. Much of the material that will described here has been adapted from Perley, Schwab and Bridle (1989), and the reader is referred to this book for a more detailed discussion.

2.1. The Very Large Array

The VLA was built in 1980 by the National Science Foundation and consists of twenty-seven antennas 25 meters in diameter placed in a Y configuration on a large plateau in central New Mexico, USA (Figure 2.1). Like most other aperture synthesis interferometers, the antennas are movable, providing observers with different configurations depending on the type of observations required.

There are four basic configurations for the VLA, named A,B,C and D in order of increasing compactness. The A configuration provides a maximum antenna separation of 36.4 km, and is used to map small scale (arc-second) structure in galactic and extra-galactic radio sources. As one moves to more compact configurations such as C and D, the array becomes more sensitive to faint, extended-type emission at the expense of losing resolution. The resolution that can be attained with an interferometer is generally mea-

1. The National Radio Astronomy Observatory is operated by Associated Universities Inc., under co-operative agreement with the National Science Foundation.

sured in terms of the half-power beamwidth θ, which is directly proportional to λ / D, where λ is the observing wavelength and *D* is the maximum antenna spacing. θ is also referred to simply as the 'beam', and represents the smallest structure size that can be imaged with the VLA. If a source has features smaller than this angular diameter, they will be smeared out to this resolution. Just as the largest baselines of an interferometer limit the

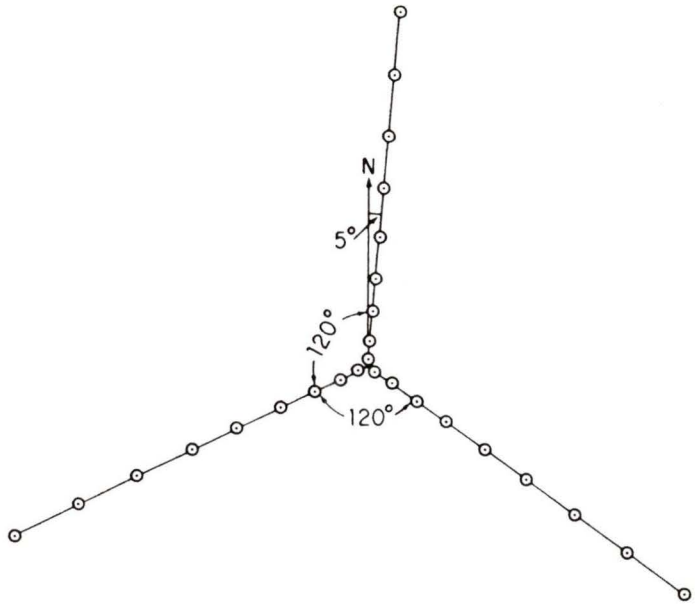

Figure 2.1: The Very Large Array

Source: Perley, Schwab and Bridle (1989)

resolution that can be achieved, the shortest baselines place an upper limit on the largest size structure that can be seen on the sky. Any structures larger than those listed for each configuration in Table 2.1 will be invisible to the VLA. This phenomenon, unique to interferometers, can greatly change the appearance of a radio map depending on what configuration is used. Great care must therefore be taken when interpreting VLA images.

Table 2.1: VLA Configuration Summary

	A	B	C	D
Max. Antenna Separation (km)	36.4	11.4	3.4	1.03
Min. Antenna Separation (km)	0.68	0.21	0.073	0.033
Approximate Resolution (Half-Power Beamwidth)				
20 cm	1.4"	3.9"	12.5"	44"
6 cm	0.4"	1.2"	3.9"	14"
2 cm	0.14"	0.4"	1.2"	3.9"
1.3 cm	0.08"	0.3"	0.9"	2.8"
Approximate Largest Structure Scale Structure "Visible" to the VLA				
20 cm	38"	2'	7'	15'
6 cm	10"	36"	2'	5'
2 cm	4"	12"	40"	90"
1.3 cm	2"	7"	25"	60"

Source: Perley (1992)

Notes on Table 2.1:

- Half-Power beamwidths are for a full-synthesis, uniformly weighted map of a source at zenith with no taper.

2.2. The Interferometer

An interferometer is a device that measures the spatial coherence function $V_\nu(\boldsymbol{r}_1, \boldsymbol{r}_2)$ of the electric field produced by an object in the sky emitting electromagnetic radiation at frequency ν. For spatially incoherent sources located at a very large distance from the observer this function is defined as (Perley, Schwab and Bridle 1989, Chapter 1):

$$V_\nu(\boldsymbol{r}_1, \boldsymbol{r}_2) \approx \int I_\nu(\boldsymbol{s})\, e^{-\frac{2\pi i \nu}{c}\boldsymbol{s}\cdot(\boldsymbol{r}_1 - \boldsymbol{r}_2)}\, d\Omega, \tag{2.1}$$

where $\boldsymbol{s}$ is the direction vector of the sky surface element $d\Omega$ and the observed intensity distribution is

$$I_\nu(\boldsymbol{s}) = |R|^2 \langle |E_\nu(\boldsymbol{s})|^2 \rangle \tag{2.2}$$

R is the distance of the source from the observer and $\boldsymbol{r}_1$, $\boldsymbol{r}_2$ are the displacement vectors of the points where $E_\nu(\boldsymbol{s})$ is to be sampled, corresponding to the positions of the two radio dishes making the observation. Large arrays such as the VLA can be thought of as a collection of many such interferometers working simultaneously. For an array of N antennas, there are $\frac{1}{2}N(N-1)$ possible pairs, all of which collect information about the spatial coherence function V_ν.

2.3. Coordinate Systems

Among radio astronomers there is a convention to adopt a right-handed coordinate system consisting of two planes: the observer or *uv* plane, and the map or *lm* plane.

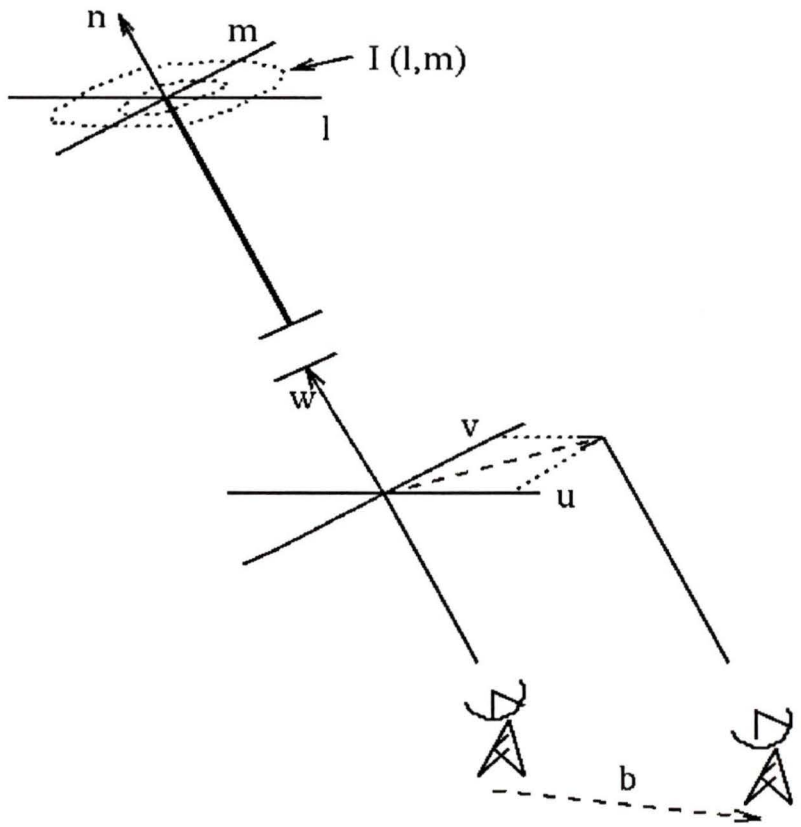

Figure 2.2: (*u,v,w*) and (*l,m,n*) Coordinate Systems for Radio Interferometry

The *uv* plane has unit vectors *u* and *v* pointing to geographical north and east respectively, with the third (*w*) axis pointing at a reference point on the object being observed. Distances in the *uv* plane are measured in units of the observing wavelength and represent the relative displacement of one antenna to another with respect to the source. For example, when observing a source at the zenith, a pair of antennae aligned in the north-south direction with a separation of 1 km would have *uv* coordinates $(\pm 100000/\lambda, 0)$, where λ is the observing wavelength in cm. Since there is no east-west (*v*) component to the base-

line, the *v* coordinate is zero. To obtain even coverage of the *uv* plane therefore, it is necessary to have baselines oriented in many different directions, hence the Y shape of the VLA. This is also the reason why the symmetry axis of the VLA is oriented at 5 degrees from geographical north (Figure 2.1).

The *lm* plane is tangent to the celestial sphere at $(l, m) = 0$, and is the plane onto which the intensity distribution of the sky $I(l,m)$ is mapped. Since the image on the *lm* plane is a projection of the celestial sphere, it is convenient to measure *l* and *m* in a scale proportional to the sine of the angle θ from the origin. Figure 2.3 shows a one-dimensional representation of the celestial sphere seen from the side. The angular distance of point **P** from point **C** on the sky is proportional to sin θ, hence the distance **CP'** on the map will have the same dependence.

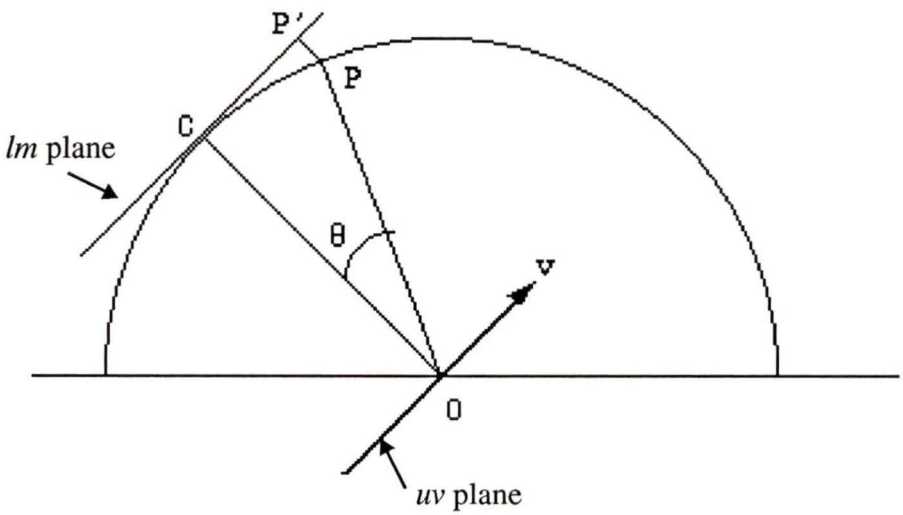

Figure 2.3: Celestial Sphere Diagram

(Adapted from Thompson, Moran and Swenson 1986)

2.4. Fourier Theory

An interferometer measures the spatial coherence field in terms of visibilities $V(u,v)$ which are complex quantities having units of flux density (W Hz^{-1} m^{-2}). Using the coordinate system just described, (2.1) becomes

$$V(u, v, w) = \int_{-\infty}^{\infty}\int_{-\infty}^{\infty} A(l, m)\, I(l, m)\, e^{-2\pi i\left[ul + vm + w\left(\sqrt{1 - l^2 - m^2} - 1\right)\right]} \frac{dl\, dm}{\sqrt{1 - l^2 - m^2}}, \quad (2.3)$$

where $I(l, m)$ is the intensity distribution on the sky at frequency ν, and $A(l, m)$ is the normalized antenna response in the direction (l,m). The antenna response function takes into account the fact that although radio antennas pick up radiation from all directions, they are designed to have increased sensitivity in the small region of sky to which they track throughout an observation. $A(l, m)$ is defined to be equal to one at the center of this region (the primary beam of the antenna), and falls off rapidly with distance from this center, thereby defining the area of sky which is being observed.

Equation (2.3) can be put in the form of a Fourier transform if one makes the assumption that $|l|$ and $|m|$ are small so that $\left(\sqrt{1 - l^2 - m^2} - 1\right) w \approx 0$. We then have

$$I(u, v) = \int_{-\infty}^{\infty}\int_{-\infty}^{\infty} A(l, m)\, I(l, m)\, e^{-2\pi i\,[ul + vm]}\, dl\, dm, \quad (2.4)$$

which can be inverted to give

$$A(l, m)\, I(l, m) = \int_{-\infty}^{\infty}\int_{-\infty}^{\infty} V(u, v)\, e^{2\pi i\,[ul + vm]}\, du\, dv \quad (2.5)$$

Thus to obtain the intensity distribution *I(l,m)* on the sky one performs a two-dimensional Fourier transform of the visibility function and divides by the antenna response *A(l,m)*.

2.5. Sampling

Recovering the true sky intensity distribution *I(l,m)* is complicated by the fact that in practice, $V(u, v)$ is sampled only at discrete locations on the *uv* plane.

One must therefore replace $V(u, v)$ with $V^s(u, v)$, the sampled visibility function. If M measurements are obtained at locations (u_k, v_k), then a sampling distribution can be defined using a two-dimensional Dirac delta function:

$$S(u, v) = \sum_{k=1}^{M} \delta(u - u_k, v - v_k) \tag{2.6}$$

$$V^s(u, v) = V(u, v)\, S(u, v) \tag{2.7}$$

Replacing the true visibility function with the sampled one in (2.5) gives

$$I^D(l, m) = \int_{-\infty}^{\infty} \int_{-\infty}^{\infty} V(u, v)\, S(u, v)\, e^{2\pi i [ul + vm]}\, du\, dv \tag{2.8}$$

$I^D(l, m)$ has been corrected for the antenna response *A (l,m)* and is usually referred to as the dirty image. It is the Fourier transform of $V \cdot S$:

$$I^D = \mathrm{F}[V \cdot S] \tag{2.9}$$

$$I^D = \mathrm{F}[V] * \mathrm{F}[S] \qquad \text{(by convolution theorem)} \tag{2.10}$$

Recalling that $I = \mathrm{F}[V]$ from equation (2.5) and letting $B = \mathrm{F}[S]$,

$$I^D = I * B \tag{2.11}$$

B is the Fourier transform of the sampling distribution and is called the *beam* or point spread function.

If the sky intensity distribution is a point source at (l_o, m_o), then

$$I(l, m) = \delta(l - l_o, m - m_o) \tag{2.12}$$

From (2.11),

$$I^D = \delta * B \tag{2.13}$$

Thus,

$$I^D = B \tag{2.14}$$

The beam is therefore the response of an interferometer to a point source.

The shape of the beam and the sampling distribution are directly related to the geometrical layout of an interferometer. The sampling distribution $S(u, v)$ of the VLA for a short (10 minute) exposure of an object at declination $+24^{\circ}$ is shown in Figure 2.4. At first it may seem odd that a Y-shaped array produces a star-like sampling distribution, but one must remember that each point on the *uv* plane represents the displacement vector of one antenna from another. For a particular antenna pair therefore, there are two displacement

vectors, one from A to B, and vice-versa.

This is readily seen in Figure 2.5, which shows the *uv* coverage for the baselines containing one particular VLA antenna. The points on this diagram correspond to all the possible baselines that can be made with the other antennas in the array.

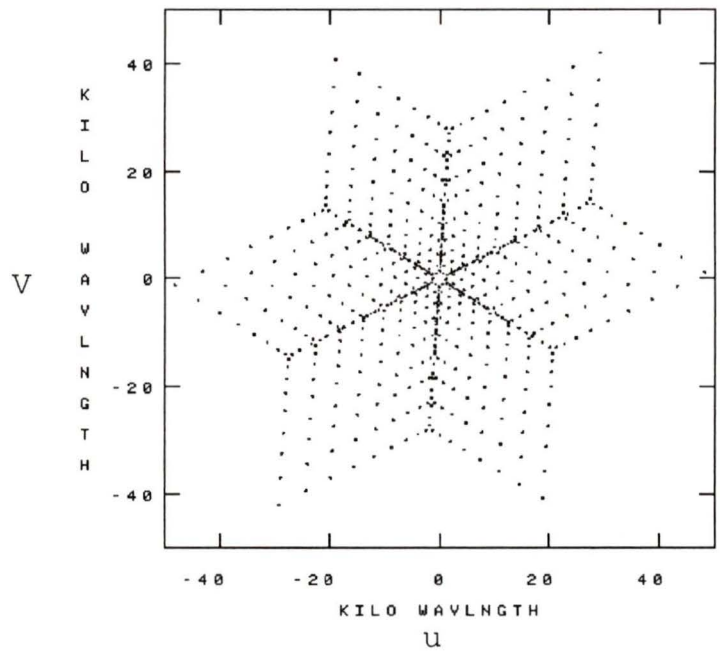

Figure 2.4: VLA Sampling Distribution for an Object at $\delta = +24°$

Figures 2.4 and 2.5 show the sampling distribution for short exposures, or 'snapshots', where the source has not moved appreciably on the sky. During a long observation, the earth will turn, causing a source to become rotated with respect to the *u* and *v* axes, which are fixed in the east and north directions on Earth. The increased integration time lowers the minimum detectable flux density, allowing higher dynamic range to be achieved, while at the same time the empty spaces in the *uv* plane slowly become filled (Figure 2.6). For most sources, the sky intensity distribution *I(l,m)* does not vary appreciably over short time periods, so data from different configurations can be combined to produce excellent *uv* coverage with spectacular results. The high resolution images of Cassiopeia A and Cygnus A found in many astronomy texts are good examples of this technique.

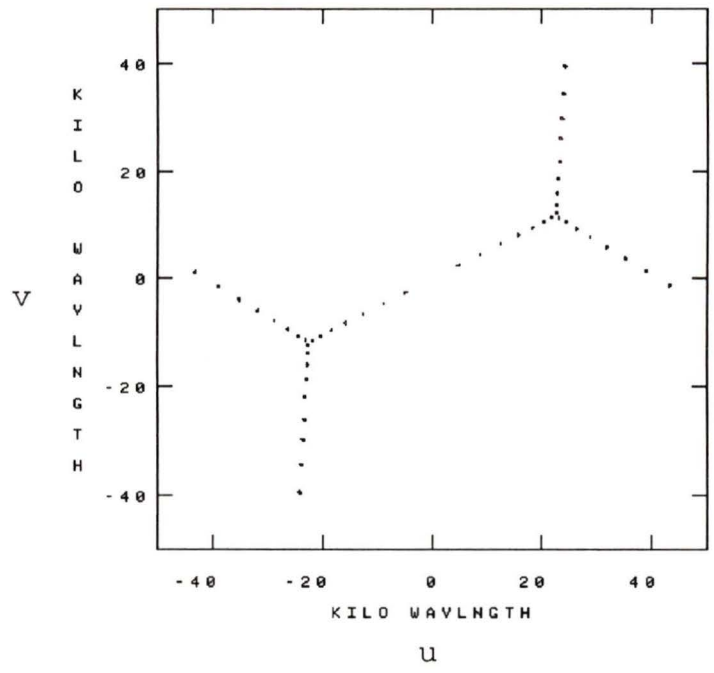

Figure 2.5: Sampling Distribution for Baselines Containing One Specific Antenna ($\delta = +24°$)

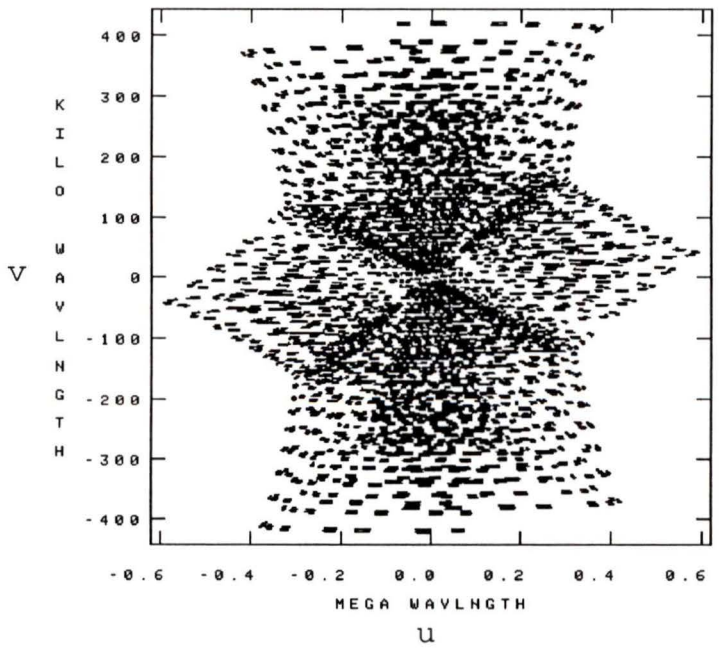

Figure 2.6: Sampling Distribution for a 5 Hour Exposure of an Object at $\delta = +0.2°$

2.6. Imaging

Although the VLA was designed to provide maximal coverage of the *uv* plane, gaps in the *uv* coverage will still exist in the majority of observations made with this instrument. These are due to missing interferometer baselines, both on small scales, and on large scales greater than the maximum spacing of the array. The resulting beam will have a central Gaussian-like peak surrounded by sidelobes which spread the flux from bright objects over large regions of the dirty image.

A natural solution to the effects of non-uniform sampling is to assign weights to the individual points in the uv plane. This is usually accomplished by the use of a weighted sampling function:

$$W(u, v) = \sum_{k=1}^{M} T_k D_k \delta(u - u_k, v - v_k), \tag{2.15}$$

which takes the place of $S(u, v)$ in (2.7). D_k and T_k are discussed below.

Since the VLA contains many more short spacings than large ones, the center of the uv plane is more heavily sampled than the outer regions. Instead of having a thin, steep beam profile, one gets a broad, flat beam that can smear out details in the dirty map. The D_k factors are used to compensate for this. When making images with the Astronomical Image Processing System (AIPS), which was designed for use with VLA data, the user can specify either natural weighting, where $D_k = 1$, or uniform weighting, where $D_k = 1/N(k)$. The $N(k)$ represent the number of observed visibilities in a small region surrounding the k^{th} visibility measurement.

Uniform weighting is especially useful when making images of short duration or 'snapshot' data having sampling distributions similar to the one shown in Figure 2.4. The effects of clustering along the arms of the VLA 'Y' shape are lessened, resulting in higher-quality dirty maps.

The T_k factors are usually referred to as a 'taper', and are used mainly to control the beam shape and to down-weight the points at the edge of the *uv* plane where most of the gaps occur in the *uv* coverage. In AIPS, the T_k's are often calculated using a Gaussian profile having a user-specified width. The Gaussian is circularly symmetric and is centered at $(u,v = 0)$.

By introducing a taper, one reduces small-scale sidelobes in the beam, while at the same time increasing the beam area and therefore the sensitivity to extended emission. The effects of tapering are readily seen in Figures 2.7 and 2.8. The first figure shows an A configuration, snapshot image at a wavelength of 6 cm with no taper. The second figure shows the same image with a Gaussian taper having a width of 150 000 λ at 30% of peak. The larger beamwidth and increased sensitivity to the diffuse structure in the radio lobes are readily apparent in the tapered map.

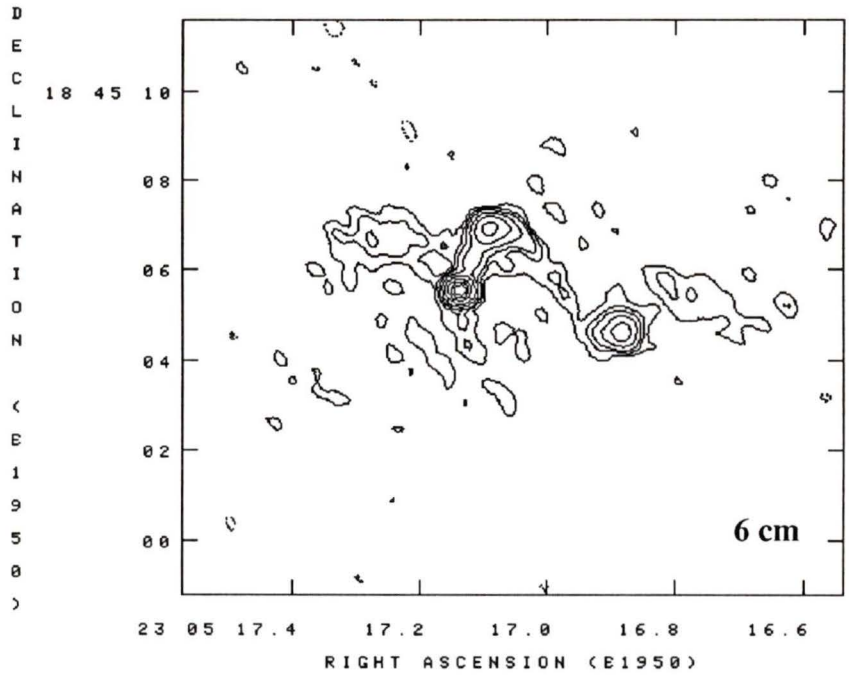

Figure 2.7: Untapered Image of 2305+187

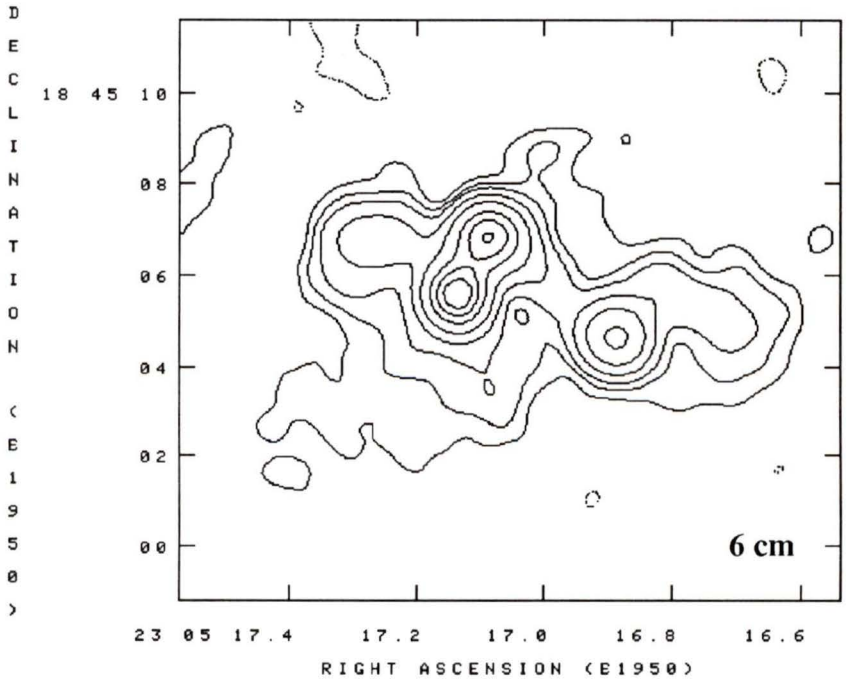

Figure 2.8: Tapered Image of 2305+187

2.7. Image Processing

2.7.1. The CLEAN Algorithm

Although tapering and weighting can greatly improve the beam shape, invariably some sidelobes will remain which degrade the quality of the dirty image. Since these sidelobes are due to missing information about the source structure, the only exact method of eliminating them is by making further observations of the source.

A clever way around this problem was first suggested by Högbom (1974), and involves first modelling the inner region of the synthesized beam with an elliptical Gaussian. This 'clean' beam provides a good approximation to the main synthesized beam, but without any sidelobes.

Högbom's method searches the dirty image for the brightest points in an iterative process and subtracts the dirty beam at these positions, leaving behind a residual map. The set of subtracted 'CLEAN' components is then convolved with the clean beam, producing a new image. Finally, the residual map is added back, producing a 'cleaned' image that does not suffer from the widespread sidelobes of the dirty beam. Högbom's original algorithm has since been improved upon by the use of fast Fourier transforms (see Chapter 8 of Perley, Schwab and Bridle (1989) for further details), and is implemented in the AIPS task MX, which maps and cleans visibility data.

2.7.2. Self Calibration

The raw data from an interferometer are naturally corrupted by instrumental and atmospheric effects, and must therefore be calibrated to recover the true visibility information of a source. This is usually done by observing strong calibrator sources such as 3C 286, 3C 48, or 3C 147, whose flux and structure are known. These observations can be used to provide general corrections for the data, but effects of short-term variations in the Earth's atmosphere still need to be corrected. The observed visibilities $\tilde{V}_{i,j}(t)$ for a single integration interval at time t can be represented by

$$\tilde{V}_{i,j}(t) = g_i(t)\, g_j^*(t)\, V_{i,j}(t), \tag{2.16}$$

where the g_i are complex quantities representing the gains of the individual antennas. These gains contain both instrumental and atmospheric errors not corrected for in the original calibration. Recalling the number of baselines in an array of N elements, there are $1/2\ N(N-1)$ measurements of $g_i(t)\, g_j^*(t)$ per integration interval, while only N $g_i(t)$ terms. For an array with many antennas such as the VLA, one usually has sufficient redundancy and a good enough estimate of the true visibility distribution (from the dirty image) that one can solve for the individual gain factors $g_i(t)$. This *self-calibration* technique is implemented in the AIPS task ASCAL.

The most common method of using ASCAL is firstly to make a map of the source using CLEAN. The brightest CLEAN components are selected by the user and are convolved with the beam to produce a source model $\hat{I}$. By Fourier transforming $\hat{I}$, one gets a set of model visibilities $\hat{V}_{ij}(t_k)$, where t_k represents the k^{th} integration interval. ASCAL then adjusts the gain factors $g_i(t_k)$ so that the observed visibilities approach those of the model, i.e.:

$$\tilde{V}_{ij}(t_k) \approx g_i(t)\, g_j^*(t)\, \hat{V}_{ij}(t_k) \tag{2.17}$$

The self-calibrated visibility data can then be mapped, cleaned, and self-calibrated again in an iterative fashion. By including more clean components in the source model with each iteration, the model improves rapidly, and convergence is usually achieved after only a few iterations.

Chapter Three:

Observations and Data Processing

3.1. Observations

In this thesis new radio data are presented on forty low-redshift quasars previously observed by Ann Gower and John Hutchings as part of a project to investigate the properties of radio quasars over a wide range of redshifts (Hutchings, Price and Gower 1988, Neff, Hutchings and Gower 1989, Neff and Hutchings 1990). The original selection criteria, described in Gower and Hutchings (1984), were chosen to obtain a representative set of quasars from the Hewitt and Burbidge (1989) catalogue having redshifts less than 0.3 and declinations greater than -20° (to be accessible to the VLA). However, time constraints during the observing run forced the omission of several sources. Several other sources with redshifts greater than 0.3 were included as Hutchings had previously obtained optical images of their host galaxies (Hutchings *et al.*1982). The sample is therefore not completely free of bias, but nevertheless forms a reasonable representation of the low-redshift radio quasar population.

The original observations, made at 6 and 20 cm with the VLA in April 1982, revealed a variety of source types including triple, one-sided, and core-dominated sources (Gower and Hutchings 1984). Several sources also contained curved structure near the core that was just barely visible at the resolution of the 6 cm data. This made accurate determinations of the core fluxes and spectral indices difficult for these sources, and it was felt that higher-resolution data were needed to resolve the small-scale structure. Since the original observations were made in the A array configuration, these could only be obtained by going to shorter wavelengths.

The sample was therefore re-observed at 4.89 and 14.97 GHz (6 and 2 cm) with the VLA by Ann Gower in November, 1984. Additional observations at 22.48 GHz (1.3 cm) were made for selected bright objects with possible small-scale structure near the core.

The observations were made in the A configuration in continuum mode with a bandwidth of 50 MHz. In order to maximize the coverage of the *uv* plane, two scans of approximately ten minutes, separated by two hours in hour angle, were made for each object. Due to a snowstorm near the end of the run, a substantial fraction of the sources were re-observed at a later date. These make-up observations were done in exactly the same manner, using the same array configuration and wavelength bands, and are of identical quality as the rest of the data. For both runs the standard sources 3C 286 and 1803+784 were used as flux calibrators, with the former source not being used for the 1.3 cm data due to its small-scale structure being resolved with the A configuration. A summary of the observations is given in Table 3.1.

Table 3.1: Summary of Observations

Object	Name	Wave-length (cm)	Observing Date	Beam[a] (arcsec)	BPA[b] (deg.)	Peak (mJy)	D.R.[c]
0007+106	III Zw 2	6	24 Nov 1984	0.43 x 0.41	-65	554	1045
		2		0.14 x 0.14	-43	1421	1615
		1.3		0.09 x 0.08	9	2108	207
0017+257	4C 25.01	6	24 Nov 1984	0.38 x 0.37	-65	254	651
		2		0.11 x 0.11	16	354	885
0041+119	4C 11.06	6	24 Nov 1984	0.69 x 0.61	-84	43	384
		2		0.29 x 0.27	33	18	28
0100+108	MC 2	2	24 Nov 1984	0.98 x 0.90	-20	5	9
0137+012	4C 01.04	6	24 Nov 1984	0.72 x 0.67	-86	170	283
		2		0.13 x 0.12	10	162	279
0241+622	4U 0241+61	6	24 Nov 1984	0.38 x 0.35	35	241	689
		2		0.13 x 0.11	27	183	223
		1.3		0.27 x 0.25	22	631	48
0736+017	OI+161	6	08 Mar 1985	0.43 x 0.35	-12	1881	4089
		2		0.16 x 0.15	7	2768	2714
0742+318	4C 31.30	6	08 Mar 1985	0.36 x 0.34	29	655	1770
		2		0.14 x 0.13	48	604	1473
0829+047	OJ+349	6	08 Mar 1985	0.44 x 0.35	-9	1062	430
		2		0.14 x 0.13	29	1586	2440
0846+100	4C 09.31	6	08 Mar 1985	0.84 x 0.75	8	6	11
		2		0.51 x 0.47	22	6	15
0952+097	4C 09.35	6	08 Mar 1985	0.39 x 0.35	-12	14	65
		2		0.58 x 0.57	40	7	7
1004+130	4C 13.41	6	08 Mar 1985	0.39 x 0.35	-16	30	115
		2		0.14 x 0.14	46	30	47

Table 3.1: Summary of Observations

Object	Name	Wave-length (cm)	Observing Date	Beam[a] (arcsec)	BPA[b] (deg.)	Peak (mJy)	D.R.[c]
1020-103	OL-133	6	19 Jan 1985	0.50 x 0.35	10	336	1200
		2		0.15 x 0.12	-3	132	388
		1.3	24 Nov 1984	0.20 x 0.19	53	96	5
1028+313	OL+347	6	19 Jan 1985	0.35 x 0.34	-28	79	395
		2		0.12 x 0.12	-48	101	388
1203+011	PKS	6	19 Jan 1985	0.42 x 0.36	-5	147	565
		2		0.13 x 0.13	-47	110	306
1217+023	ON+029	6	19 Jan 1985	1.05 x 0.95	-74	328	745
		2		0.13 x 0.12	-26	293	586
1223+252	4C 25.40	6	19 Jan 1985	0.97 x 0.93	67	10	19
		2		0.38 x 0.36	-69	5	10
1243-072	ON-073	6	19 Jan 1985	0.49 x 0.36	5	867	2477
		2		0.16 x 0.13	0	976	1807
1302-102	OP-106	6	19 Jan 1985	1.51 x 1.44	-13	982	1853
		2		0.17 x 0.12	-2	926	1425
1525+227	OR+241	6	19 Jan 1985	0.35 x 0.34	16	34	150
		2		0.12 x 0.11	27	57	137
1635+119	MC 2	6	24 Nov 1984	1.20 x 0.62	61	37	89
		2		0.54 x 0.52	51	7	5
1721+343	4C 16.39	6	24 Nov 1984	0.65 x 0.63	-5	385	119
		2		0.65 x 0.57	-8	213	173
1725+044	PKS	6	24 Nov 1984	0.85 x 0.80	48	630	1703
		2		0.14 x 0.13	18	595	1026
1739+184	4C 18.51	6	24 Nov 1984	0.55 x 0.41	58	33	82
		2		0.75 x 0.69	0	11	9

Table 3.1: Summary of Observations

Object	Name	Wave-length (cm)	Observing Date	Beam[a] (arcsec)	BPA[b] (deg.)	Peak (mJy)	D.R.[c]
2135-147	OX-158	6	24 Nov 1984	0.60 x 0.54	-20	135	96
		2		1.29 x 1.08	-15	151	122
2141+175	OX+169	6	24 Nov 1984	0.45 x 0.38	85	907	1093
		2		0.73 x 0.72	38	902	567
2201+315	4C 31.63	6	24 Nov 1984	0.85 x 0.73	75	3623	929
		2		0.49 x 0.49	45	4244	1505
2217+087N,S	4C 08.66	6	24 Nov 1984	5.36 x 5.22	68	26	20
2217+087N		2		0.13 x 0.12	11	29	46
2217+087S		2		0.35 x 0.33	36	9	11
2247+140	4C 14.82	6	24 Nov 1984	0.41 x 0.39	17	1123	1059
		2		0.12 x 0.11	1	326	447
		1.3		0.08 x 0.08	8	484	103
2305+187	4C 18.68	6	24 Nov 1984	0.60 x 0.54	65	68	146
		2		0.72 x 0.67	24	41	39
2328+167	MC 3	6	24 Nov 1984	0.38 x 0.38	40	30	121
		2		0.12 x 0.11	17	6	13
2331-240	OZ+252	6	24 Nov 1984	0.72 x 0.37	-7	1192	1268
		2		0.22 x 0.12	-10	1294	775
2355-082	PKS	6	24 Nov 1984	0.48 x 0.41	-23	68	317
		2		0.36 x 0.35	38	42	62

Notes on Table 3.1:

(a) - Beam dimensions are the full width half maximum values for the major and minor axes.

(b) - BPA = position angle of the beams' major axis, measured in degrees east of north.

(c) - D.R. = Dynamic Range (see §3.2)

3.2. Data Processing

The data were processed using the Astronomical Image Processing System (AIPS) developed by the NRAO for use with the VLA. Using the tasks MX and ASCAL discussed in Chapter 2, the data were mapped, cleaned, and self-calibrated for several iterations until the self-calibration model converged for each source. The typical characteristics of the maps were as follows:

Table 3.2: Map Parameters

Wavelength (cm)	Frequency (GHz)	Cellsize ("/ pixel)	Beam Size (")	Theoretical Noise (mJy)
6	4.8851	0.10	0.38	~0.2
2	14.9649	0.03	0.14	~0.5
1.3	22.4851	0.003	0.08	~0.9

In many of the maps a Gaussian taper was used to increase the sensitivity to faint diffuse structure. These can be recognized in Table 3.1 as having a larger than average beam size. This table also gives the dynamic range of each map, which was calculated by taking the ratio of the peak brightness in the map to the root- mean-square pixel noise calculated in a region devoid of radio emission.

The final maps can be found in Appendix A. Due to the small size of the primary beam at 6 and 2 cm (see Chapter 2), only the core regions of many of the quasars could be mapped adequately. In order to give the reader a more complete picture of the structure of each quasar, I have included maps of the extended structure of some sources that have been previously published in the literature. The relevant references are given alongside each map.

3.3. Radio Core Data

3.3.1. Core Fluxes

Table 3.3 lists the data pertaining to the core components of the quasars in the sample. The 1.3, 2 and 6 cm core fluxes were derived using the AIPS task JMFIT, which fits a two-dimensional Gaussian to the core on the radio map. Included in the table are the core fluxes at 6 and 20 cm from Gower and Hutchings (1984), obtained in April 1982 with the VLA using the same observational setup.

3.3.2. Core Flux Errors

Determining formal error estimates for fluxes obtained from interferometer data is very difficult since there are many sources of error, whose relative contributions depend on both the observational setup and the source being observed. For faint sources, it is the system (thermal) noise that dominates, but for brighter ones, the error in the flux depends largely on the accuracy of the flux calibration. The error can also depend on the parameters used when mapping the data, as the sensitivity in a map is determined by the beam size, taper and choice of weighting function. (see Perley, Schwab and Bridle 1989, Chapter 6).

Another important consideration in determining the core flux is the presence of nearby extended structure. For several of the sources in my sample the 2 cm data have revealed small extensions that were un-resolved at 6 cm, implying that the latter fluxes were contaminated by extended structure. I have marked these sources with an asterisk in Table 3.3.

Since core flux error estimates are needed to determine the degree of variability in Chapter 4, I have assigned separate errors to the weak (< 10 mJy) and strong core fluxes. Following Rys and Machalski (1990), I have taken the errors in the strong sources to be 5%, except those marked with asterisks, as described above, whose errors were estimated to be 20%. For the weak sources, I have also assumed an error of 20%, which is the upper limit of the standard errors obtained from the Gaussian core fits.

3.3.3. Core Spectral Index

Since the radio spectra of many quasars approximately follow a power law, it is useful to define a spectral index, which is simply the slope of the spectrum in a log S versus log ν plot. There is an unfortunate state of confusion in the literature at present over how the spectral index is defined, with some authors choosing $S \propto \nu^{\alpha}$, and others $S \propto \nu^{-\alpha}$. I have decided to choose the former, so that the spectral index α is defined as

$$\alpha = \frac{(\log S_{6\mathrm{cm}} - \log S_{2\mathrm{cm}})}{(\log 2 - \log 6)} \tag{3.1}$$

Since the spectral indices derived in this manner depend on accurate core fluxes, the values for sources with extended structure near the core (marked with an asterisk in Table 3.3) will necessarily contain larger errors.

3.3.4. Core Fraction

The core fraction, defined as the ratio of core to total (core + extended) flux, is an important parameter in testing unified schemes, which predict it to be a function of source orientation. The A configuration of the VLA is not sensitive to extended structure due to the lack of short antenna baselines, so it was necessary to draw on other data to obtain values for the total flux. Several of the sources were observed and imaged in May 1984 at 20 cm by Ann Gower with the VLA in the C configuration. Being a more compact array, this configuration provided a larger field of view and increased sensitivity to extended structure. This enabled an accurate measurement of the total flux, and was used to determine the core fraction at 20 cm. These sources are marked with a dagger symbol in Table 3.3.

For the other sources, an extensive literature search was made with the help of the NASA Extragalactic Database[1] for single-dish fluxes in the radio and millimeter wave-

1. The NASA/IPAC Extragalactic Database (NED) is operated by the Jet Propulsion Laboratory, California Institute of Techonology, under contract with the National Aeronautics and Space Administration.

length ranges. Total-flux estimates were made by fitting a parabola to the locus of points on a log-log plot of flux versus wavelength. The total-flux estimates were uncertain in many cases due to variability of the source and/or errors in the single-dish fluxes. The core fractions for these objects are marked with a colon (:) in Table 3.3.

Since the core and extended structure generally have different spectral indices, one must correct for bandpass effects caused by the redshift. This can be accomplished by converting the observed flux S_{obs} to that in the rest frame of the quasar (S_i).

Assuming a power law spectrum for the core with spectral index α_c and a redshift z, we have

$$S_{c,i} = S_{c,obs}(1+z)^{-\alpha_c - 1} \qquad \text{W cm}^{-2}\ \text{Hz}^{-1} \tag{3.2}$$

Likewise for the lobes,

$$S_{l,i} = S_{l,obs}(1+z)^{-\alpha_l - 1} \qquad \text{W cm}^{-2}\ \text{Hz}^{-1} \tag{3.3}$$

Therefore, the core fraction in the rest frame of the quasar is given by

$$f_i = \frac{S_{c,i}}{S_{c,i} + S_{l,i}} \tag{3.4}$$

$$f_i = \frac{1}{\left(1 + \frac{S_{l,obs}}{S_{c,obs}}(1+z)^{\alpha_c - \alpha_l}\right)} \tag{3.5}$$

In terms of the observed core fraction this becomes

$$f_i = \frac{1}{1 + (\frac{1}{f_{obs}} - 1)\ (1+z)^{\alpha_c - \alpha_l}} \tag{3.6}$$

Since accurate values for the lobe spectral indices were not available, a typical value of $\alpha_l = -0.8$ (Kellermann and Owen, 1988) was used.

3.3.5. Core Luminosity

The core luminosities were calculated using values of $H_o = 100$ km s^{-1} Mpc^{-1} and $q_o = 0.5$, which will be used throughout this thesis. The luminosity in the rest frame of the quasar, corrected for bandpass is

$$L = 4\pi d_l^2\ (1+z)^{-\alpha_c - 1} f_{obs} \qquad W\ Hz^{-1}, \tag{3.7}$$

where α_c is the 6 - 2 cm core spectral index, f_{obs} is the observed flux, and the luminosity distance d_l is given by

$$d_l = \frac{2c}{H_o}[\ (1+z) - (1+z)^{1/2}] \tag{3.8}$$

Table 3.3: Radio Core Data

Object	Core Flux (milliJanskys)					Spectral Index (6-2 cm)	Core Fraction[c]			Core Luminosity log[W Hz^{-1}]		
	1.3 cm	2 cm	6 cm	6 cm (1982)[d]	20 cm (1982)[d]		2 cm	6 cm	20 cm (1982)	2 cm	6 cm	20 cm (1982)
0007+106	2128	1432	590	470	340	0.81	1.00	1.00	1.00	25.02	24.64	24.40
0017+257	-	357	299	310	240	0.16	0.56	0.48	0.28[†]	25.42	25.34	25.25
0041+119	-	18	20	17	11	-0.08	0.16	0.07	0.02	23.97	24.01	23.75
0100+108A	-	5	-	11	48	-	-[b]	-	-	23.09	23.43	24.07
0100+108B		3	-	>8	48	-	-	-	-	22.87	23.29	24.07
0137+012	-	163	178	150	230	-0.08	0.38	0.22	0.15[†]	25.03	25.07	25.18
0241+622	615	191	256	300	160	-0.27	0.39	0.66	0.56	23.59	23.72	23.52
0736+017	-	2769	1882	2240	2190	0.35	1.00:	1.00:	0.89:	25.97	25.80	25.87
0742+318	-	604	656	640	610	-0.07	0.65	0.79	0.52	26.07	26.10	26.07
0829+047	-	1588	1065	656	740	0.36	1.00	0.94	0.92	25.68	25.51	25.35
0846+100	-	7.4	5.6	6	7	0.25	0.11	0.03	0.01[†]	23.92	23.80	23.90
0851+202	-	-	-	3200	2270	-	-	1.00	1.00	-	26.43[a]	26.28
0952+097	-	5.5	7.8	7	9	-0.32	0.07	0.04	0.02	23.70	23.85	23.91
1004+130	-	29	30	12	20	-0.04	0.15	0.06	0.01[†]	24.21	24.23	24.05
1011-282	-	-	-	37	27	-	-	0.11	0.01[†]	-	24.32[a]	24.18
1020-103	95	133	367*	330*	-	-0.92	0.54	0.85	-	24.78	25.22	-

Table 3.3: Radio Core Data

Object	Core Flux (milliJanskys)					Spectral Index (6-2 cm)	Core Fraction[c]			Core Luminosity log[W Hz^{-1}]		
	1.3 cm	2 cm	6 cm	6 cm (1982)[d]	20 cm (1982)[d]		2 cm	6 cm	20 cm (1982)	2 cm	6 cm	20 cm (1982)
1028+313	-	107	83	110	89	0.24	0.68	0.47	0.29[†]	24.50	24.39	24.42
1203+011	-	114	154	170	130	-0.27	1.00	1.00	1.00[†]	24.11	24.24	24.17
1217+023	-	319	330	320	220	-0.03	0.99	0.66	0.31[†]	25.25	25.27	25.09
1223+252	-	6.6	3.5	4.0	2.4	0.58	0.05	0.02	0.00[†]	23.60	23.32	23.16
1243-072	-	977	869	1300	850	0.11	0.56	0.96	0.99	25.82	25.77	25.76
1302-102	-	927	982	1185	570	-0.05	0.97	0.95	0.81[†]	25.86	25.89	25.65
1400+162	-	-	-	130	190	-	-	0.27	0.21[†]	-	24.90[a]	25.07
1525+227	-	59	39	43	43	0.38	0.73	0.21	0.11[†]	24.52	24.34	24.38
1545+210	-	-	-	-	35	-	-	-	0.02[†]	-	-	-
1635+119	-	8.0	36	17	16	-1.37	0.42	0.75	0.13	23.31	23.97	23.62
1721+343	-	210	386	370	450	-0.56	0.40	0.50	0.32	24.98	25.25	25.31
1725+044	-	597	634	730	560	-0.06	0.70	0.85	0.83	25.70	25.72	25.67
1739+184	-	13	32	25	23	-0.83	0.14	0.10	0.02[†]	23.71	24.10	23.96
2135-147	-	157	136	126	87	0.13	0.27	0.09	0.07[†]	24.78	24.72	24.52
2141+175	-	904	918	280	370	-0.01	1.00	1.00	1.00	25.60	25.61	25.22
2201+315	-	4247	3696	1500	1100	0.13	0.90:	1.00:	0.59:[†]	26.53	26.47	25.95

Table 3.3: Radio Core Data

Object	Core Flux (milliJanskys)					Spectral Index (6-2 cm)	Core Fraction[c]			Core Luminosity log[W Hz^{-1}]		
	1.3 cm	2 cm	6 cm	6 cm (1982)[d]	20 cm (1982)[d]		2 cm	6 cm	20 cm (1982)	2 cm	6 cm	20 cm (1982)
2217+08N	-	28	27	27	22	0.03	0.57	0.14	0.03	24.95	24.93	24.85
2217+08S	-	9.1	12	7	8	-0.29	0.19	0.15	0.04	23.69	23.83	23.63
2247+140	480	394	1277*	1210*	1870	-1.07	0.69	1.00	0.90	25.43	25.94	26.10
2305+187	-	46	70	81	80	-0.38	0.21	0.15	0.08†	24.67	24.85	24.91
2328+167	-	6.3	41*	25*	-	-1.70	0.22	0.60	-	23.87	24.68	-
2331-240	-	1346	1197	910	-	0.11	1.00	1.00	-	24.51	24.46	-
2355-082	-	41	89*	110*	-	-0.71	0.66	0.45	-	24.31	24.65	-

Notes on Table 3.3:

(a) - denotes luminosity derived from 1982 core fluxes and spectral indices.

(b) - confusion exists at present as to which component is the core in this source (see Appendix A)

(c) - core fractions are the ratio of core to total flux, with latter quantity estimated from single dish fluxes (see §3.3.4).

(d) - 1982 core fluxes are from Gower and Hutchings (1984)

† - core fraction calculated using total flux from unpublished C configuration data of Ann Gower (see §3.3.4).

: - core fraction uncertain due to source variabilty and/or single dish flux errors (see §3.3.4)

* - denotes core with close-in structure (see §3.3.2)

- all quantities are calculated using H_o =100 km s^{-1} Mpc^{-1}, q_o = 0.5

- 1 Jansky = 10^{-26} W m^{-2} Hz^{-1}

- spectral indices are defined as $S \propto \nu^{\alpha}$

3.4. Morphological Data

In addition to the core data, it is necessary to present here a summary of the morphological data for the low-redshift sample. As mentioned previously, many of the sources contain structure larger than the primary beam of the 6 cm data, thus much of the data in Table 3.4 was taken from the literature. The final column cites the references used for each object.

The first column contains a simple description of the source type, with the components (C=core, L=lobe) in order of decreasing luminosity. The redshift data were taken from the Hewitt and Burbidge catalogue of quasi-stellar objects (Hewitt and Burbidge 1989), and refer to the optical core. The LAS (largest apparent size) is a standard parameter used in radio quasar studies, and refers to the angular separation of the extremities in the radio structure. Estimates of the LAS are necessarily limited by the noise level and sensitivity of the maps used, and the values in Table 3.4 should be taken as lower limits only.

For triple sources, consisting of an unresolved core and two extended radio lobes, a bend angle was measured. It is defined as the angle between lines joining the hotspots of each lobe and the core, with straight sources having a bend of zero. In practice these angles can only be measured to within two or three degrees due to poor resolution and/or edge-darkening effects in radio lobes. The values in parentheses are extreme examples of the above, and have a higher uncertainty associated with them.

Table 3.4 also includes the distances from the core to the two hotspots, D_1 and D_2 respectively. Following Teerikorpi (1984), the core-to-hotspot distance ratio Q was calculated. This parameter, discussed in further detail in Chapter 5, is defined to be the ratio of D_1 and D_2 that is always less than unity.

Table 3.4: Morphological Data

Object	Type[a]	z	Lum. Dist. (Mpc)	LAS[b] (")	LAS (kpc)	Bend (°)	Q[c]	Refs.
0007+106	C	0.087	267	< 0.14	< 0.2	-	-	
0017+257	CLL	0.284	905	48	128	47	0.91	1,10
0041+119	LLC	0.228	719	46	105	9	0.57	
0100+108	LL?	0.144	447	3.6	6.0	-	-	2
0137+012	CLL	0.260	825	35	88	1	0.74	2
0241+622	CL	0.044	133	3.3	2.0	-	-	2
0736+017	CLL	0.191	598	27.4	56	2	0.55	3
0742+318	CLL	0.462	1517	120	413	4	0.96	4,6
0829+047	CLL	0.180	562	29.3	57	(92)	(0.55)	3
0846+100	LCL	0.366	1183	69	212	13	0.72	2
0851+202	C	0.310	993	< 0.4	< 1.1	-	-	2
0952+097	LCL	0.298	952	12.5	34	12	0.48	2
0957+227	LL	0.419	1367	35	115	N.C.	-	2
1004+130	CLL	0.240	759	(115)	(275)	9	(0.36)	5,7
1011-282	CLL	0.250	792	72.6	178	23	0.43	2
1020-103	CLL	0.197	618	1.7	3.6	4	0.09	
1028+313	CLL	0.177	553	(28)	(54)	(0)	0.60	2,11
1203+011	C	0.104	320	< 0.14	< 0.2	-	-	
1217+023	CLL	0.240	759	(135)	(322)	(14)	(0.95)	6,2
1223+252	LLC	0.268	852	67	172	4	0.95	2
1243-072	CLL	0.270	858	9.8	25.3	(0)	0.41	2
1254-333	LL	0.190	595	24.8	50	N.C.	-	2
1302-102	CLL	0.286	912	16.0	43	52	(0.83)	
1400+162	CLL	0.244	773	(36)	(87)	(53)	0.83	3
1525+227	CL	0.253	802	6.0	14.9	-	-	
1545+210	LLC	0.264	838	69	176	0	0.74	2
1635+119	CLL	0.146	453	205	343	13	0.72	7
1721+343	CLL	0.206	645	260	560	0	0.97	8,12
1725+044	CL	0.296	945	5.1	13.9	-	-	2
1739+184	LLC	0.186	582	206	413	7	0.96	2

Table 3.4: Morphological Data

Object	Type[a]	z	Lum. Dist. (Mpc)	LAS[b] (")	LAS (kpc)	Bend (°)	Q[c]	Refs.
2135-147	LCL	0.200	627	150	317	4	(0.90)	3
2141+175	C	0.213	670	< 0.14	< 0.3	-	-	
2201+315	CLL	0.297	949	91	250	12	0.83	6
2217+08N	CLL	0.623	2094	34	131	59	0.84	9
2217+08S	CLL	0.228	719	116	268	5	0.92	9
2247+140	CL	0.237	749	0.2	0.5	-	-	
2305+187	CLL	0.313	1003	(20)	(56)	(15)	(0.59)	2
2328+167	CL	0.284	905	1.0	2.7	-	-	
2331-240	C	0.048	146	< 0.14	< 0.1	-	-	
2355-082	CL	0.211	663	3.2	7.0	-	-	

Notes on Table 3.4:

(a) - Components in order of decreasing luminosity, where C = Core, L = Lobe

(b) - Largest apparent size of extended radio structure (see §3.4)

(c) - Q = Ratio of core-hotspot distances as defined by Teerikorpi (1984) (see §3.4)

- all quantities are calculated using H_o =100 km s^{-1} Mpc^{-1}, q_o = 0.5

- Quantities in parentheses are uncertain due to diffuseness of lobes and/or poor resolution.

- N.C. = No radio core detected at 20 cm.

References:

1. Garrington *et al.* (1991)
2. Gower and Hutchings (1984)
3. Antonucci and Ulvestad (1985)
4. Neff (1982b)
5. Miley and Hartsuijker (1978)
6. Neff (1982a)
7. Unpublished C Configuration Data of Ann Gower
8. Barthel (1987)
9. Harris *et al.* (1983)
10. Stocke *et al.* (1985)
11 Hutchings and Neff (1990)
12. Jägers *et al.* (1982)

3.5. Optical Data

As part of a program to obtain high resolution optical images of the host galaxies of low redshift quasars, Hutchings and others (see end of Table 3.5 for references) have published optical data on 33 of the 40 quasars in the sample. Many of these images can be found in Appendix A, and a summary of the optical quantities is given in Table 3.5. All quantities have been converted to a standard Euclidean cosmology with H_0= 100 and q_0= 0.5. Where possible, apparent magnitudes were taken from the papers by Hutchings listed in the references column. Otherwise, magnitudes from the Hewitt and Burbidge catalogue were used. The L_n / L_f ratio is defined by Hutchings *et al.* (1984b) to be the ratio of unresolved (nuclear) to resolved (fuzz) luminosity, corrected for bandpass, redshift, signal level, and seeing effects. The host and nuclear magnitudes (in the R band) contain k-corrections and are corrected for foreground extinction. Further details on optical quantities can be found in the references listed at the end of Table 3.5.

Table 3.5: Optical Data

Object	z	m_v	M_{gal}	M_{nuc}	L_n/L_f	Scale Length (kpc)	$(B-R)_{gal}$	$(B-R)_{nuc}$	Refs.
0007+106	0.087	15.4	-21.6	-20.5	2.80	2.0	1.10	0.10	2,4
0017+257	0.284	15.4	-24.3	-21.6	17.00	-	0.70	0.10	2,3
0041+119	0.228	19.0	-19.7	-19.4	1.60	4.6	-	-	3,4
0100+108	0.144	18.0	-	-	-	-	-	-	
0137+012	0.260	17.1	-21.2	-22.5	0.30	11.8	-	-	4
0241+622	0.044	16.4	-21.1	-23.3	8.40	0.7	-	-	2
0736+017	0.191	16.5	-22.4	-21.2	3.00	4.2	0.40	0.10	4,5,7
0742+318	0.462	16.0	-24.8	-21.1	30.00	-	-	0.30	2,4,7
0829+047	0.180	16.5	-	-	-	-	-	-	
0846+100	0.366	19.2	-21.8	-20.9	2.30	3.2	-	-	2,4
0851+202	0.310	14.0	-26.1	-22.4	30.00	-	-	-	2,4
0952+097	0.298	17.2	-	-	-	-	-	-	
0957+227	0.419	17.9	-	-	0.90	-	-	-	6
1004+130	0.240	15.1	-24.1	-21.8	8.00	5.3	-	-0.10	4,7
1011-282	0.250	15.7	-23.7	-22.1	4.00	9.6	-	0.20	2,4,7
1020-103	0.197	16.5	-23.1	-20.4	12.00	3.7	-0.10	0.20	2,4,7
1028+313	0.177	16.7	-21.9	-20.9	2.50	10.1	-0.50	-	4
1203+011	0.104	18.2	-19.4	-19.5	-	-	-	0.40	2,7

Table 3.5: Optical Data

Object	z	m_v	M_{gal}	M_{nuc}	L_n/L_f	Scale Length (kpc)	$(B-R)_{gal}$	$(B-R)_{nuc}$	Refs.
1217+023	0.240	16.7	-22.1	-21.8	17.00	5.0	1.10	-0.10	7
1223+252	0.268	16.0	-22.8	-23.0	0.80	3.2	0.00	-0.10	1,4,7
1243-072	0.270	18.0	-	-	-	-	-	-	
1254-333	0.190	18.0	-20.5	-19.4	7.20	2.3	-	0.40	7
1302-102	0.286	14.9	-24.5	-23.7	2.50	4.1	-	0.00	2,4,7
1400+162	0.244	16.5	-23.1	-22.4	1.90	3.8	1.20	-0.10	2,4,7
1525+227	0.253	16.4	-22.7	-20.7	6.00	4.5	-	-	2,4
1545+210	0.264	16.6	-22.9	-20.9	-	-	-	0.10	2,7
1635+119	0.146	16.5	-20.3	-21.2	0.40	4.2	-	-	4
1721+343	0.206	16.5	-	-	-	-	-	-	
1725+044	0.296	18.2	-21.1	-21.7	2.00	1.6	-	-	2
1739+184	0.186	16.4	-	-	-	-	-	-	
2135-147	0.200	15.4	-22.1	-23.4	3.70	1.5	0.60	0.10	2
2141+175	0.213	15.5	-22.1	-23.6	4.60	1.6	0.30	-	2
2201+315	0.297	15.5	-23.3	-24.3	3.30	7.3	-	-	2
2217+08N	0.623	18.6	-24.5	-20.5	0.12	2.9	-	-	2
2217+08S	0.228	17.6	-22.3	-22.2	0.22	2.7	-	-	2
2247+140	0.237	17.0	-22.0	-21.4	1.70	2.8	0.20	0.10	2,4,7
2305+187	0.313	16.5	-24.1	-22.2	0.23	4.1	1.40	0.10	2

Table 3.5: Optical Data

Object	z	m_v	M_{gal}	M_{nuc}	L_n/L_f	Scale Length (kpc)	$(B-R)_{gal}$	$(B-R)_{nuc}$	Refs.
2328+167	0.284	18.3	-21.4	-20.4	2.50	4.7	-	-	4
2331-240	0.048	17.0	-18.7	-17.8	0.44	1.8	-	-	2
2355-082	0.211	17.5	-	-	-	-	-	-	

References for Table 3.5:

1. Hutchings and Neff (1992)
2. Hutchings *et al.* (1984b)
3. Hutchings *et al.* (1984a)
4. Hutchings and Neff (1990)
5. Wyckoff *et al.* (1981)
6. Hutchings *et al.* (1982)
7. Hutchings (1987)

Chapter Four:

Core Variability and Spectral Index

4.1. Background

In the thirty years since its discovery (Dent 1965), much progress has been made towards understanding the variability of radio quasars. However, there is still no model which can explain the wide variety of variability timescales and amplitudes that have been observed to date. As will be made clear later in this chapter, part of the problem is a lack of extensive variability data for the extended and core components of the different classes of active galactic nuclei (AGN). Before showing how the low-redshift quasar sample data of this thesis can fill in some of this gap, I will discuss some of the current models for variability, and the results of studies on which they are based.

Historically, the first variability models to be proposed were expanding source models (Pauliny-Toth and Kellerman 1966), where a spherical cloud of plasma expands isotropically at constant non-relativistic velocity. As the sphere expands, the total flux increases, but soon drops as the source becomes optically thin. Since the opacity is dependent on the observed wavelength, this model predicts that bursts in flux should occur first at high frequency and then propagate to lower observing frequencies.

Although the behaviour of many sources does follow this pattern, there are many other sources which either show no time lag at all, or appear to have no correlation at all between bursts at different wavelengths. (Epstein *et al.* 1982)

The expanding source model also predicts that the maximum flux of a burst is proportional to ν^b, where $1 < b < 1.3$. This range of b does not agree with the observed value of $b = 0.4 \pm 0.2$ however (Andrew *et al.* 1978).

It was partly due to these problems that expanding source models have lost support in favour of beaming or 'shock' models (Hughes *et al.* 1985, Marscher and Gear 1985), which involve a bulk relativistic flow of electrons near the line of sight. These models

were first introduced as a solution to the brightness temperature, or 'inverse-Compton catastrophe' problem.

As the relativistic electrons inside the core of a quasar spiral around magnetic field lines, they give off large amounts of synchrotron radiation, which is believed to account for the bulk of the luminosity seen at radio wavelengths. These same electrons can also lose their energy through collisions with photons in an inverse-Compton scattering process. By using a simple source model having a power law distribution of electron energies and spatially-homogeneous magnetic fields, Altschuler (1989) has calculated a theoretical value for the ratio of inverse-Compton (U_{compt}) to synchrotron (U_{sync}) radiation:

$$R_{cs} = \frac{U_{compt}}{U_{sync}} = 5\times10^{-3}\left[\frac{T_b}{10^{12}}\right]^5 \nu_h, \tag{4.1}$$

where ν_h is the high-frequency cutoff (in MHz) associated with the highest energy electrons in the source, and T_b is the brightness temperature in ° K, defined as the temperature of a black body emitting the same luminosity as the source at a given observing frequency. In terms of the angular size of the source θ, and the flux density S_ν, this works out to be (Kellermann and Owen 1988)

$$T_b = \frac{2c^2 S_\nu}{\pi k \nu^2 \theta^2}, \tag{4.2}$$

where k is Boltzmann's constant and c is the speed of light.

Due to the efficiency of the inverse-Compton process, it is believed that a source will undergo rapid energy losses (an inverse-Compton 'catastrophe') if $R_{cs} >> 1$ (Altschuler 1989).

By using the characteristic timescales of variability to estimate the angular diameter of the emitting region (θ), Fanti *et al.* (1983) found typical brightness temperatures of

$T_b \cong 10^{14}$ °K . This would imply a large degree of inverse-Compton scattering, which would produce copious amounts of ultraviolet and x-ray photons. The predicted x-ray fluxes from this model are much higher than the observed fluxes however (Biermann *et al.* 1989), hence the origin of the brightness temperature problem.

Relativistic beaming models can solve this problem by assuming that the flux density on the left hand side of (4.2) has been increased by Doppler boosting, thus requiring lower values for T_b. The most successful model in this class has been the shocked-jet model of Hughes *et al.* (1989). It suggests that the bright, superluminal components seen in VLBI images are shocks in the relativistic flow that are interacting with inhomogeneities in the surrounding medium. These shocks cause random flares in luminosity as the interacting material brightens and then fades. Through the use of computer modelling, Hughes *et al.* have had a large degree of success in reproducing the flare behaviour of many radio sources. The shocked-jet model can also explain the 'shot noise' analysis of Cruise and Dodds (1985), who found that the light curves of variable sources could be well-modelled as the sum of a series of identical pulses, randomly spaced in time.

In addition to solving the brightness temperature problem, relativistic-jet models are attractive as they can explain the observation that all VLBI jets are one sided (with the exception of 3C 338, recently mapped by Feretti *et al.* 1992). This would be due to the fact that the radiation from the opposite jet is beamed away from the observer, and is therefore greatly de-amplified.

A natural consequence of the beaming models is that the most variable sources are those whose viewing angle (Ψ) is very close to the line of sight, since the timescale of intrinsic variability is shortened by a factor of $\gamma(1-\beta\cos\Psi)\ (1+z)$. Saikia *et al.* (1991) have also pointed out that if these components follow wiggly paths near the line of sight, the observed Doppler beaming factors can change dramatically, leading to erratic flux changes.

These arguments have led to the suggestion that BL Lac objects, which display a high degree of rapid optical variability, are sources with jets pointed directly at us. However,

Altschuler (1983) has found that out of a sample of 31 BL Lacs, nearly half displayed no substantial degree of variability at 2380 MHz over a two and a half year monitoring period. Furthermore, questions have been raised about the parent population of BL Lacs. Due to the low probability of a source being pointed directly at us, for every BL Lac there should be a large number of unbeamed sources. Various candidates have been proposed, the most popular being elliptical radio galaxies (Browne 1983, Barthel *et al.* 1986, Padovani 1992), but the narrow range of γ values required to reproduce the ratio of observed space densities (Padovani and Urry 1992) are not consistent with the ranges found from observations of superluminal motion (Cohen 1989).

There do appear to be statistical differences in the degree of variability seen in the various classes of AGN, with BL Lacs being the most variable, followed by quasars and then radio galaxies (Eckart, Hummel and Witzel 1989, Ghosh and Gopal-Krishna 1990). This finding lends support to both the beaming and unified models, the latter of which proposes that the optical classifications of AGN are a consequence of viewing angle. The issue of quasar orientation will be discussed in more detail in Chapter 5.

4.2. Core Variability

Very few studies to date have focussed on the variability of the core components of quasars, as a result of unavoidable observational scheduling and time constraints. To resolve the cores of extended triple sources one needs the sensitivity and large baselines provided by an interferometer, but these instruments are largely oversubscribed, making observing time difficult to obtain. Multi-epoch, high-resolution maps of extended radio sources are therefore quite rare in the literature. What many groups have done instead is to take regular flux-density measurements of a sample of sources over long time intervals with single-dish telescopes. In this way, many well-sampled light curves have been obtained for use in variability studies. Due to the poor sensitivity of single-dish instruments, the sample of well-monitored objects consists almost entirely of bright, core-dominated sources. Since very few members of this class of object have substantial large-scale

structure very little is known at present about the radio light-curves of weak-cored, lobe-dominated quasars.

Although the two-epoch 6 cm data presented in this thesis obviously cannot provide much information regarding the variability characteristics of individual sources, the sample is large enough that statistical comparisons can be made between different groups of objects, such as the core- and lobe-dominated sources. Furthermore, the maps are of sufficiently high resolution that we can be assured that we are measuring variability in the core components only.

4.2.1. Variability Index

In assigning a measure of the variability to each source, I have used the ΔS/S statistic of Edelson (1987) to compare the fluxes at 6 cm from 1982 and 1984. It is defined by Edelson as:

$$\frac{\Delta S}{S} = \frac{|S_{1984} - S_{1982}|}{(S_{1984} + S_{1982})/2} \tag{4.3}$$

The ΔS/S values for the low-redshift sample are listed in Table 4.2. This statistic must be taken only as a rough estimate of a source's true variability due to the unpredictable nature of most quasar light curves.

A more general way to estimate the variability of objects in a sample was developed by Gregorini *et al.* (1986). If the fluxes at two epochs are have errors $S_1 \pm \sigma_1$ and $S_2 \pm \sigma_2$, then the standard error of the difference in fluxes $\sigma_{\Delta S}$ is

$$\sigma_{\Delta S} = ((\sigma_1)^2 + (\sigma_2)^2)^{1/2} \tag{4.4}$$

Gregorini *et al.* showed that the distribution of $\Delta S/\sigma_{\Delta S}$ for their sample was a Gaussian, allowing them to determine the probability that a value of $\Delta S = |S_2 - S_1|$ was due to

observational error. For a Gaussian with standard deviation $\sigma_{\Delta S}$, the confidence levels for various values of $\Delta S/\sigma_{\Delta S}$, are shown in Table 4.1.

Table 4.1: Variability Confidence Levels

$\Delta S/\sigma_{\Delta S}$	Probability of ΔS being due to observational error
> 3.29	0.1%
> 2.81	0.5%
> 2.58	1%

In my analysis, I have deemed a source to be variable if $\Delta S/\sigma_{\Delta S} \geq 3.29$ (the 99.9% confidence level), and have assigned a 'probably variable' designation for those sources with $\Delta S/\sigma_{\Delta S} \geq 2.58$ (the 99% confidence level). The results of this analysis are found in the column of Table 4.2 marked 'Variable'.

Table 4.2: Variability Data

Object	6 cm	6 cm (1982)	Weak Core?	Variable	ΔS/S	Spectral Index (6-2 cm)
0007+106	590	470		PV	0.23	0.81
0017+257	299	310			0.04	0.16
0041+119	20	17	WC		0.15	-0.08
0137+012	178	150			0.17	-0.08
0241+622	256	300	WC		0.16	-0.27
0736+017	1882	2240			0.17	0.35
0742+318	656	640			0.02	-0.07
0829+047	1065	656		V	0.48	0.36
0846+100	5.6	6	WC		0.07	0.25
0952+097	7.8	7	WC		0.11	-0.32
1004+130	30	12	WC	V	0.87	-0.04
1020-103	367*	330*			0.11	-0.92
1028+313	83	110	WC	V	0.28	0.24
1203+011	154	170	WC		0.10	-0.27
1217+023	330	320			0.03	-0.03
1223+252	3.5	4	WC		0.13	0.58
1243-072	869	1300		V	0.40	0.11
1302-102	982	1185		PV	0.19	-0.05
1525+227	39	43	WC		0.10	0.38
1635+119	36	17	WC	V	0.72	-1.37
1721+343	386	370			0.04	-0.56
1725+044	634	730			0.14	-0.06
1739+184	32	25	WC	V	0.25	-0.83
2135-147	136	126			0.08	0.13
2141+175	918	280		V	1.07	-0.01
2201+315	3696	1500		V	0.85	0.13
2217+08N	27	27			0.00	0.03
2217+08S	12	7	WC	V	0.56	-0.29
2247+140	1277*	1210*			0.05	-1.07
2305+187	70	81			0.15	-0.38
2328+167	41*	25*			0.48	-1.70
2331-240	1197	910	WC	V	0.27	0.11
2355-082	89*	110*			0.21	-0.71

Notes on Table 4.2:

V = variable at 99.9% confidence level

PV = variable at 99% confidence level

* = flux uncertain due to the presence of nearby extended structure.

WC = weak core: 6 cm core luminosity (1984) < $10^{24.5}$ W Hz^{-1} (see §4.4.1)

4.3. Variability Distributions

4.3.1. Overall Distribution

The distribution of ΔS/S values for the sample is shown in Figure 4.1. Out of the 33 objects for which two-epoch data was available, 10 were deemed variable at the 99.9% confidence level, with 2 more possibly variable sources at the 99% level.

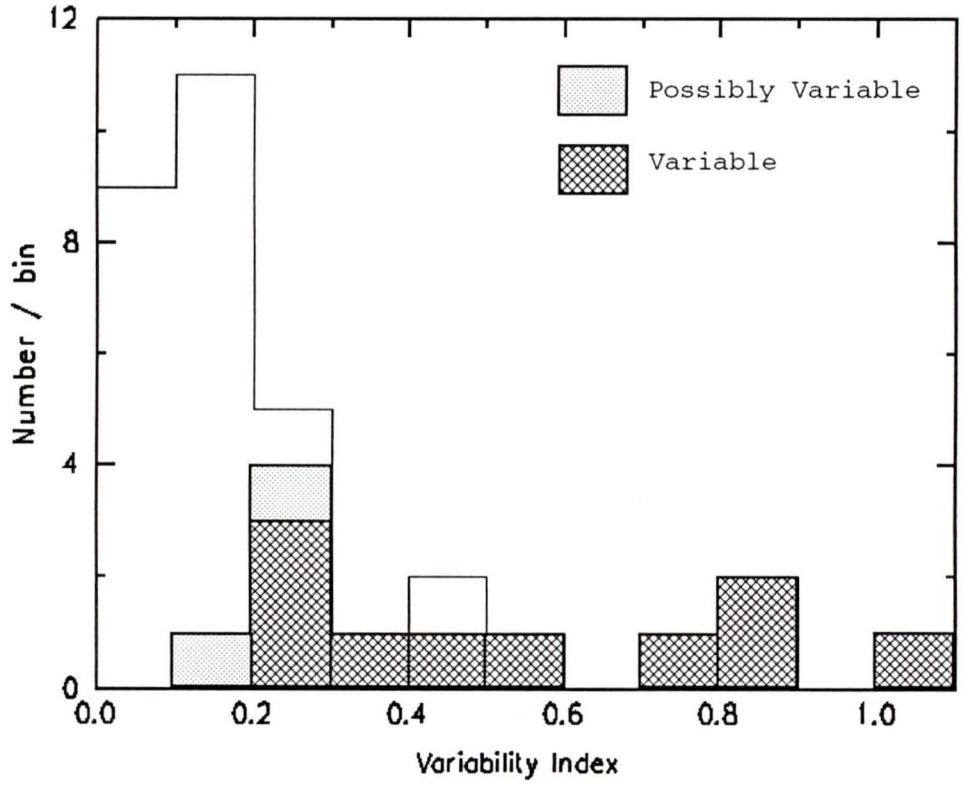

Figure 4.1: Variability Index Distribution

4.3.2. Distributions for Different Source Morphologies

In Table 4.3 I present the variability statistics for different radio morphologies. The most noteworthy aspects of this table are that the cores of triple sources are quite variable, while none of the one-sided lobe sources displayed any appreciable variability. There does not appear to be any appreciable correlation between radio size and variability however, as shown in Figure 4.2.

The variability in the triple sources is quite interesting as these sources are not expected to have their cores beamed at us. As a further test of beaming, I have plotted in Figure 4.3. the core fraction parameter against the variability indices for the sample. The core fraction, discussed in more detail in Chapter 6, is defined as the ratio of core to total flux, and is predicted to be much higher for beamed sources. I do not find strong evidence for this in Figure 4.3. When the sample is divided into roughly equal groups with $f_c > 0.5$ and $f_c < 0.5$, a Kolmogorov-Smirnov (K-S) test gives a coefficient of only 0.36, implying that these two groups are different in their variability properties at a confidence level of only 71%. I also investigated and did not find any correlation between variability index and core luminosity for the sample.

Table 4.3: Variability Statistics for Different Morphological Classes

Morphology	Variable	Possibly Variable	Non-Variable
Core	2	1	1
Core + Lobe	0	0	6
Triple	8	1	14

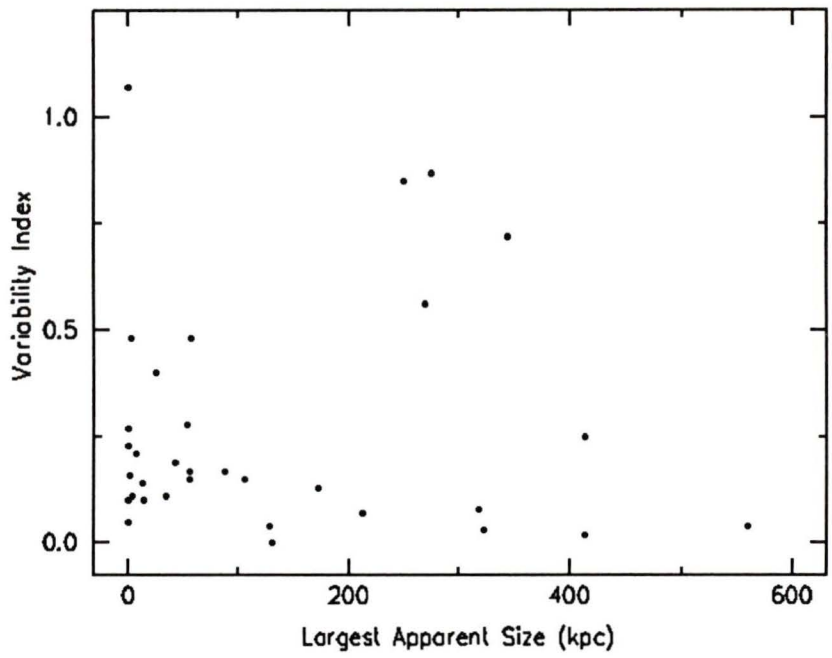

Figure 4.2: Variability Index vs. Largest Apparent Size

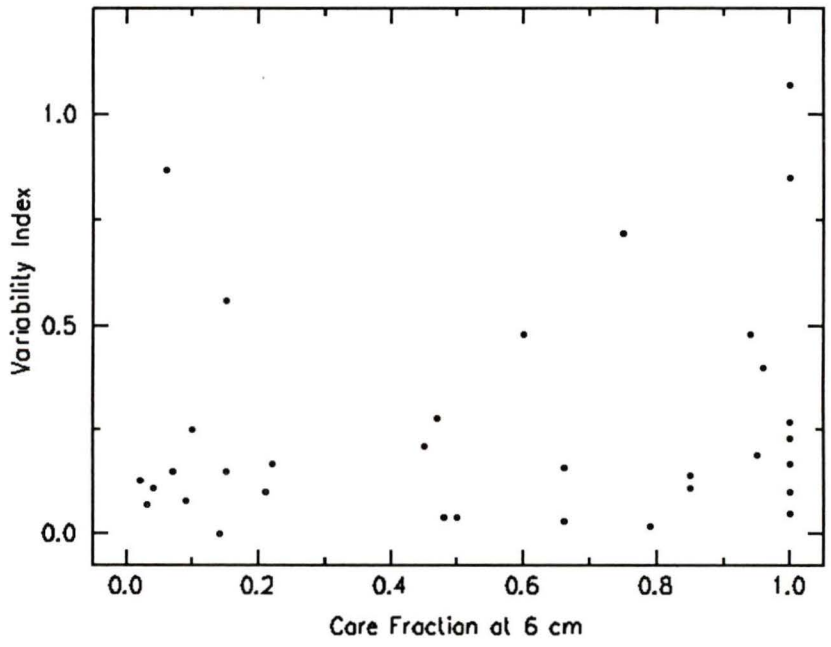

Figure 4.3: Variability Index vs. Core Fraction at 6 cm

4.4. Core Spectral Indices

It is well known that the radio spectra of most quasars can be described by a power law $S \propto \nu^{\alpha}$, where α is the spectral index. This power-law form is thought to be a result of the relativistic energy distribution of the synchrotron-emitting electrons in the central core.

The observed values of α for radio quasars range from those of classical, steep-spectrum sources ($\alpha < 0$), to flat ($\alpha \cong 0$) or inverted ($\alpha > 0$) values. Although the most common interpretation of the last two classes is that they are affected by opacity effects such as synchrotron self-absorption, other authors have claimed that these sources may be beamed. This hypothesis was first put forward by Orr and Browne (1982) on the basis of relative differences in the observed number counts of flat- and steep-spectrum sources. Observations showing that sources with highly inverted spectra nearly always have small intrinsic sizes have also lent support to this model (Kellerman and Owen 1988).

Beaming however does not appear to be responsible for the flat spectrum of some quasars such as 0735+178. This source appears to contain many different components in its core whose spectra add up in such a way to give an overall flat spectrum. Since the probability of this occurring by chance appears unlikely, this observation has often been referred to as 'the cosmic conspiracy' (Cotton *et al.* 1980).

Due to possible beaming and opacity effects, very little is known about the intrinsic electron energy distribution and spectral indices of the core components. The extended structure however is optically thin and is not believed to be affected by beaming. Studies of radio lobes all appear to indicate that they have steep spectra, and generally have different α from the core component (Neff 1982a). This is what would be expected for an ensemble of electrons losing their energy through synchrotron radiation in an optically-thin region.

4.4.1. Correlations with Variability

Numerous studies to date have found evidence that flat- and inverted-spectrum radio sources (including both radio quasars and galaxies) are more variable than steep spectrum ones (Aller 1991, Edelson 1987, Heeschen *et al.* 1987). Unfortunately, the strength of these authors' conclusions is lessened by possible errors in their derived spectral indices. These were partly due to flux errors, and partly due to the inability of a single-dish telescope to resolve out the core from the extended components. Furthermore, the two or more measurements at different observing frequencies used to calculate α were often taken at different times, which can introduce large errors for variable sources. The low-redshift sample data of this thesis, having been taken simultaneously at 2 and 6 cm using the highest-resolution configuration of the VLA, do not suffer from these effects.

Figure 4.4 shows the spectral-index distributions for the variable and non-variable sources in my sample. There is no appreciable difference between the spectral-index distribution of the variable and non-variable sources, with a Kolmogorov-Smirnov test showing that they are different at a confidence level of only 14%. This discrepancy from the results of other authors appears to be due to the inclusion of sources with weak cores in the low-redshift sample. In Figure 4.4 I have shaded those sources having core luminosities at 6 cm less than $10^{24.5}$ W Hz^{-1}. This division was chosen so that the weak core group consisted almost entirely of low-luminosity cores embedded in extended triple sources. From Figure 4.4. it is apparent that nearly all of the variable, steep-spectrum ($\alpha < 0$) cores are weak.

If all the weak-cored objects are excluded from the sample, the spectral index distributions of the variable and non-variable sources do indeed differ at the 91% level using the K-S test, in accordance with the findings of the other authors mentioned above.

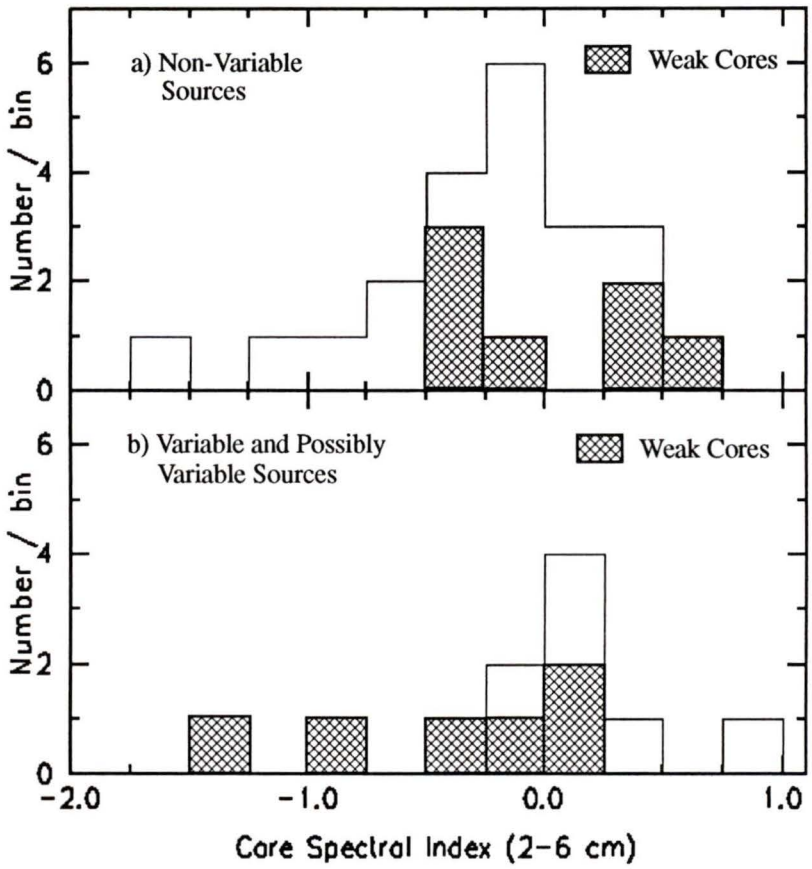

Figure 4.4: Spectral Index Distributions for Variable and Non-Variable Sources

4.5. Summary

Although the sample of objects in this analysis is small and only two epochs were used to determine variability, I nevertheless believe the results of this chapter to be highly significant. The data set is quite different from those used previously, in that it uses accurate core spectral indices and includes weak-cored objects.

If the morphological differences of the core and lobe dominated sources are merely due to orientation effects, the beaming model predicts differences in the variability properties of these two classes. However, in this chapter I have shown that the cores of both triple and core-dominated sources show signs of variability. Furthermore, the variability displayed by the weak-cored, steep spectrum sources appears to be in conflict with the simple beaming hypotheses mentioned earlier.

These findings can be reconciled by using the scheme of Barthel (1989) in which all quasars are oriented close to the line of sight. If further multi-epoch observations of the cores of triple sources were to show similar amounts of variability, this model would receive strong support. A variability study that included radio galaxies would also be very interesting, as these objects are believed by many authors to be un-beamed objects (Padovani and Urry 1992). Without an accurate means of determining the orientation of the core component however, it is difficult to assess to what degree flux variability may be intrinsic, rather than due to beaming (Duric, Gregory and Tsutsumi 1989). In the following chapter I will use numerical modelling experiments to show how the lobe morphology of quasars can be used as a statistical indicator of orientation.

Chapter Five:

Radio Lobe Orientation Models

5.1. Background

Many of the unanswered questions about the cores of radio quasars arise from uncertainties in the viewing angle to the source. For instance, it is not known what fraction of quasars suffer from the effects of relativistic beaming as a result of having their jet structures pointed directly at us. In this chapter I will explore the possibilities of using the lobe properties of radio quasars as an indicator of viewing angle through the use of simple geometrical modelling experiments.

In Figure 5.1 I have drawn a diagram showing a classical double-lobed or 'canonical' quasar seen face on. The two hotspots, marking the points at which the radio jets encounter the inter-galactic medium, are located at distances D_1 and D_2 from the central core of the quasar.

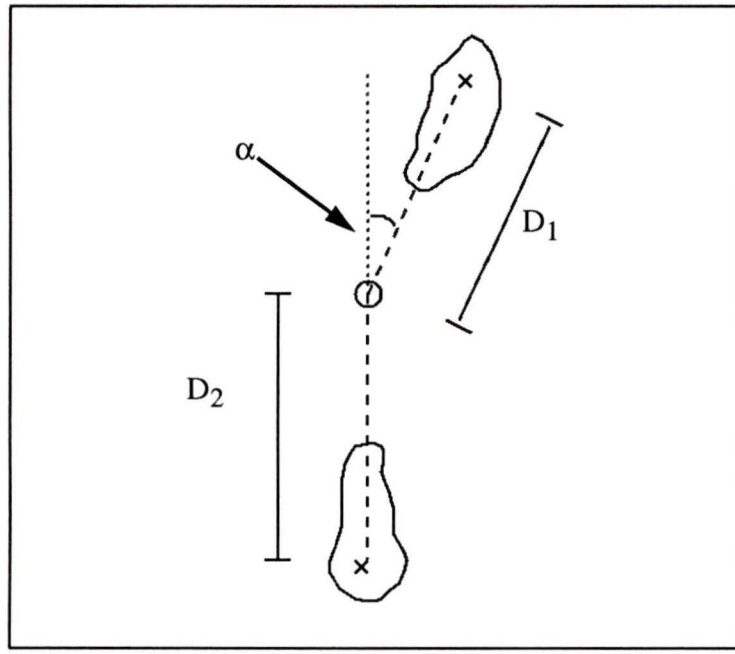

Figure 5.1: A Canonical Quasar

The core and the hotspots are usually non-collinear due to intrinsic bending of the jets, the origins of which will be discussed in §5.2.

If this canonical quasar is viewed end-on, two effects will be noticeable. Firstly, the apparent distance between the hotspots will be much smaller due to foreshortening, and secondly the apparent bend angle (α) will be greatly enhanced. A simple analogy for the latter effect is found when a carpenter looks down the end of a board to check for intrinsic bending or warpage.

For triple sources that resemble the canonical quasar in Figure 5.1, the apparent size and bend angle are relatively straightforward to measure (see §3.4). In many studies, authors have made use of the optical positions for quasars without detectable radio cores, and assumed that they are coincident with the core component. These positions can often be greatly in error, as indicated by the crosses in the maps in Appendix A, and can therefore yield inaccurate bend angles. For this reason I have only measured the bend angles for sources in my sample having triple (lobe-core-lobe) structure. Figure 5.2 shows a plot of largest angular size versus bend angle for these objects. There is a definite trend, first observed by Macklin (1981) that smaller sources have larger bend angles, implying that the distribution is strongly affected by viewing angle. Note the persistence of the trend when combined with measurements of sources from other surveys in Figure 5.3.

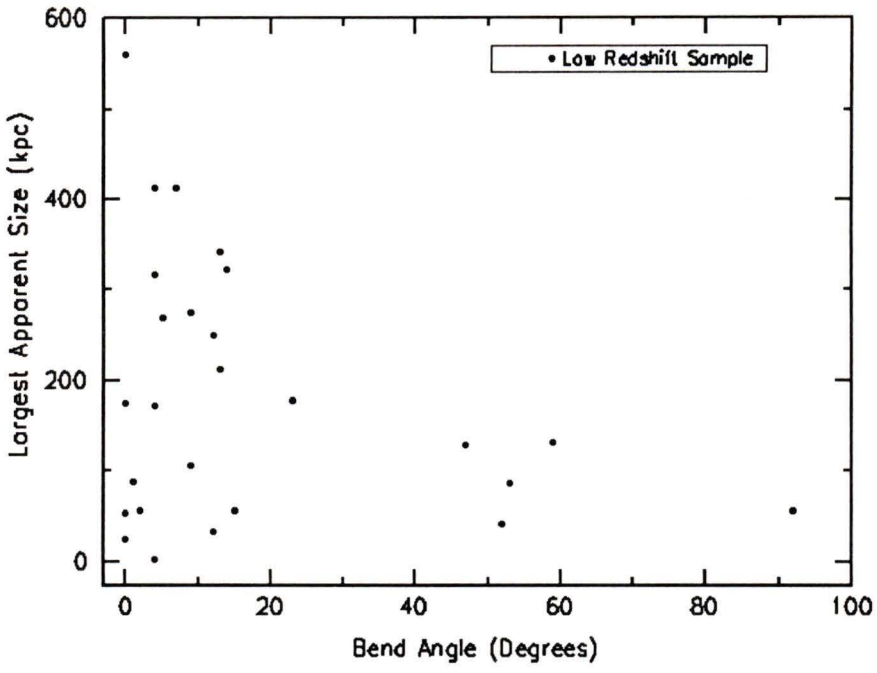

Figure 5.2: L.A.S. vs. Bend Angle for the Low Redshift Sample

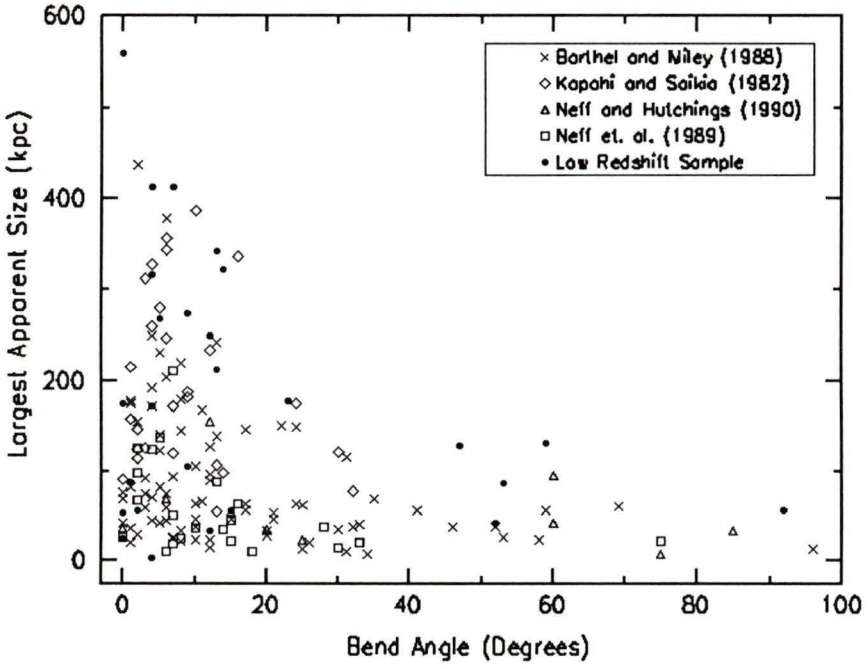

Figure 5.3: L.A.S. vs. Bend Angle Including Other Surveys

5.2. Numerical Modelling of Size-Bend Angle Relation

In their study of a small sample of 28 double-lobed radio quasars, Hough and Readhead (1989) showed that their observed size, bend angle and core fraction (see Chapter 6) distributions could be modelled by a sample of randomly-oriented quasars. Their analysis looked at the parameters individually however, and did not investigate the correlations between these variables. They also omitted any discussion of the core-hotspot distance ratio (Q), which I will show in §5.3 to be strongly correlated with orientation.

The initial goal of this chapter was to extend the work of Hough and Readhead by taking a set of canonical quasars as in Figure 5.1, randomly orienting them in space, and comparing the resulting size vs. bend angle distribution to the larger observational data set of 167 triple sources. These objects, all classified as quasars, are plotted in Figure 5.3, and comprise roughly 3/4 of the known objects in this class.

The first step in constructing the model required some assumptions about the intrinsic (de-projected) bend angle and linear size distribution of triple sources, since there are very few observational constraints on these parameters.

Since radio quasars are thought to have a large distribution of intrinsic sizes as a result of evolutionary effects (Neff and Hutchings, 1990), I chose a uniform distribution of core-hotspot distances from 0 to 280 kpc, the upper limit coming from the largest known quasar, 1721+343, which has a linear size of 560 kpc (Barthel, 1986). To keep the model as simple as possible, for each quasar the core-hotspot distance ratio Q was set to be unity (i.e. D_1=D_2).

Very little is known about the intrinsic bend angles of radio quasars due to uncertainties involving projection effects. Riley and Pooley (1978) suggested that the observed bends of triple sources could be due to motion of the source through the inter-galactic medium. There are several examples of 'narrow angle tail' sources (e.g. NGC 1265) that appear to have their radio lobes swept back by such a process. However the majority of triple sources have very straight jet structures and small apparent bend angles that are not consistent with this explanation. Instead, many authors have claimed that the bends are

due to precession of the central engine (Gower and Hutchings 1982), or hydrodynamical instabilities in the jets that cause them to trace curved trajectories (Conway and Murphy, 1992). It has also been suggested that the bends are due to inelastic collisions of the radio jet with a nearby galaxy halo or cloud (Stocke *et al.* 1985). Due to these uncertainties regarding its origin, the intrinsic bend angle was left as a free parameter in the model.

5.2.1. Initial Results

As a first step, I calculated the observed size vs. bend-angle distribution for a randomly oriented set of canonical quasars all having an intrinsic bends uniformly distributed between 0-15 degrees (Figure 5.4).

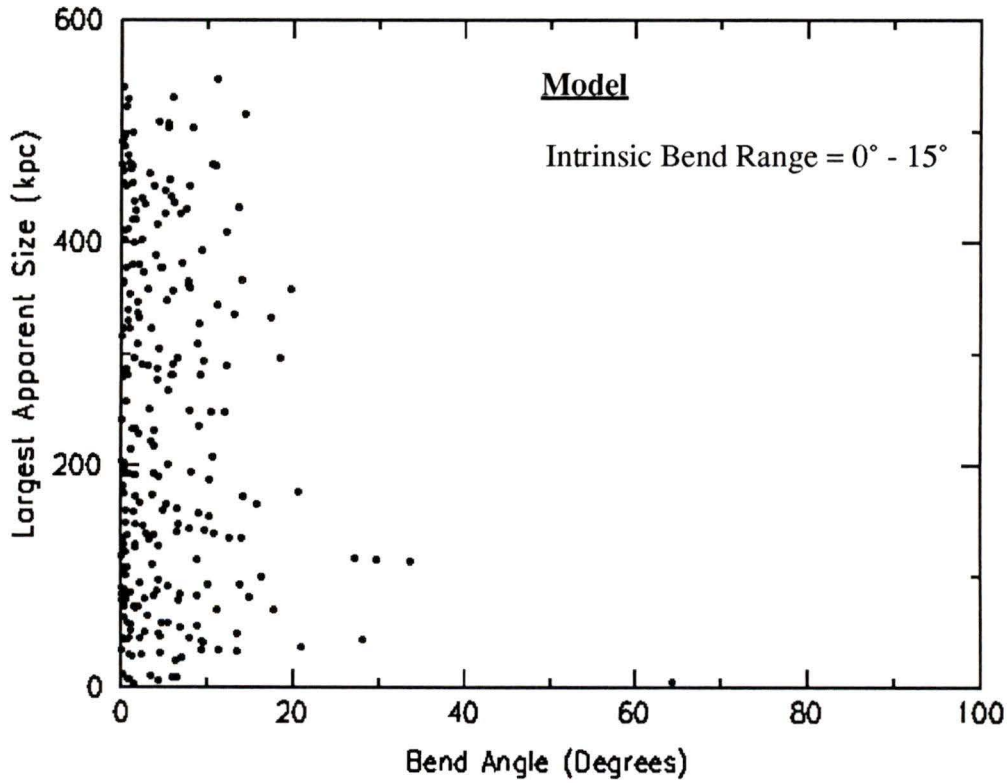

Figure 5.4: Size vs. Bend- Angle Distribution for a Randomly Oriented Population of Canonical Quasars With an Intrinsic Bend Range of 0-15 Degrees

When comparing Figure 5.4 to the observed distribution in Figure 5.3, it is readily apparent that the model contains a strong deficit of sources with large bend angles. This is simply a reflection of the fact that in a randomly-oriented sample, there is a much higher probability of seeing a source near the plane of the sky rather than end-on.

A possible explanation for the poor fit to the observational data is selection effects present in the quasar sample. According to the beaming model, sources pointed directly at us will have their apparent luminosity increased by Doppler boosting, making them more likely to be included in flux-limited samples. Since the combined sample in Figure 5.3 was selected from flux-limited optical and radio surveys, it is perhaps biased towards highly-inclined objects, thus changing the observed bend-angle distribution.

Another possible bias is that all the objects in the sample are radio quasars. It has been suggested that quasars are merely radio galaxies seen end on (Barthel 1989, Padovani and Urry 1992), so once again the sample could be biased against objects lying near the plane of the sky.

As a way of compensating for possible selection effects, I repeated the modelling experiments using a biased-orientation distribution. This was accomplished by excluding all canonical quasars that happened to have orientations greater than a certain angle (Φ) to the line of sight. A value of $\Phi = 90$ is thus equivalent to an unbiased distribution, while smaller values of Φ imply a larger bias. Of course, when an orientation bias is introduced, it reduces the maximum size that can be seen, so to produce results consistent with the data, I increased the upper range for the canonical quasar core-hotspot distance distribution to $280/\sin\Phi$ kpc.

Figure 5.5 shows the resulting distribution for a model with an intrinsic bend angle range of 0 to 15 degrees incorporating a line-of-sight cutoff of 45 degrees. The model produces a much better fit to the observational data, suggesting that there is indeed an orientation bias present in the radio quasar data.

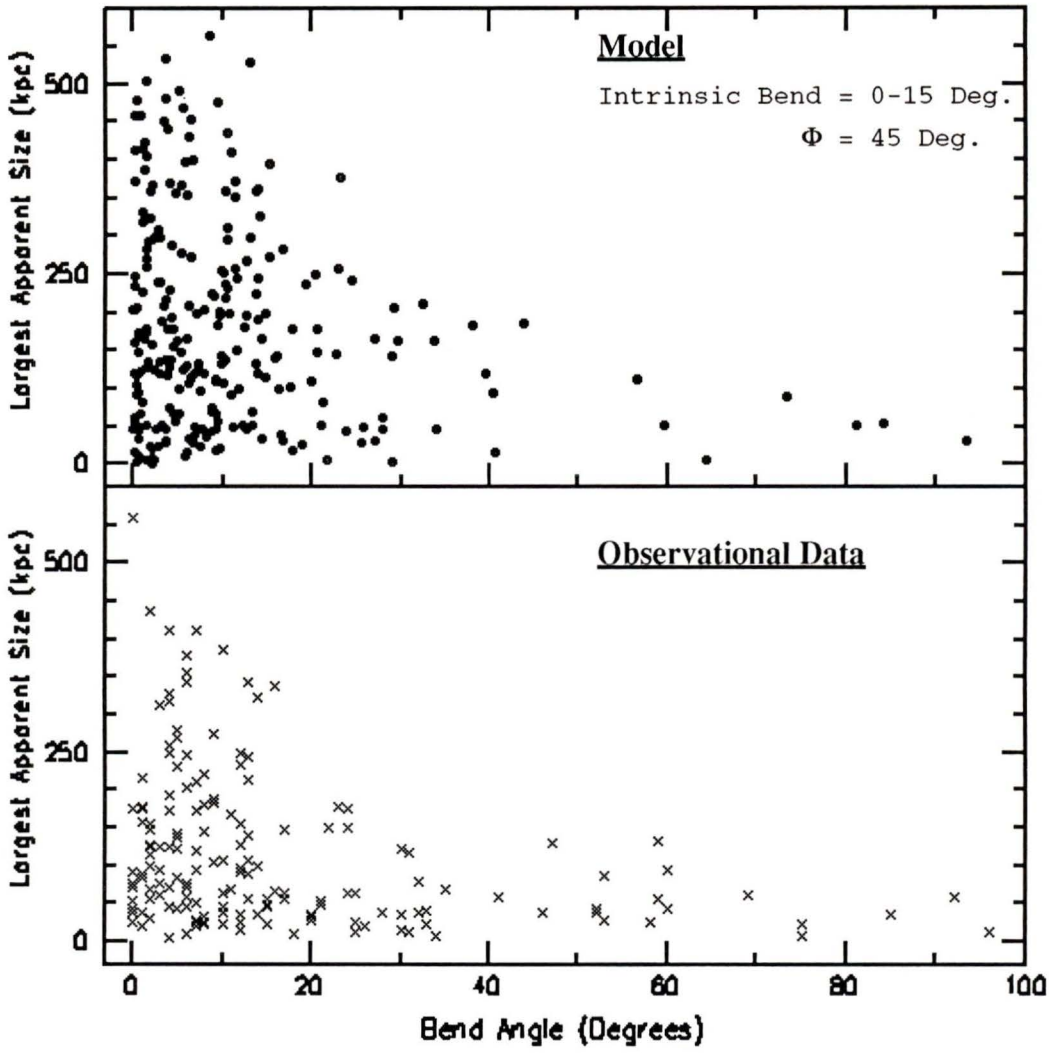

Figure 5.5: Comparison of Orientation-Biased Model With Observed Size vs. Bend-Angle Distribution

5.2.2. Testing of Fits

In order to test the accuracy of their model fits to the data, Hough and Readhead compared their projected size and bend-angle distributions separately with the observed distributions using a χ^2 test. I decided not to follow their procedure for several reasons. Firstly, the χ^2 test involves binning the data, which results in a loss of information, and the goodness of the fits can often be biased depending on how the bins are chosen. Secondly, the size and bend measurements often have large errors associated with them, and since the χ^2 test is very sensitive to points that differ greatly from the model predictions, it is not well suited for this data. Finally, in my model I wished to examine how the size and bend were correlated, so it was not logical to throw away information by looking at the two variables separately.

I therefore decided to use a version of the Kolmogorov-Smirnov test modified for use with two-dimensional distributions by Peacock (1983) and Fasano and Franceschini (1987). In the test, the size / bend-angle plane is divided into four quadrants at the position of the first observational data point. The number of observational data points in the first quadrant is calculated, and divided by the total number of observational data points to give a cumulative probability value. In the same quadrant, the number of model data points is calculated and divided by the total number of model data points to give a cumulative probability for the model points. The absolute value of the difference of these two probabilities is recorded, and the process is repeated for the other three quadrants. The plane is then divided into four quadrants at the position of the next observational data point, and new differences are found. The largest difference found by this method is known as the D statistic, and is a measure of how well the two data sets are correlated. For completely uncorrelated data sets lying in different parts of the plane, the D statistic will be very close to one, so a *low* value of D implies a better fit to the data. When comparing a random distribution to the observed data set, consistent values of D=0.66 were obtained. To be considered a good fit therefore, a model should have a D value significantly *lower* than this value.

5.2.3. Quantitative Comparisons of Fits

The two free parameters in my model are the intrinsic bend and line-of-sight cutoff angle Φ, and in this section I describe my investigation into which combinations of values provide the best fits to the observed size vs. bend-angle distribution of Figure 5.3.

My procedure was as follows:

1. A value for the intrinsic bend angle was chosen (e.g. 5 degrees).
2. An initial value of $\Phi = 20$ degrees was chosen for the line-of-sight cutoff angle.
3. Using these parameters, a model distribution was calculated and compared with the observed data in the manner described in §5.2.2, to obtain an estimate of fit (D_b) value.
4. Step 3 was repeated five times using different random number seeds, and the D_b's were then used to give an average value.
5. The line-of-sight cutoff angle Φ was incremented by two degrees, and steps 3 and 4 were repeated until Φ reached 90 degrees.
6. The average D_b values for each Φ were plotted, and a cubic spline was then fit to the points (Figure 5.6).
7. A new value for the intrinsic bend angle was chosen, and steps 2 through 6 were repeated.

When calculating the average D_b of the five iterations in step 4, the mean standard deviation of the D_b values was ~ 0.03, so it is important to note that when comparing the models in Figure 5.6, differences less than this value are not significant.

With the exception of the models having an intrinsic bend of 15 degrees, the best fits in Figure 5.6 all occur for $\Phi < 90$ degrees, suggesting that there is indeed some form of orientation bias present in the data.

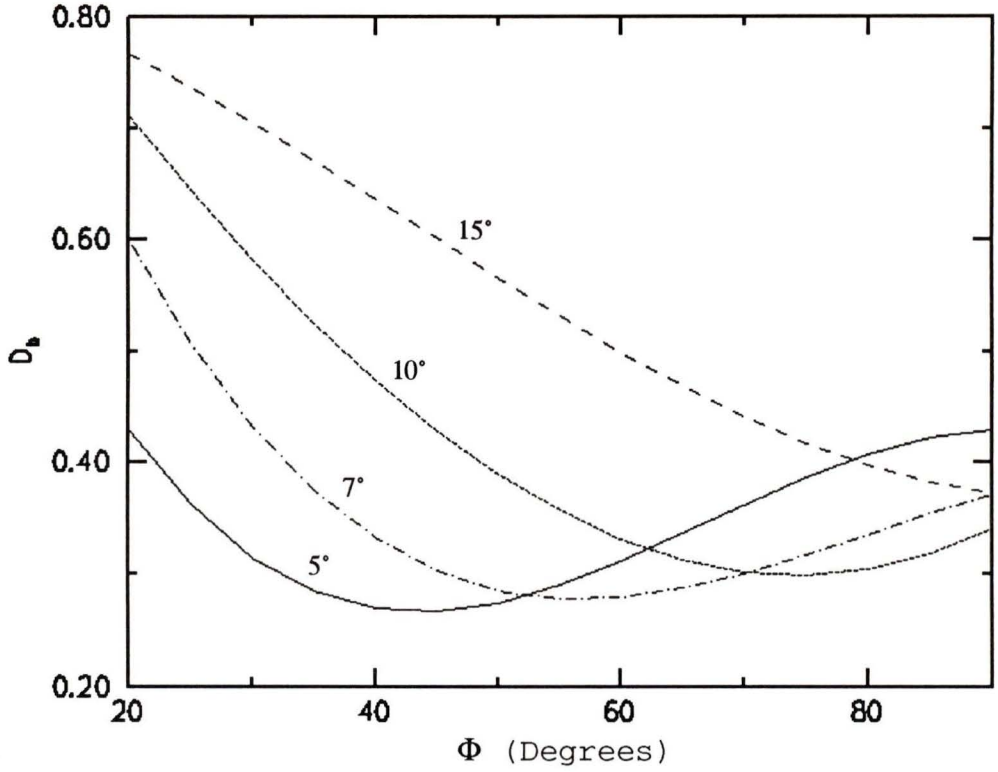

Figure 5.6: Fits of Orientation-Biased Models to Size vs. Bend-Angle Distribution (Single Values of Intrinsic Bend Angle)

In addition to individual values, I also investigated using different ranges for the intrinsic bend angle of the canonical quasars. The results are shown in Figure 5.7. The quality of fits are very similar to those using individual values, and these models are more likely to reflect the true distribution of intrinsic bends in radio quasars.

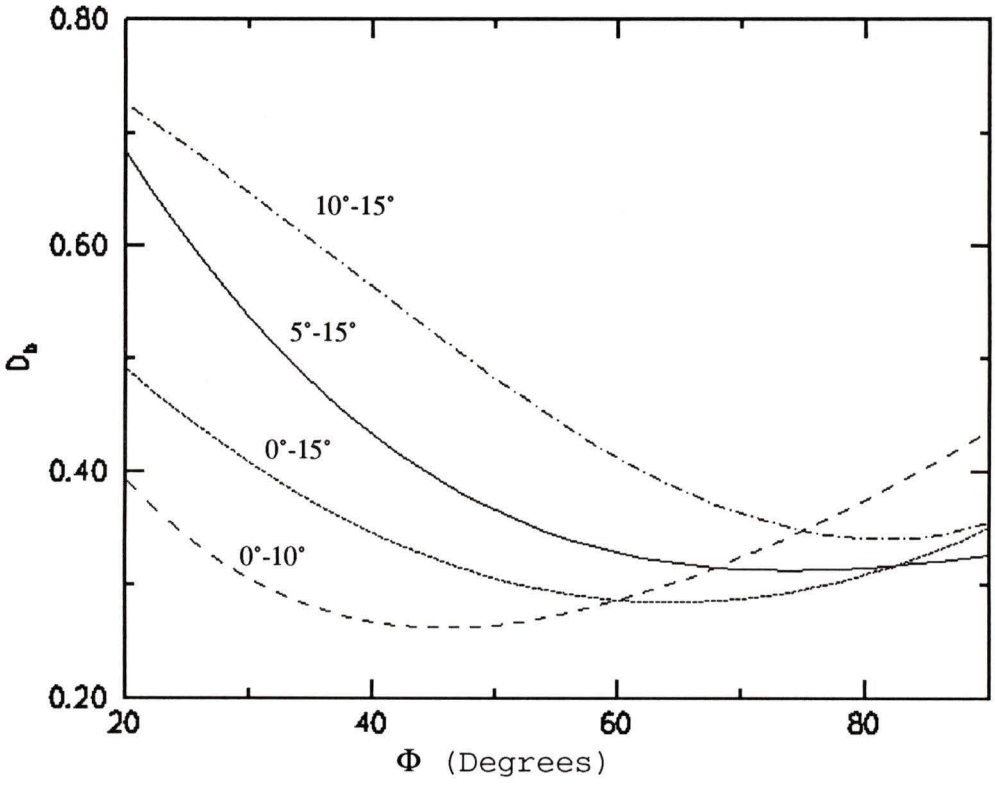

Figure 5.7: Fits of Orientation-Biased Models to Size vs. Bend-Angle Distribution (Ranges of Intrinsic Bend Angle)

5.3. Numerical Modelling of Size vs. Hotspot-Distance-Ratio Relation

Another prediction to come out of my numerical modelling experiments is that intrinsically bent quasars seen end-on will appear to have unequal core-hotspot distances due to the aforementioned projection effects. Since end-on sources will also have smaller apparent sizes, there should be a relation between the core-hotspot distance ratio ($Q = D_1 / D_2$) and the largest apparent size. These two quantities are plotted in Figure 5.8.

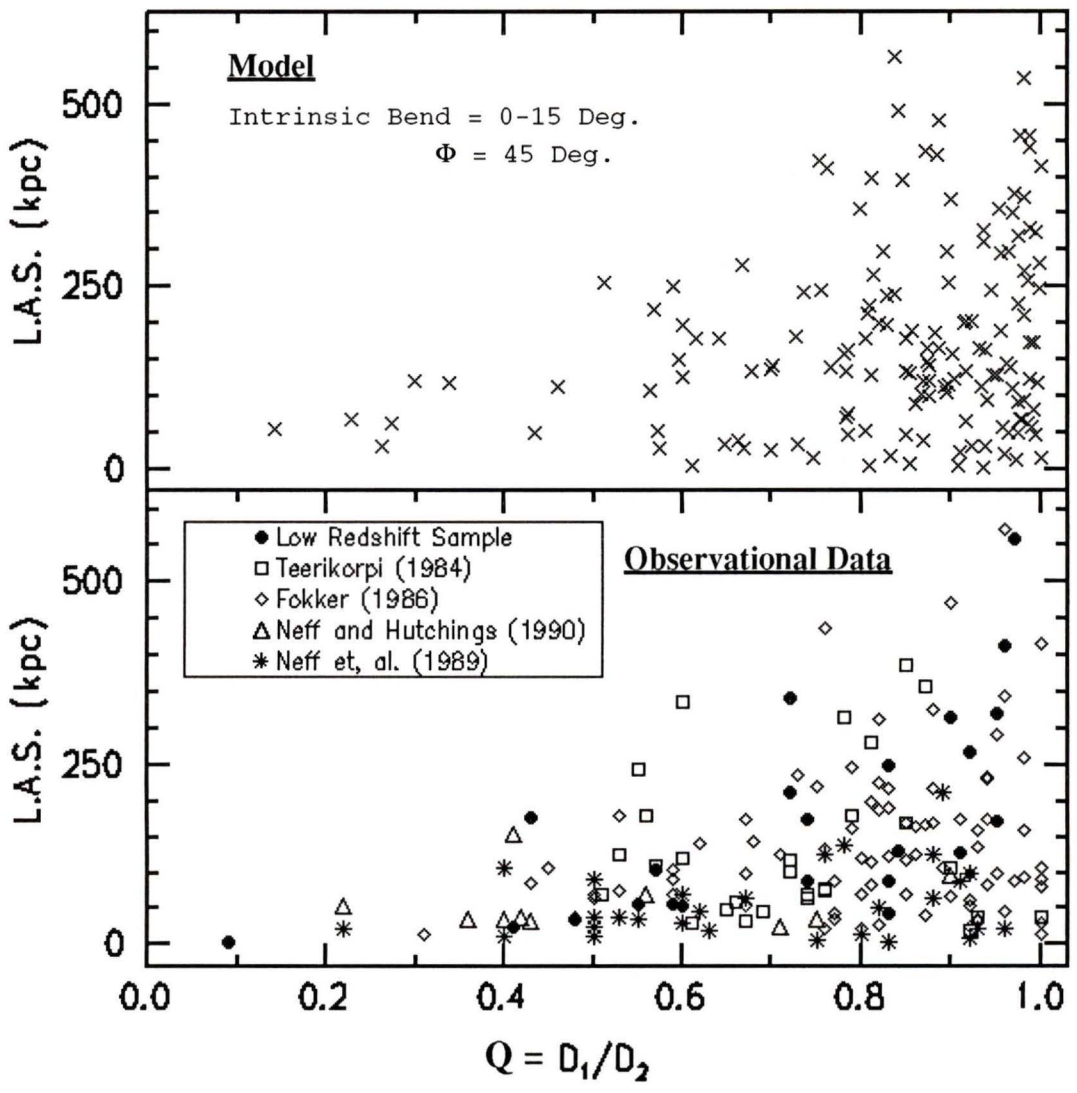

Figure 5.8: Comparison of Orientation-Biased Model With Observed Size vs. Q Distribution

This figure contains measurements for the triple sources in the low-redshift sample and others collected from the literature. It is important to note that the canonical quasars plotted in the top half of the figure are the exact same ones as in Figure 5.5. This is a strong indication that projection effects are the dominant factor in determining the morphological appearance of radio quasars.

I have compared the observational data to the models for different values of the free parameters in the exact same fashion as §5.2.3. The values of D_Q for various intrinsic bends and values of Φ are shown in Figure 5.9.

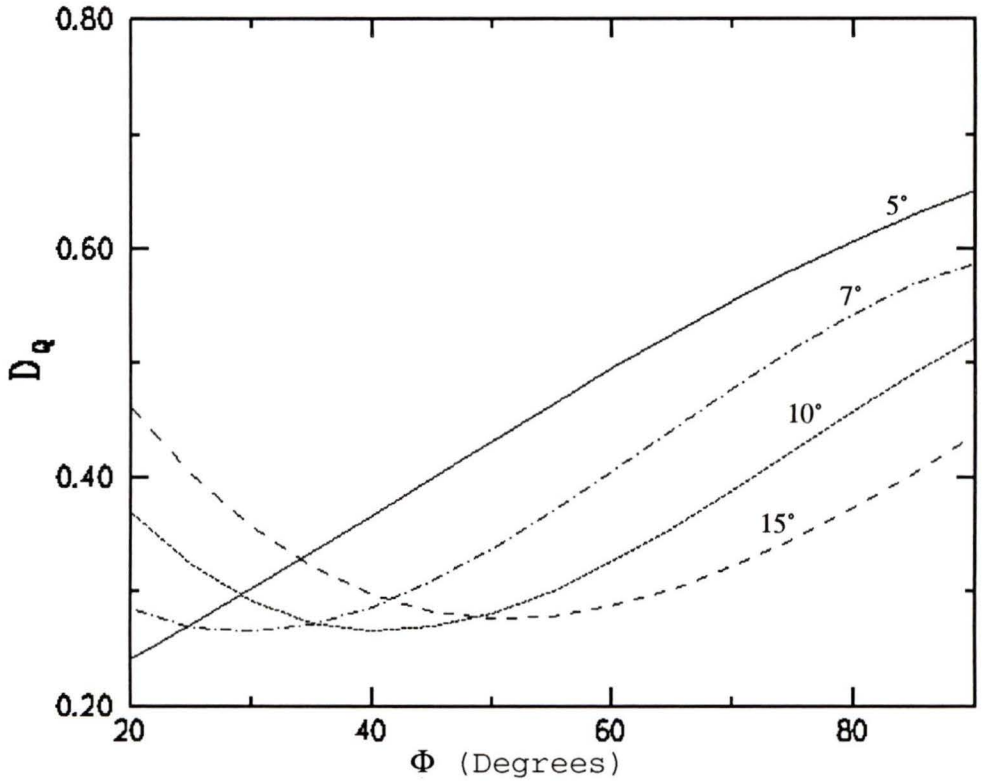

Figure 5.9: Fits of Orientation-Biased Models to Size vs. Q Distribution (Single Values of Intrinsic Bend Angle)

Once again, there is no appreciable difference between the fits using single intrinsic bends (Figure 5.9) and those using ranges (Figure 5.10). In both cases however, the best fits all occur for values of $\Phi < 90$ degrees, as was the case in the size vs. bend-angle mod-

els. In general, if quasars have small intrinsic bend angles, large numbers of sources near the plane of the sky must be excluded from the model (by decreasing Φ) to obtain a good fit to the data.

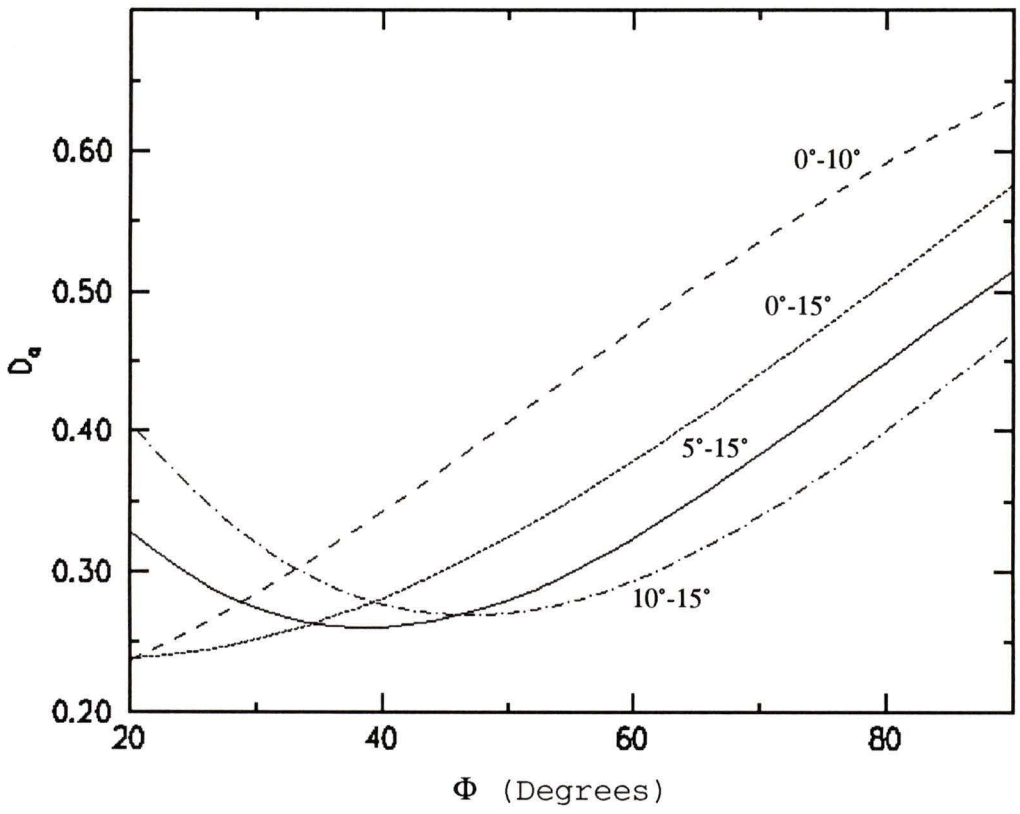

Figure 5.10:Fits of Orientation-Biased Models to Size-Q Distribution (Ranges of Intrinsic Bend Angle)

5.4. Fits to Both Size vs. Bend-Angle and Size vs. Q Distributions

As a way of determining which models best fit the observational size vs.bend angle and size vs. Q distributions, I have summed the D_b and D_Q statistics for each model and plotted them in Figure 5.11. It is difficult to characterize an 'absolute best' model, as the goodness of the fits depend on the range of Φ being examined. There are three clear minima however at (Φ= 60°, bend =10°); (Φ= 45°, bend = 7°); and (Φ= 32°, bend=5°).

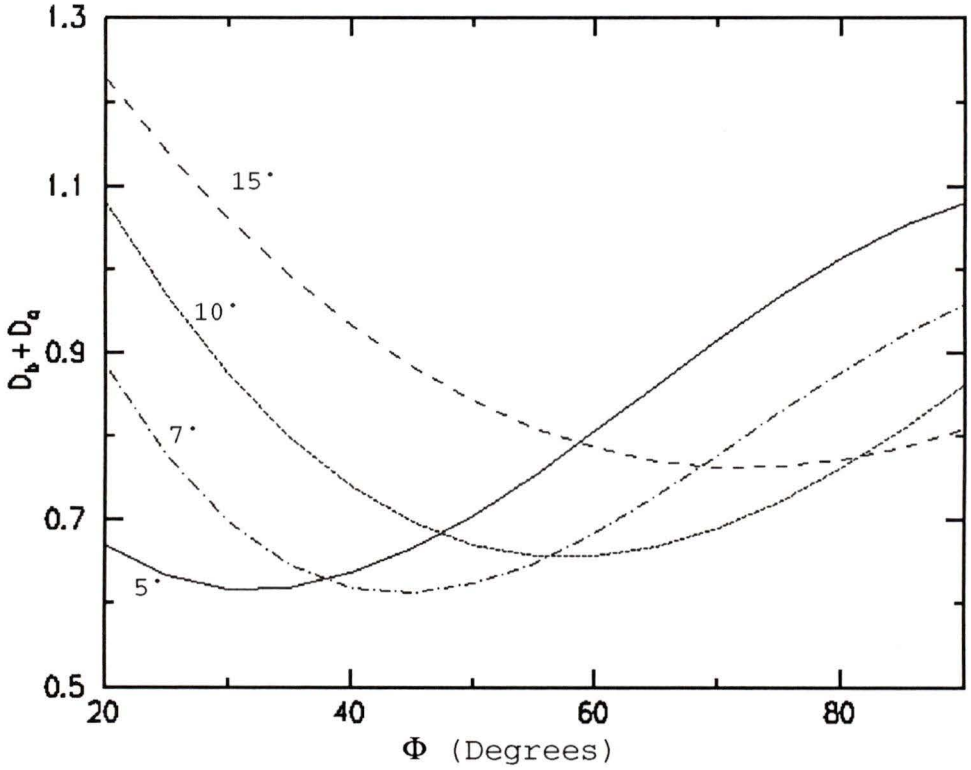

Figure 5.11: Fits of Orientation-Biased Models to Size vs. Q and Size vs. Bend-Angle Distributions (Single Values of Intrinsic Bend Angle)

The models with a range of intrinsic bend angle are not appreciably different than those of Figure 5.11, and have minima at (Φ= 31°, bend = 0°-10°); (Φ= 45°, bend = 0°-15°); and (Φ= 54°, bend = 5°-15°). Since all of these models provide equally good fits to

the data, I have arbitrarily chosen the (Φ= 45°, bend = 0°-15°) model to display in Figures 5.5 and 5.8.

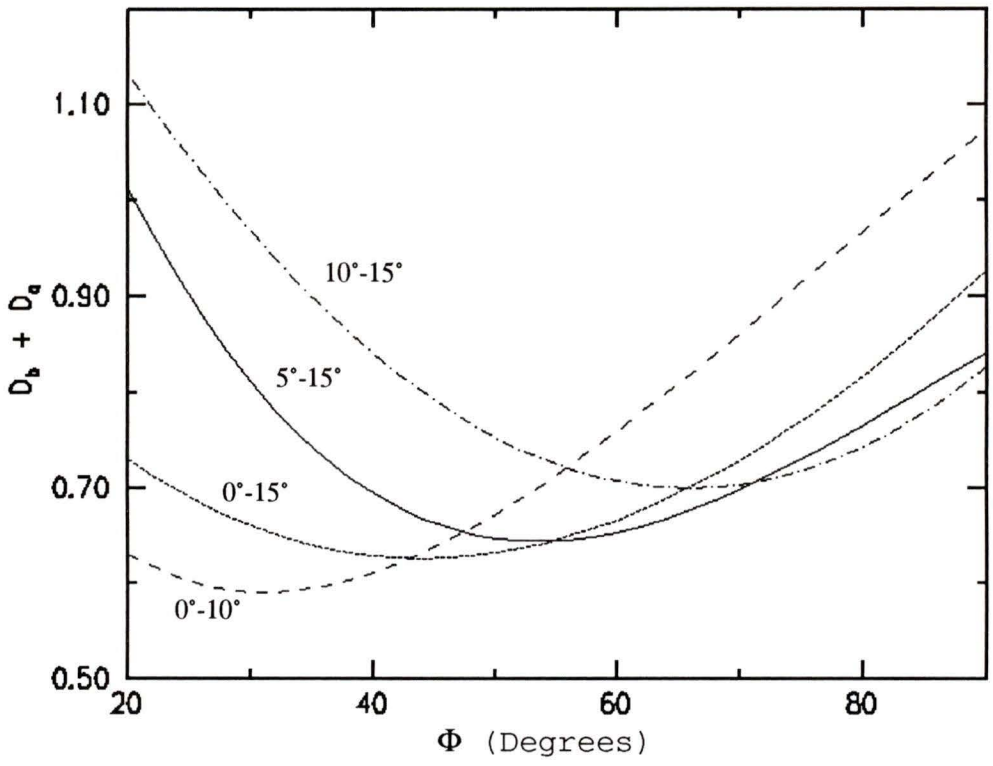

Figure 5.12: Fits of Orientation-Biased Models to Size vs. Q and Size vs. Bend Angle Distributions (Ranges of Intrinsic Bend Angle)

5.5. Alternating Ejection

Several authors have used the observed distribution of Q values for triple sources as evidence for alternating ejection in radio quasars (Ensman and Ulvestad 1984, Hutchings, Price and Gower, 1988). If jets of quasars are not being simultaneously emitted from opposite sides of the central engine, there should be a notable lack of sources with equal core-hotspot distances. As can be seen in the lower half of Figure 5.13, this dip is indeed observed. However, in the top half of the same figure I have plotted the Q distribution for the model plotted in Figures 5.5 and 5.8. Although in the model the intrinsic Q value is unity for all sources, most have an intrinsic bend angle. Introducing a bias favouring objects oriented 'end-on' makes it more likely for them to have apparently unequal core-hotspot distances due to projection effects. The result is a dip at unity, which becomes deeper as one excludes more sources lying near the plane of the sky (by decreasing Φ). If radio quasars do indeed suffer from an orientation bias, caution should be exercised when using this dip to estimate alternating-ejection parameters in extragalactic radio sources.

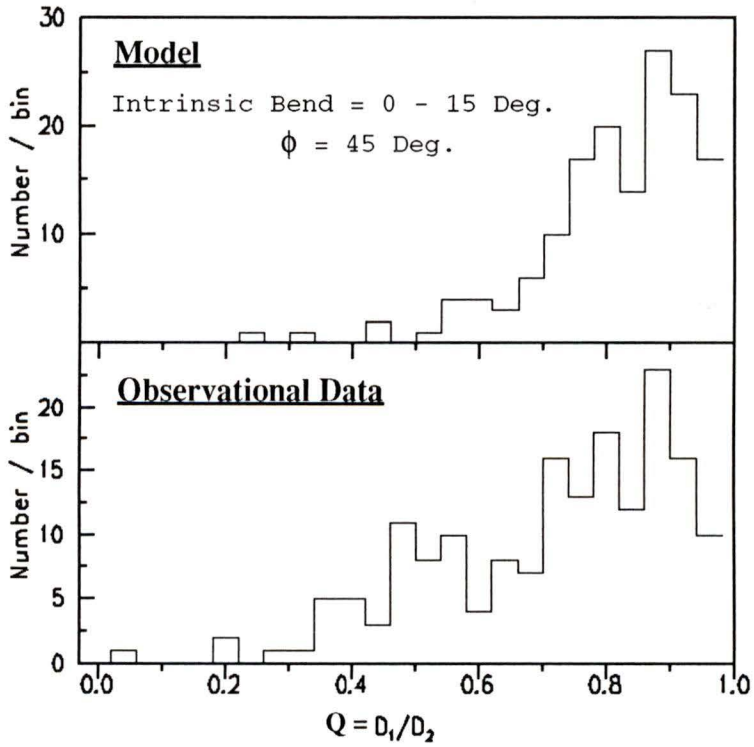

Figure 5.13: Q Histograms Showing Dip at Unity

5.6. Discussion

Although there are admittedly many environmental and evolutionary effects that can greatly change the observed morphology of radio quasars, the results presented in this chapter suggest that the effects of orientation might be dominant in this regard. The most convincing evidence comes from the fact that my biased-orientation model needs no modifications to explain both the size vs. bend-angle and size vs. Q distributions.

Perhaps the most questionable aspect of the model is the use of the line-of-sight cutoff Φ. Since the sources in the combined sample have all been identified optically as quasars, the implication is that the different classes of active galactic nuclei are related to viewing angle. Barthel (1989) and others have suggested that this may be due to an obscuring dust torus that blocks the bright continuum radiation and broad line region in objects seen in the plane of the sky. This theory, which traces back to Scheuer and Readhead (1979), remains highly controversial. The majority of current debate is focussed on the 'parent population' of the quasar class. If quasars are all aligned to within some angle to the line-of-sight, then there must be a large number of radio sources lying in the plane of the sky. These objects would have smaller bend angles, larger apparent sizes, and a higher number density than radio quasars. As radio galaxies generally satisfy all of the above criteria (Kapahi 1990), they have been postulated as the most likely candidate for the parent population (Browne 1983, Barthel 1986). There are, however, some observations showing differences in these two groups that cannot be accounted for by the orientation hypothesis. These include differences in [O III] linewidths (Scheuer 1987) and properties of the host galaxies (Hutchings 1987).

One observation often used in support of orientation bias is the occurrence of one-sided jets in large radio quasars. In a study of bright radio sources, Wardle and Potash (1984) found all of the eight largest doubled-lobed quasars to have one-sided jets. Unless these sources are undergoing some form of alternating ejection making them intrinsically one-sided, they must be suffering from the effects of relativistic beaming. A natural explanation to Wardle and Potash's findings is that the radiation from the counterjet is beamed

away from the observer, which requires the quasars to be oriented close to the line of sight. This is also consistent with the observation that superluminal sources nearly always have one-sided jets (Bridle, 1990).

Another very important discovery was made by Garrington et al. (1988), who found that in triple sources, the lobe opposite the jet side is always strongly depolarized. The most common interpretation of this is that radiation on the jet side, being pointed at us, has to travel through less intervening material than the far lobe, and therefore retains its polarization.

Putting the current debate over relativistic beaming aside, I have in this chapter presented evidence that orientation is indeed a dominant factor in determining the observed morphology of quasars. It follows therefore that the size, bend angle, and Q parameters can be used as statistical indicators of orientation, and in the next chapter I will investigate this hypothesis by looking for correlations with the core properties of the low-redshift sample.

Chapter Six:

Core Properties and Viewing Angle

6.1. Introduction

In the previous chapter I discussed how the observed size and bend angle of a quasar can be used as statistical indicators of radio-lobe orientation. Of more interest to the relativistic beaming model however is the orientation of the central core component, since it is believed to be responsible for the majority of the luminosity and variability seen in radio quasars. The best indicator of core orientation available at present is the superluminal motion of luminous components in radio cores observed with Very Long Baseline Interferometry (VLBI) techniques. The most widely-accepted explanation of this effect assumes that the components are moving at relativistic velocities at angles very close to the line of sight. Finding a source to be superluminal would thus provide strong evidence that its core was beamed towards us. Its large-scale structure would be expected to have small apparent size, low Q and a large bend angle. However, studies have shown that there appears to be nothing special about either the optical spectra (Lawrence et al., 1987) or the extended structures of superluminals (Browne, 1987). As a group, they contain the same variety of source morphologies as other samples of radio quasars, leading many authors to believe that this phenomenon is common among radio quasars (Browne 1987, Pearson et al. 1987, Zensus and Porcas 1987). Indeed, only a few sources have been shown to have sub-light speeds (Marscher, 1987), while the list of superluminals has grown steadily from 4 to approximately 35 sources over the last decade.

If the explanation for superluminal motion is correct, then the ubiquity of superluminal motion would suggest that all quasars are oriented close to the line of sight, in accordance with the conclusions reached in Chapter 5. This last point assumes that the small-scale, VLBI jets in the core are aligned with the extended (lobe) structure. Although this appears to be the case for the majority of high-luminosity radio sources (Browne 1987, Pearson

1990), there are several documented cases (e.g. 3C 309.1, 3C 216, 3C 345) of strong misalignments (Schilizzi and de Bruyn 1983, Pearson and Readhead 1988).

6.2. The Core Fraction

One parameter that has been used extensively in testing the beaming model is the ratio of core to total flux, where the total flux is the sum of the core and extended (lobe) fluxes. In the simple beaming picture, the jet velocity is relativistic (high β and γ, where $\beta = v/c$ and $\gamma = (1-\beta^2)^{-1/2}$) and therefore the flux from the core is highly collimated and Doppler boosted by a factor of $\gamma^{-3}[1-\beta\cos\theta]^{\alpha-3}$ where θ is the difference in angle between the velocity vector of the jet and the line of sight. The lobe emission, coming from slower-moving material, is less collimated and is not appreciably affected by Doppler boosting. Thus, the ratio of core to total flux should be much larger for sources with cores aligned close to the line of sight.

This prediction has been borne out somewhat by the superluminal sources, which show a strong positive correlation between the core fraction and the apparent superluminal velocity (Hough and Readhead 1987). Fanti and Fanti (1987) have also found that the core fractions of quasars are roughly two orders of magnitude larger than those of radio galaxies. However, using the core fraction as a test of the beaming model is difficult, for several reasons. Firstly, nearly all radio cores display some degree of variability, making it impossible to obtain a true measure of the core fraction. Secondly, interferometers give good core-flux measurements, but are not suited for measuring the total flux due to the lack of short antenna spacings (Chapter 2). Thus, data from single dishes must be used to obtain the total flux. These measurements are generally taken at different times from the core-flux observations, which can introduce errors for variable sources. In addition to being less accurate, single-dish fluxes are often measured at a different observing frequency than that of the interferometer data, requiring flux estimates to be made from log (flux) versus log (frequency) plots in the manner described in Chapter 3.

6.3. Size - Core Fraction Relation

6.3.1. Relativistic Beaming Interpretation

In Chapter 5 we found evidence that the apparent size of a quasar is strongly dependent on its viewing angle. The beaming model would therefore predict that on average, smaller sources, being pointed at us, would experience Doppler boosting of their core luminosity, and would therefore have larger core fractions. Indeed, such a relation, first described by Kapahi and Saikia (1982), appears to be present in the low-redshift sample data (Figure 6.1).

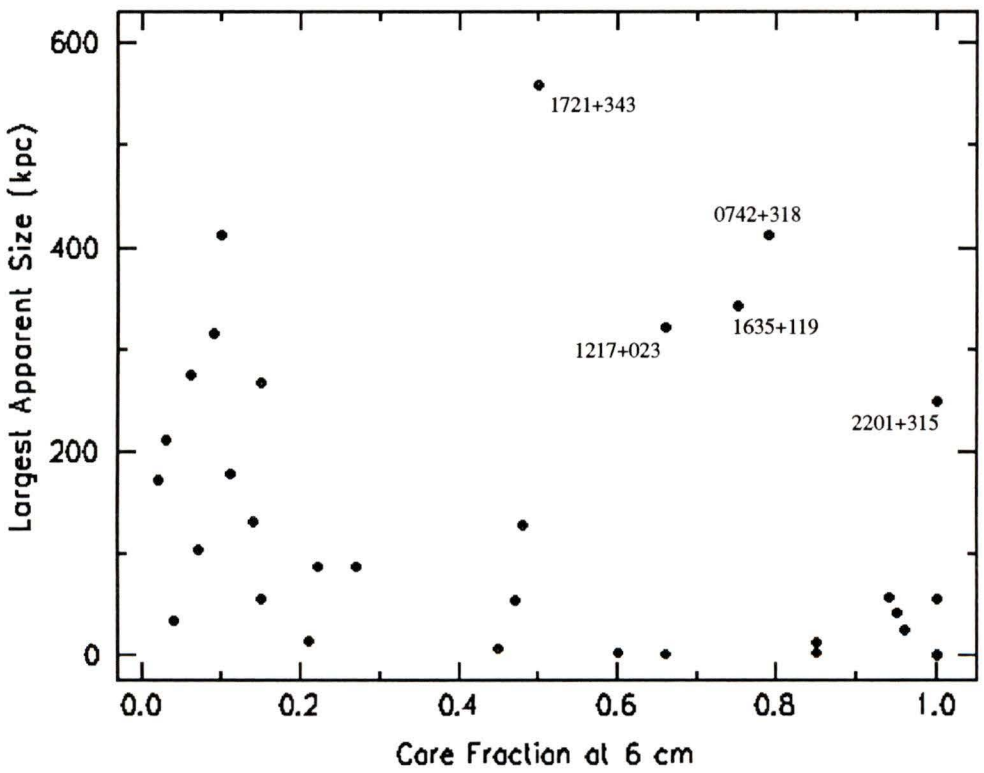

Figure 6.1: Size vs. Core Fraction Distribution(6 cm)

The predicted trend of smaller sources having larger core fractions is evident, with the exception of the five quasars labelled. These five sources all appear to have overly large

core fractions for their apparent size. The core fractions for 1721+343, 0742+318 and 1217+023 are all in agreement with those previously obtained by Jägers et al. (1982) and Neff (1982a). On the other hand, 2201+315 and 1635+119 are both highly-variable sources, making the measured core fraction less certain.

A satisfactory explanation for these discrepant sources has yet to be found. It is possible that they are sources with a beamed core component that is misaligned with the large-scale structure, or perhaps the core has undergone a burst of re-activity due to a recent merger event (Hutchings and Neff, 1992). At present however there is no way of distinguishing between these possibilities, so these sources must remain as oddities.

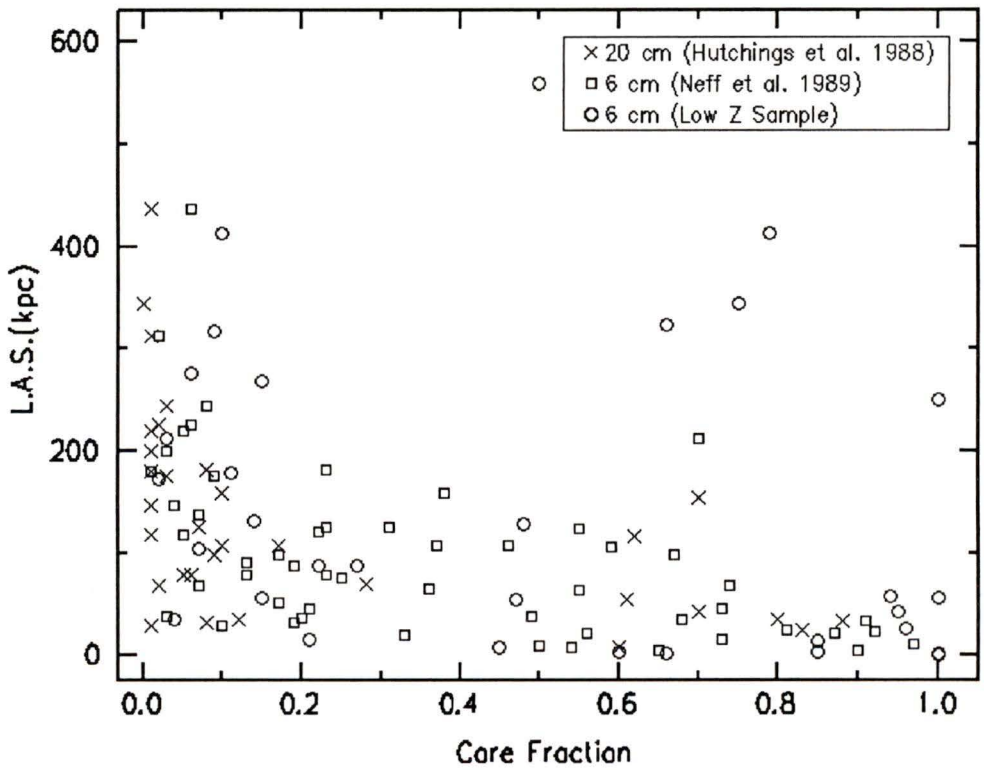

Figure 6.2: Size vs. Core Fraction Distribution (Combined Data)

If the size-core fraction relation is indeed due to orientation effects, we would also expect to find a correlation between the core fraction and the other two statistical orientation indicators discussed in Chapter 5, namely the bend angle and hotspot-distance ratio (Q).

Figures 6.3 and 6.4 , which include sources from Hutchings *et al.* (1988) and Neff *et al.* (1989) show no such correlation however, suggesting that the core fraction of a source is not a good statistical indicator of its lobe orientation. A better model than the simple beaming explanation is obviously needed.

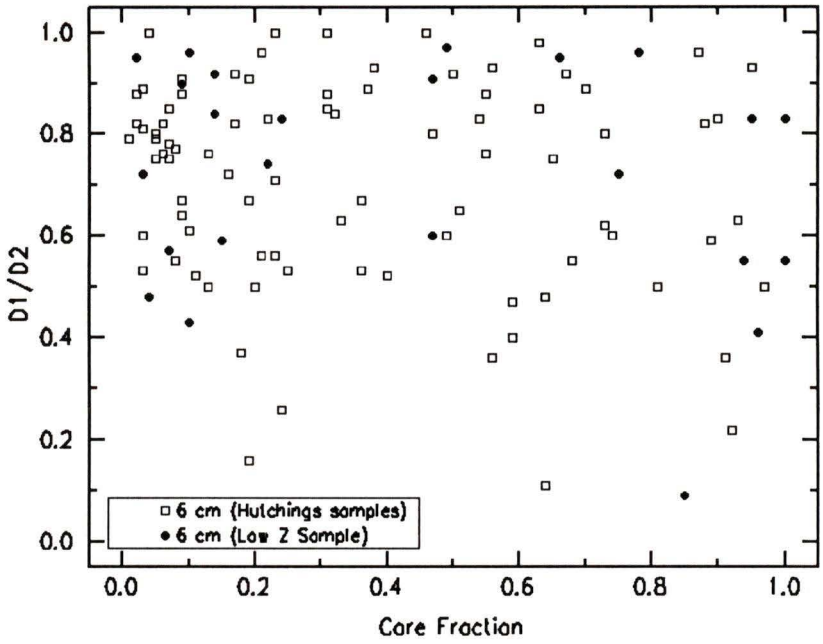

Figure 6.3: Hotspot Distance Ratio vs. Core Fraction (6 cm)

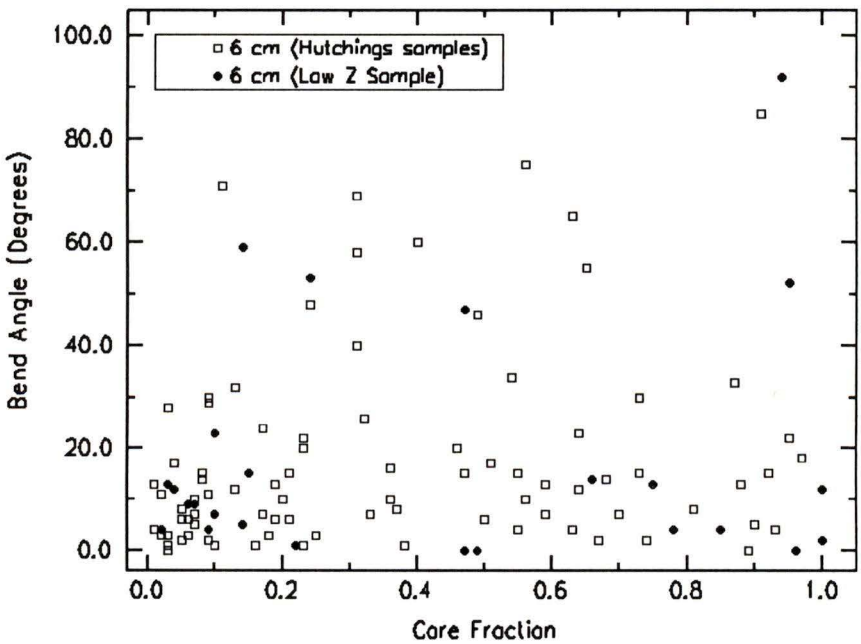

Figure 6.4: Bend Angle vs. Core Fraction (6 cm)

6.3.2. Evolutionary Interpretation

A somewhat different explanation for the distribution of Figure 6.2 can be found in an evolutionary scheme for radio quasars described by Hutchings, Price and Gower (1988). In their model, sources start out as core-dominated, and then develop increasingly larger radio lobes as the core fades. It would thus be the age, and not the orientation that would dictate the observed core fraction and apparent size of a source.

By assuming a simple exponential decay for the core, and a linear growth for the lobe size and power, it is possible to obtain a curve that fits the observational data quite well.

Letting the core luminosity *(C)* decay exponentially and the extended (lobe) luminosity *(E)* increase linearly with time as the source grows, we have

$$C \propto e^{-k_1 t} \tag{5.1}$$

$$E = k_2 t \tag{5.2}$$

The core fraction *(f)* can then be expressed as a function of time:

$$f = \frac{C}{C+E} \tag{5.3}$$

$$f = (1 + k_2 t e^{k_1 t})^{-1} \tag{5.4}$$

The rates of core decay and lobe growth are free parameters, and by choosing appropriate values of k_1 and k_2 one obtains curves that can be fit to the distribution in Figure 6.5. The curves in this figure use $k_1 = 0.018$, $k_2 = 0.005$ (Model 1) and $k_1 = 0.005$, $k_2 = 0.005$ (Model 2). The two models differ only in the rates of the core decay, suggesting that the scatter in the diagram might be due to different core decay rates.

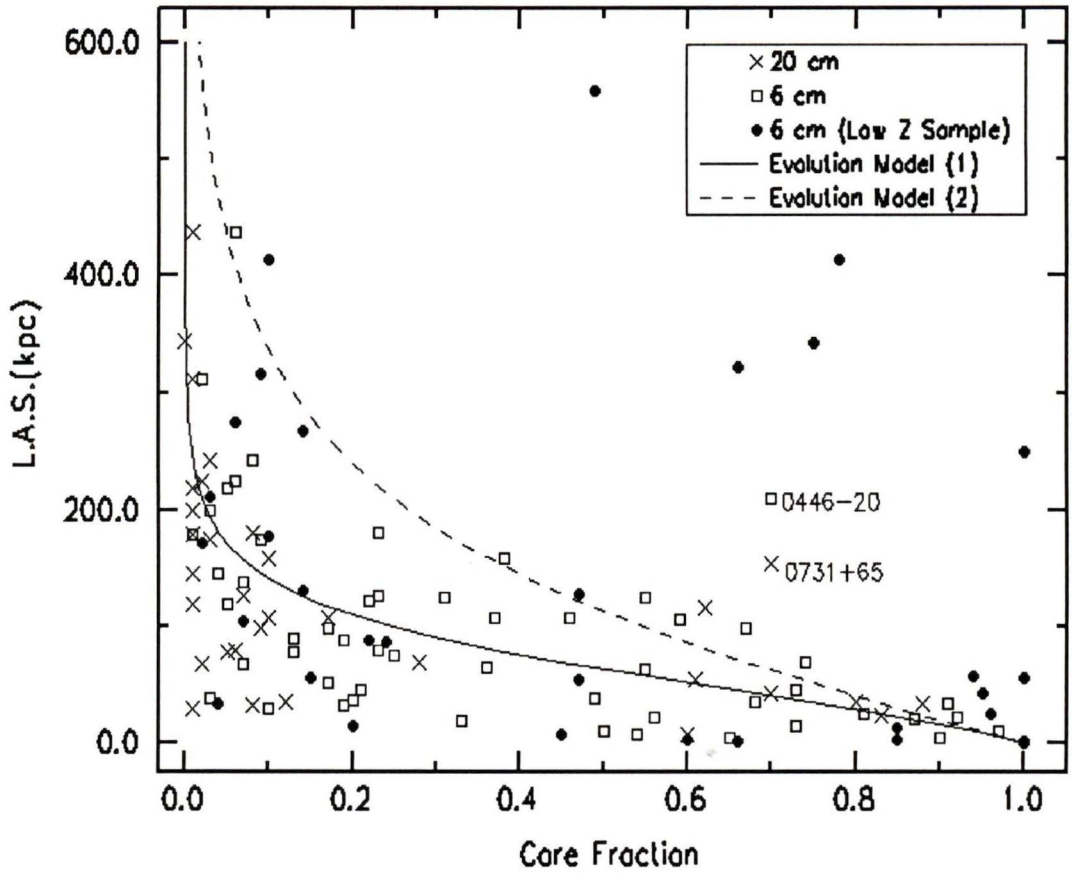

Figure 6.5: Evolutionary Models

6.4. Discussion

Although the beaming model correctly predicts the existence of a relation between size and core fraction, it cannot account for the lack of any correlation between the latter parameter and bend angle or hotspot-distance ratio. The evolutionary model is more consistent with the distributions shown in Figures 6.2, 6.3, and 6.4. The main conclusion that can be drawn is that the observed core fraction of a source is more likely to be related to its evolutionary stage and not its orientation.

There are undoubtedly a small percentage of sources, which by virtue of being pointed directly at us, have their core fractions increased by beaming effects. The majority of superluminal sources do indeed have high core fractions, as do the BL Lac objects. There are a few sources however, such as 3C 263, that do not obey this trend due to their anomalously weak cores. Furthermore, the existence of superluminal motion in extremely large quasars such as 1721+343 (Barthel, 1989) poses a problem for beaming supporters.

As the evidence for superluminal motion being commonplace in radio quasars continues to mount, the notion that superluminal sources are always pointed directly at us may have to be discarded. The quality of VLBI maps is still quite low, making it difficult to trace with confidence the motion of individual components on maps made at successive epochs. Some authors, including Pearson (1990) have proposed that we are not following individual blobs of matter but instead are merely tracing the brightness peaks in the jet. We therefore might be measuring a phase velocity, which could be much higher than the velocity of the moving components.

On the other hand, if one decides to accept the current model for superluminal motion some assumptions must be made. Firstly core-lobe misalignments must be postulated to explain sources such as 1721+343 and the other large, double-lobed superluminals, of which there are seven currently known (Impey, 1993). Secondly, the ubiquity of superluminal motion requires that all quasars lie near the line of sight, which is supported by the results of Chapter 5. The most serious challenge to this idea comes from the observation of superluminal motion in Seyfert and radio galaxies such as 3C 120 and 3C 111 (Preuss et

al. 1990, Walker et al. 1987). If more such sources were to be found in the near future it would have serious repercussions on the beaming theory.

In conclusion it does not appear the core fraction is a very good statistical indicator of either core or lobe orientation, as it can be affected by both source evolution and core-lobe misalignments. The observed size-core fraction relation can be adequately described by a simple evolution model in which the core fades as the lobe structure increases in size, without the need to invoke relativistic beaming.

Chapter Seven:

Correlations with Optical Properties

Several correlations between the optical and radio properties of the low-redshift sample were discussed in Gower and Hutchings (1984) (GH). At that time optical data were available for only 24 sources in the sample. Since then additional maps have been published, bringing the total up to 33. Many of the sources have been re-observed with the HR-Cam instrument (McClure 1992) at the Canada-France-Hawaii Telescope, which has consistently yielded images rivalling those of the Hubble Space Telescope in resolution.

7.1. Optical Nuclear Magnitude

GH reported a correlation between optical nuclear magnitude and radio-core luminosity that is re-confirmed in Figure 7.1. The linear correlation coefficient (ρ) of this plot is 0.27, which is significant at the 86% confidence level.

Part of the scatter is due to inaccuracies in subtracting the host-galaxy luminosity from the nucleus, and might also be due to source variability, since the radio and optical measurements were not taken simultaneously. The optical nuclear magnitude does not appear to correlate with any of the other radio properties of the sample, including the spectral index. GH found weak evidence that sources with inverted spectra are more luminous using 20-6 cm spectral indices for the sample. Figure 7.2 shows no such correlation with the 6-2 cm spectral index, which is generally more accurate due to the higher resolution of the maps.

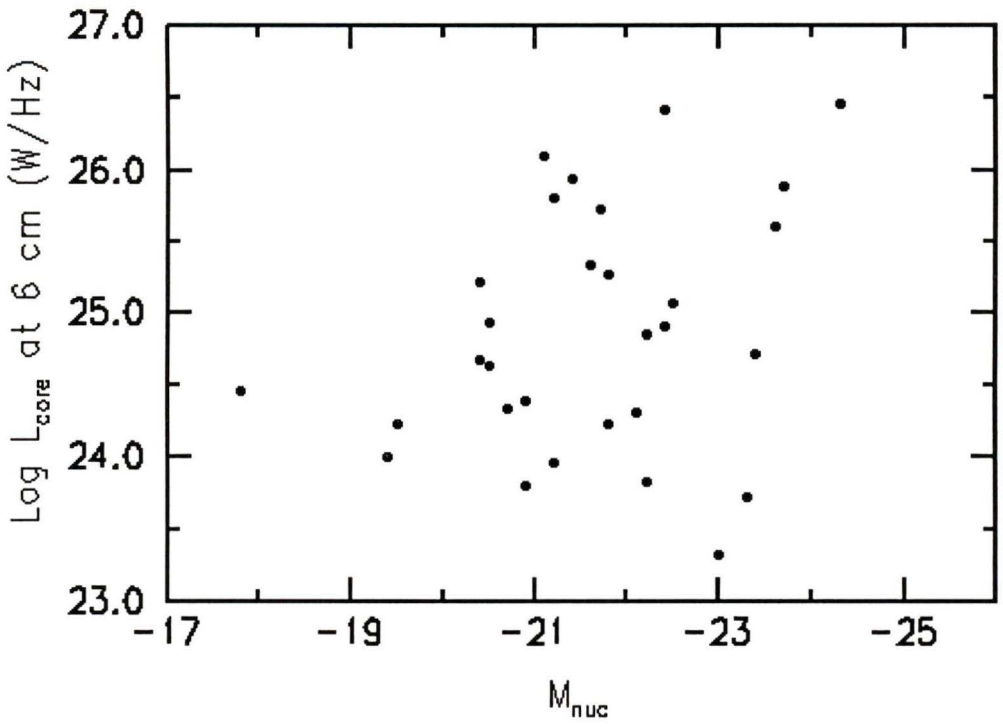

Figure 7.1: Radio Core Luminosity vs. Optical Nuclear Magnitude

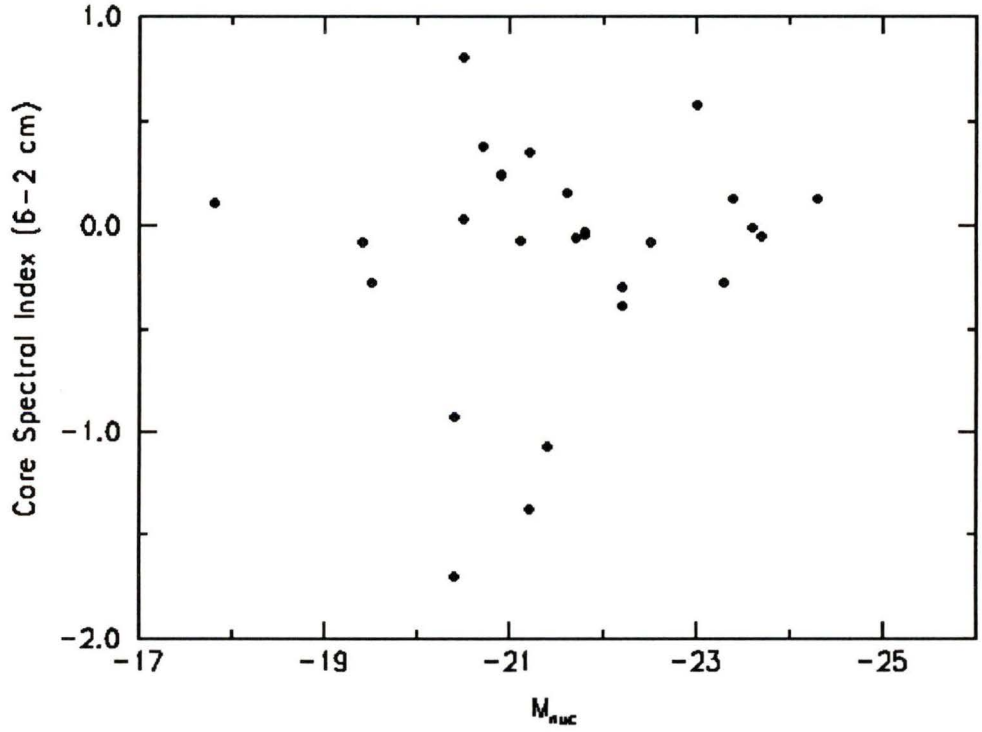

Figure 7.2: Core Spectral Index vs. Optical Nuclear Magnitude

7.2. Host Galaxy Properties

7.2.1. Radio Core Luminosity Correlation

Since it has only been a little over a decade since the first discoveries of optical nebulosities surrounding quasars, very little is known about the relation between the host galaxy and radio core properties. Imaging of the surrounding galaxies is extremely challenging due to the enormous luminosity of the nucleus, and host galaxy magnitudes are thus prone to large error (Hutchings and Neff, 1992). However, in spite of these uncertainties, there appears to be a correlation (ρ= 0.465, P= 99%) between the host galaxy magnitude M_{gal} and the radio core luminosity at 6 cm for the low-redshift sample (Figure 7.3).

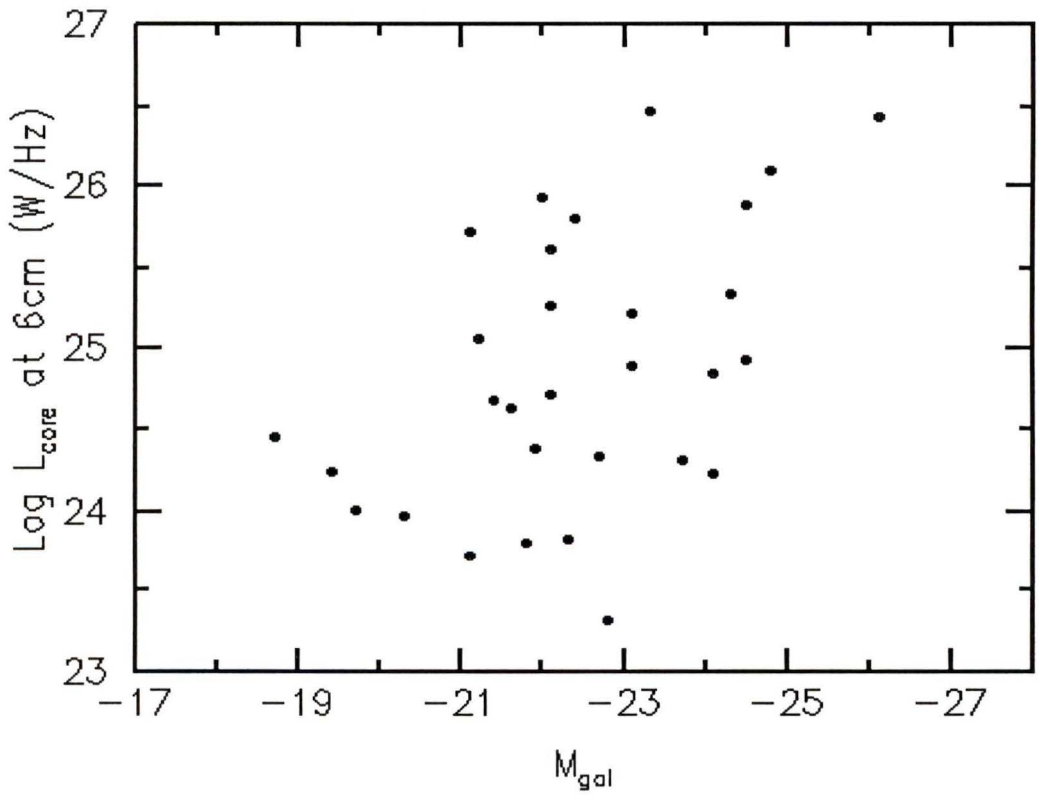

Figure 7.3: Radio Core Luminosity vs. Host Galaxy Magnitude

The result that radio power is greater in brighter galaxies was also found by Hutchings *et al.* (1984), and could be indicative of a recent merger event which has triggered activity in both the nuclear and host galaxy components. Indeed, Smith *et al.* (1986) find that radio-loud quasars have host galaxies that are typically a magnitude more luminous than radio-quiet ones. Several authors (Hutchings *et al.* 1984b, Smith *et al.* 1986, Heckman *et al.* 1986) have also found that a large fraction of quasar host galaxies shows signs of peculiar and distorted morphology, which may be the result of mergers.

In addition to fueling the nucleus, a tidal encounter might trigger a burst of star formation in the host galaxy. I find some evidence that the stronger radio cores reside in bluer host galaxies, which supports this suggestion (Figure 7.4). Hutchings (1987) has also

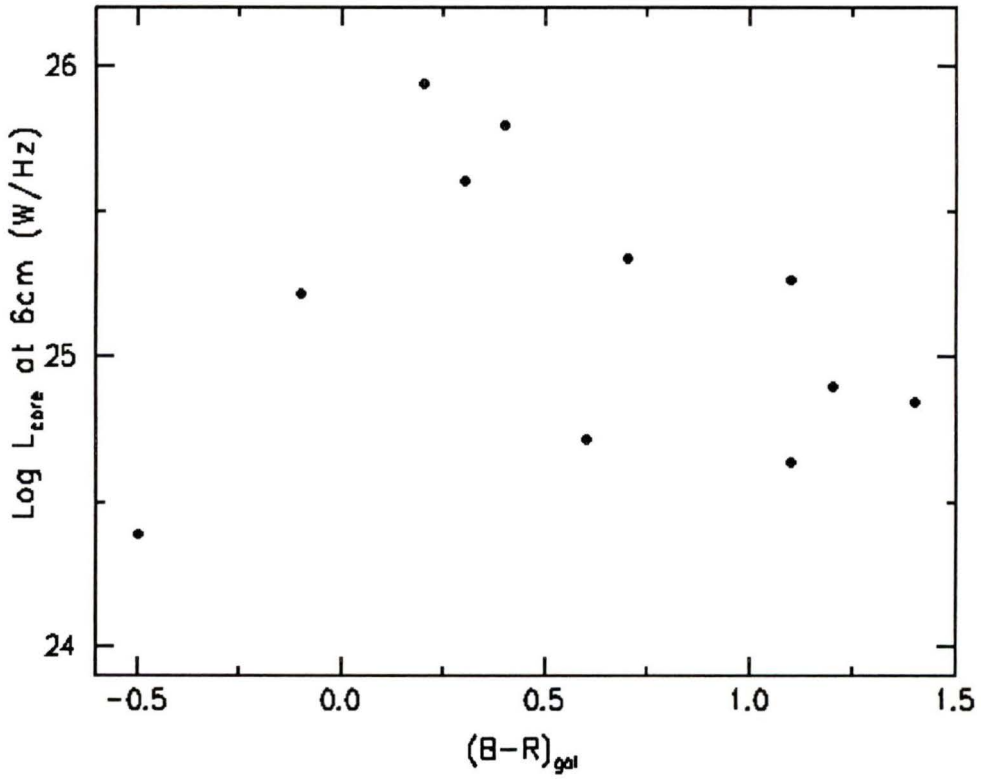

Figure 7.4: Radio Core Luminosity vs. Host Galaxy Color

shown that the host galaxies of quasars are significantly bluer than those of radio galaxies, which generally have very weak or undetectable radio cores.

7.3. Nuclear to Fuzz Luminosity Ratio

The ratio L_n/L_f of nuclear to host-galaxy luminosity has been investigated for several small samples of radio quasars by Hutchings *et al.* in a series of papers (Hutchings *et al.*, 1982, Hutchings 1987, Hutchings and Neff, 1990). They found that radio-loud quasars generally have larger values of L_n/L_f, most likely as a consequence of the core optical vs. radio luminosity relation discussed in §7.1. However, neither my data nor their samples showed any sign of a relation between L_n/L_f and core radio luminosity.

The use of the L_n/L_f statistic as a beaming indicator appears to be hampered by the same evolutionary effects that plague the radio core fraction (see Chapter 6). It does not appear to correlate with any of the radio properties of the low-redshift sample, including bend angle, with which Hutchings and Neff (1990) claimed to find a positive correlation.

However, it is interesting to note that two of the sources mentioned in §6.3.1 as having excessively high core fractions for their apparent size, 0742+318 and 1217+023, both have L_n/L_f values significantly higher than the median value of the sample. The overly bright core fluxes at both optical and radio wavelengths suggest that these sources may have beamed cores. Unfortunately there is no published value of L_n/L_f for the other discrepant source, 1721+343, so it is unclear if this source exhibits similar behaviour. If superluminal cores are indeed pointed at us, a study of their optical L_n/L_f values would prove to be extremely useful for testing the beaming hypothesis.

7.4. Host Galaxy Scale Length

Determinations of the radial intensity profiles of underlying QSO host galaxies have long been hindered by the observational difficulties already discussed. However, improvements in image quality and the use of CCD detectors over photographic plates enabled Hutchings (1987) to distinguish between host galaxies with standard ($L \propto r^{-1/4}$) brightness profiles from those with less-commonly-seen exponential ones, ($L \propto \exp(-r/r_s)$, where r_s is the scale length in kpc). He found that the scale lengths are larger in the host galaxies of quasars as compared to radio galaxies, with the largest quasars having the largest scale lengths. A plot of largest apparent size versus scale length for the low- redshift sample, which has 12 sources in common with the Hutchings (1987) sample, shows no apparent trend (Figure 7.5) The three quasars with the largest scale lengths all have radio structures less than 200 kpc, which is difficult to reconcile with Hutchings' hypothesis.

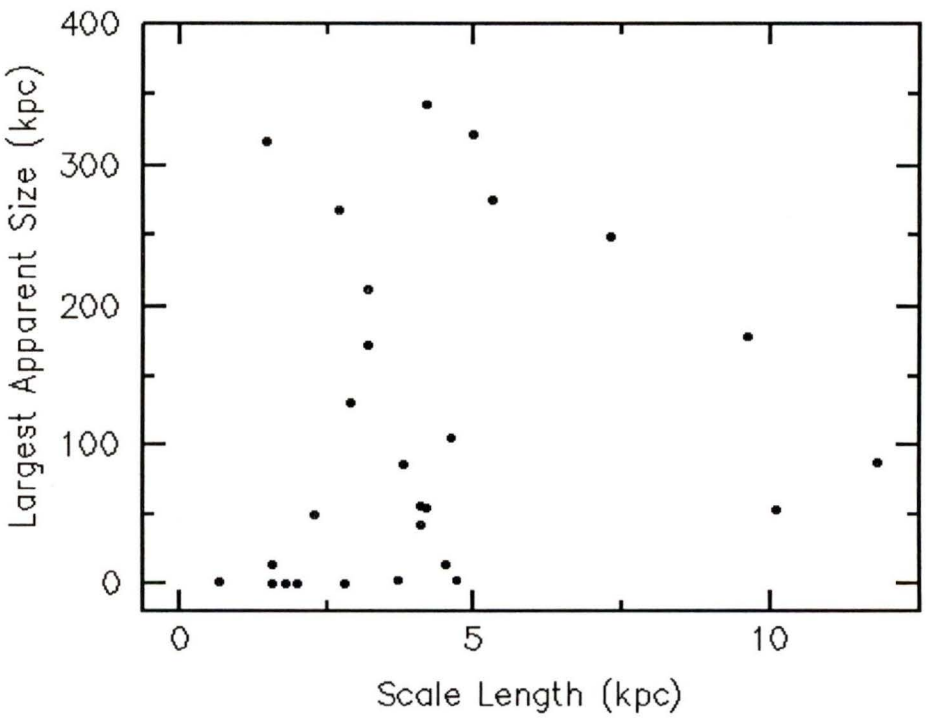

Figure 7.5: Radio Structure Size vs. Host Galaxy Scale Length

7.5. Summary

The comparisons of the optical and radio properties of the low-redshift sample were somewhat disappointing, as no new correlations were found. Indeed, many of the possible correlations proposed in the literature were not seen in my data set. The radio core luminosity and nuclear / host galaxy relations suggest that there is a connection between the host galaxies of quasars and their radio properties, but optical data for larger samples of radio galaxies and quasars will have to be obtained before we can gain a better insight into this area. As improvements are made in the resolution of ground-based images using adaptive optics systems, it will be possible to extend studies to higher redshifts, while at the same time greatly reducing errors in the measured optical quantities. In particular, high quality L_n/L_f measurements for large samples of quasars may help determine whether this statistic can be used as a reliable beaming indicator.

Chapter Eight:

Conclusion

In this thesis I have looked at many aspects of the radio and optical properties of a sample of 40 low-redshift radio quasars.

By using the published 6 cm data of Gower and Hutchings (1984), I was able to obtain two-epoch core variability estimates for the sample sources. These estimates, although limited by having only two flux measurements, nevertheless provided important insight on the nature of variability of weak cores embedded in large scale structure. In all, 9 out of 23 triple and 3 out of 4 core-dominated sources had variable cores, suggesting that variability is common among both morphological classes.

As beaming models predict that sources lying near the line of sight should appear more variable, I looked for correlations between variability, core fraction, and radio size. For the variable and non-variable sources, there were no appreciable differences in either the core fraction or radio size distributions. I also found no difference in the core luminosity distributions of the two groups.

In contrast to claims made by other authors that flat- and inverted-spectrum sources are generally more variable than steep ones, I found no difference in the spectral index distributions of the non-variable and variable sources in my sample. However, this appears to be due to the fact that the low-redshift sample includes many weak-core sources that have been omitted from previous variability studies. These weak cores, nearly all of which are found in triple sources, have the interesting property that the variable ones nearly all have steep spectra.

In Chapter 5 I showed a strong anticorrelation between radio structure size and apparent bend angle for my sample which can be explained entirely in terms of projection effects. My numerical modelling experiments led to the finding that the radio size - bend angle distribution, as well as the radio size - Q distribution, can be reproduced by a set of equal-lobe-length, orientation-biased objects. This bias involves excluding those objects

that lie within a certain angle to the plane of the sky from the model. This is consistent with the unified model of Barthel (1987) in which quasars are objects that lie near the line of sight.

By excluding the objects in the plane of the sky, the orientation bias was also responsible for producing a deficit of sources having equal core-hotspot distances. This has important implications for alternating ejection studies which have been based largely on this observed deficit.

I also found an anticorrelation between radio size and core fraction, which has been interpreted by past authors as evidence for beaming of the core component flux. However, I found no evidence of any correlation between the core fraction and the bend angle or Q parameters, which suggests that the observed anticorrelation is not due to beaming or projection effects. A more satisfactory explanation of the data was found using the evolutionary scheme of Hutchings, Price and Gower (1988), in which radio sources start out as core dominated, and then grow lobe structure as the core fades.

There were very few well defined correlations between the and radio properties of the sample, and the optical properties of the host galaxy; the strongest correlations were those between the core radio luminosity and both the optical host galaxy and nuclear magnitudes. A weaker correlation was found between core radio luminosity and host galaxy color. These observations are consistent with current theories regarding the triggering of quasar activity by merger or tidal interaction events. No correlations between the optical nuclear to host galaxy luminosity ratio (L_n/L_f) and other radio properties were found, but it is possible that some may have been masked by the small number of sources involved and/or observational errors. Until larger data sets are obtained it will remain unclear as to what degree this statistic can be relied upon as a beaming indicator.

In summary, the findings of this thesis are consistent with the Barthel (1989) scenario in which radio quasars are objects oriented towards the line of sight, with the viewing angle towards an obscuring dust torus being responsible for their optical classification. This model provides a natural explanation for the ubiquity of variability and superluminal

motion in the different source morphologies, and is consistent with the results of my numerical modelling experiments of quasar orientation.

Until such time as the effects of quasar orientation, beaming, and evolution can be fully disentangled, the inner workings of extragalactic radio sources will remain a mystery. It will no doubt be some time before our knowledge in this area approaches that of other branches of astronomy such as stellar astrophysics. However, considering the enormously large distances involved, it is remarkable how much insight has already been gained into these fascinating objects.

References

Aller, M. 1991, in *Variability of Active Galactic Nuclei*, eds. H. Miller and P. Wiita (Cambridge: Cambridge University Press).

Altschuler, D. 1983, *Astronomical Journal,* **88**, 16.

Altschuler, D. 1989, *Fundamentals of Cosmic Physics*, **14**, 37.

Andrew, B., MacLeod, J., Harvey, G., Medd W., 1978, *Astronomical Journal,* **83**, 863.

Antonucci, R. and Ulvestad, J. 1984, *Nature,* **308**, 617.

Antonucci, R. and Ulvestad, J. 1985, *Astrophysical Journal,* **294**, 158.

Barthel, P. 1987, in *Superluminal Radio Sources*, eds. J. Zensus and T. Pearson (Cambridge: Cambridge University Press), p. 148.

Barthel, P. 1989, *Astrophysical Journal,* **336**, 606.

Barthel, P., Miley, G., Schilizzi, R., Preuss, E. 1985, *Astronomy and Astrophysics,* **151**, 131.

Barthel, P., Pearson, T., Readhead, A., Canzian, B. 1986, *Astrophysical Journal Letters,* **310**, L7.

Barthel, P. and Miley G. 1988, *Nature,* **333**, 319.

Blandford, R. and Rees, M. 1974, *Monthly Notices of the Royal Astronomical Society,* **169**, 395.

Bridle, A. 1990, in *Parsec Scale Radio Jets*, eds. J. Zensus and T. Pearson, (Cambridge: Cambridge University Press), p. 187.

Browne, I. 1983, *Monthly Notices of the Royal Astronomical Society,* **204**, 238.

Browne, I. 1987, in *Superluminal Radio Sources*, eds. J. Zensus and T. Pearson, (Cambridge: Cambridge University Press), p. 129.

Cohen, M. 1989, in *BL Lac Objects*, eds. L. Maraschi, T. Maccacaro and M. Ulrich (Berlin: Springer-Verlag), p. 13.

Conway, J. and Murphy, D. 1992, Preprint.

Cotton, W., Wittels, J., Shapiro, I., Marcaide, J., Owen, F., Spangler, S., Rius, A., Angulo, C., Clark, T., Knight, C. 1980, *Astrophysical Journal Letters,* **238**, L123.

Cruise, A. and Dodds, P. 1985, *Monthly Notices of the Royal Astronomical Society,* **215**, 417.

Dent, W. 1966, *Astrophysical Journal,* **144**, 843.

Duric, N., Gregory, P., and Tsutsumi, T. 1989, *Nature,* **337**, 143.

Eckart, A., Hummel, C., Witzel, A. 1989, *Monthly Notices of the Royal Astronomical Society,* **239**, 381.

Edelson, R. 1987, *Astronomical Journal,* **94**, 1150.

Ensman, L. and Ulvestad, J. 1984, *Astronomical Journal,* **89**, 1275.

Epstein, E., Fogarty, W., Mottmann, J., Schneider, E. 1982, *Astronomical Journal,* **87**, 449.

Fasano, G. and Franceschini, A. 1987, *Monthly Notices of the Royal Astronomical Society,* **225**, 155.

Fanti, C., Fanti, R., Ficarra, A., Gregorini, L., Mantovani, F., and Padrielli, L. 1983, *Astronomy and Astrophysics,* **118**, 171.

Fanti, C. and Fanti, R. 1987, in *Superluminal Radio Sources*, eds. J. Zensus and T. Pearson (Cambridge: Cambridge University Press), p. 174.

Fanti C., Fanti, R., Schilizzi, R., Spencer, R., Nan Rendong, Parma, P., van Breugel, W., Venturi, T. 1990, in *Parsec Scale Radio Jets*, eds. J. Zensus and T. Pearson (Cambridge: Cambridge University Press), p. 146.

Feretti, L., Comoretto, G., Giovannini, G., Venturi, T., Wehrle, A. 1992, in *Poster papers from the Space Telescope Science Institute Symposium on Astrophysical Jets*, p. 11.

Ford, H., Jaffe, W., Ferrarese, L., van den Bosch, F., O'Connell, R. 1993, *Space Telescope Science Institute Newsletter*, **10**, 1.

Garrington, S., Leahy, P., Conway, R. and Laing, R. 1988, *Nature,* **331**, 149.

Garrington, S., Conway, R. and Leahy, J. 1991, *Monthly Notices of the Royal Astronomical Society,* **250**, 171.

Ghosh, T. and Gopal-Krishna 1990, *Astronomy and Astrophysics,* **230**, 297.

Gower, A., Gregory, P., Hutchings, J., and Unruh, W. 1982, *Astrophysical Journal,* **262**, 478.

Gower, A. and Hutchings, J. 1984, *Astrophysical Journal,* **89**, 1658.

Gower, A. and Hutchings, J. 1984b, *Publications of the Astronomical Society of the Pacific,* **96**, 19.

Gregorini, L., Ficarra, L., and Padrielli, L. 1986, *Astronomy and Astrophysics,* **168**, 25.

Harris, D., Dewdney, P., Costain, C., Butcher, H., Willis, A. 1983, *Astrophysical Journal,* **270**, 39.

Heeschen, D. and Rickett, B. 1987, *Astronomical Journal,* **93**, 589.

Heckman, T., Smith, E., Baum, S., van Breugel, W., Miley, G., Illingworth, G., Bothun, G., Balick, B. 1986, *Astrophysical Journal,* **311**, 526.

Hewitt, A. and Burbidge, G. 1989, *Astrophysical Journal Supplement Series,* **69**, 1.

Hintzen, P. and Owen, F. 1981, *Astronomical Journal,* **86**, 1577.

Hintzen, P., Ulvestad, J. and Owen, F. 1983, *Astronomical Journal,* **88**, 709.

Hogbom, J. 1974, *Astrophysical Journal Supplement Series,* **15**, 417.

Hooimeyer J., Schilizzi, R., Miley, G., Barthel, P. 1992, *Astronomy and Astrophysics,* **261**, 1.

Hough, D. and Readhead, A. 1987, in *Superluminal Radio Sources*, eds. J. Zensus and T. Pearson (Cambridge: Cambridge University Press), p. 114.

Hough, D. and Readhead, A. 1989, *Astronomical Journal,* **98**, 1208.

Hughes, P., Aller, H., and Aller, M. 1985, *Astrophysical Journal,* **298**, 301.

Hughes, P., Aller, H., and Aller, M. 1989, *Astrophysical Journal,* **341**, 54.

Hutchings, J. 1987, *Astrophysical Journal,* **320**, 122.

Hutchings, J., Crampton, D., Campbell, B., Pritchet, C. 1981, *Astrophysical Journal,* **247**, 743.

Hutchings, J., Campbell, B., Crampton, D., Gower, A., and Morris, S. 1982, *Astrophysical Journal,* **262**, 48.

Hutchings, J., Crampton, D., Campbell, B., Duncan, D., and Glendenning, B. 1984a, *Astrophysical Journal Supplement Series,* **55**, 319.

Hutchings, J., Crampton, D., and Campbell, B. 1984b, *Astrophysical Journal Supplement Series,* **280**, 41.

Hutchings, J., Johnson, I., Pyke, R. 1988, *Astrophysical Journal Supplement Series,* **66**, 361.

Hutchings, J., Price, R., Gower, A. 1988, *Astrophysical Journal,* **329**, 122.

Hutchings, J. and Neff, S. 1990, *Astronomical Journal,* **99**, 1715.

Hutchings, J. and Neff, S. 1992, *Astronomical Journal,* **104**, 1.

Hutchings, J., Neff, S., and Gower, A., 1992, *Publications of the Astronomical Society of the Pacific,* **104**, 66.

Impey, C. 1993, Private Communication.

Jagers, W., van Breugel, W., Miley, G., Schilizzi, R., Conway, R. 1982, *Astronomy and Astrophysics,* **105**, 278.

Kapahi, V. 1990, in *Parsec Scale Radio Jets*, eds. J. Zensus and T. Pearson (Cambridge: Cambridge University Press), p. 304.

Kapahi, V. and Saikia, D. 1982, *Journal of Astrophysics and Astronomy,* **3**, 465.

Kellermann, K. and Owen, F. 1988, in *Galactic and Extragalactic Radio Astronomy*, eds. G. Verschuur and K. Kellermann (Berlin: Springer-Verlag), p. 563.

Lawrence, C., Readhead, A., Pearson, T., Unwin, S. 1987, in *Superluminal Radio Sources*, eds. J. Zensus and T. Pearson (Cambridge: Cambridge University Press), p. 260.

Lawrence, C. 1990, in *Parsec Scale Radio Jets*, eds. J. Zensus and T. Pearson (Cambridge: Cambridge University Press), p. 280.

Macklin, J. 1981, *Monthly Notices of the Royal Astronomical Society,* **196**, 967.

Marscher, A. and Gear, W. 1985, *Astrophysical Journal,* **298**, 114.

Marscher, A. 1987, in *Superluminal Radio Sources*, eds. J. Zensus and T. Pearson (Cambridge: Cambridge University Press), p. 280.

McClure, R. 1992, in *Proceedings of the Third Canada-France-Hawaii Telescope Users' Meeting*, ed. R. Arsenault (Kamuela: Canada-France-Hawaii Telescope Corporation), p. 42.

Miley, G. and Hartsuijker, A. 1978, *Astronomy and Astrophysics Supplement Series,* **34**, 129.

Mutel, R. 1990, in *Parsec Scale Radio Jets*, eds. Zensus, J. and Pearson, T. (Cambridge: Cambridge University Press), p. 98.

Neff, S. 1982a, Ph.D. Thesis, University of Virginia.

Neff, S. 1982b, in I.A.U. Symposium No. 97, *Extragalactic Radio Sources*, eds. D. Heeschen and C. Wade (Dordrecht: Reidel), p. 137.

Neff, S., Hutchings, J., Gower, A. 1989, *Astronomical Journal,* **97**, 1291.

Neff, S. and Hutchings, J. 1990, *Astronomical Journal,* **100**, 1441.

Orr, M. and Browne, I. 1982, *Monthly Notices of the Royal Astronomical Society,* **200**, 1067.

Padovani, P. 1992, *Monthly Notices of the Royal Astronomical Society,* **257**, 404.

Padovani, P. and Urry, C. 1992, *Astrophysical Journal,* **387**, 449.

Pauliny-Toth, I. and Kellermann, K. 1966, *Astrophysical Journal,* **146**, 634.

Peacock, J. 1983, *Monthly Notices of the Royal Astronomical Society,* **202**, 615.

Peacock, J. 1987, in *Astrophysical Jets and their Engines* ed. W. Kundt (Dordrecht: Reidel), p. 185.

Pearson, T. 1990, in *Parsec Scale Radio Jets*, eds. J. Zensus and T. Pearson (Cambridge: Cambridge University Press), p. 1.

Pearson, T., Readhead, A., and Barthel, P. 1987, in *Superluminal Radio Sources*, eds. J. Zensus and T. Pearson (Cambridge: Cambridge University Press), p. 94.

Pearson, T. and Zensus, J. 1987, in *Superluminal Radio Sources*, eds. J. Zensus and T. Pearson (Cambridge: Cambridge University Press), p. 1.

Pearson T. and Readhead A. 1988, *Astrophysical Journal,* **328**, 114.

Perley, R. 1992, *Very Large Array Observational Summary*, National Radio Astronomy Observatory Circular.

Perley, R., Schwab, F., and Bridle, A. 1989, *Synthesis Imaging in Radio Astronomy* (San Francisco: Astronomical Society of the Pacific Conference Series Volume 6).

Preuss, E., Alef, W., Shengyin, W., Yuhai, Q., Zhihan, Q., Kellermann, K., Matveenko, L., Gotz, M. 1990 in *Parsec Scale Radio Jets*, eds. J. Zensus and T. Pearson (Cambridge: Cambridge University Press), p. 120

Rees, M. 1967, *Nature,* **135**, 345.

Rees, M. 1971, *Nature,* **229**, 312.

Rees, M. 1984, *Annual Review of Astronomy and Astrophysics,* **22**, 471.

Riley, J. and Pooley, G. 1978, *Monthly Notices of the Royal Astronomical Society,* **184**, 769.

Rys, S. and Machalski, J. 1990, *Astronomy and Astrophysics,* **236**, 15.

Saikia, D., Singal, A., Wiita, P. 1991, in *Variability of Active Galactic Nuclei*, eds. H. Miller and P. Wiita (Cambridge: Cambridge University Press).

Scheuer, P. 1987, in *Superluminal Radio Sources*, eds. J. Zensus and T. Pearson (Cambridge: Cambridge University Press), p. 104.

Scheuer, P. and Readhead A. 1979, *Nature,* **277**, 182.

Schilizzi, R. and De Bruyn, A. 1983, *Nature,* **303**, 26.

Smith, P., Heckman, T., Bothun, G., Romanshin, W., Balick, B. 1986, *Astrophysical Journal,* **306**, 64.

Stocke, J., Burns, J., Christiansen, W. 1985, *Astrophysical Journal,* **299**, 799.

Teerikorpi, P. 1984, *Astronomy and Astrophysics,* **132**, 179.

Thompson, A., Moran, J., and Swenson, G. 1986, *Interferometry and Synthesis in Radio Astronomy*, (New York: Wiley).

Turland, B. 1975, *Monthly Notices of the Royal Astronomical Society,* **170**, 281.

Unwin, S. 1985, *Astrophysical Journal,* **289**, 109.

Unwin, S., Cohen, M., Biretta, J., Hodges, M., Zensus, J. 1989, *Astrophysical Journal,* **340**, 117.

Urry, C.M. 1993, Preprint.

Walker, R., Benson, J., and Unwin, S. 1987, in *Superluminal Radio Sources*, eds. J. Zensus and T. Pearson (Cambridge: Cambridge University Press), p. 48.

Wardle, J. and Potash, R. 1984, in *Physics of Energy Transport in Extragalactic Radio Sources*, eds. A. Bridle and J. Eilek (Green Bank: National Radio Astronomy Observatory), p. 128.

Witzel, A., Schalinski, C., Johnston, K., Biermann, P., Krichbaum, T., Hummel, C., Eckart, A. 1988, *Astronomy and Astrophysics,* **206**, 245.

Wyckoff, S., Wehinger, P., and Gehren, T. 1981, *Astrophysical Journal,* **247**, 750.

Zensus, J. and Porcas, R. 1987, in *Superluminal Radio Sources*, eds. J. Zensus and T. Pearson (Cambridge: Cambridge University Press), p. 126.

Appendix A:

Source Maps

A.1. Maps

In this appendix I present contour maps made from the second-epoch VLA data taken of the low-redshift sample. A list of the contour intervals as a percentage of peak can be found in Table A.1. The optical identification positions from Hewitt and Burbidge (1989) are marked with a cross.

Since the primary beam of the VLA in the A configuration at 2 and 6 cm was not large enough to map the large scale structure of many sources, I have included maps from the literature for reference purposes. The appropriate references can be found below each map. I have also included optical maps of the sample, both published and un-published, as provided to me by John Hutchings.

Where possible, I have tried to reproduce the optical and radio maps with the same scale, but large differences in size between the radio and optical structures made this unfeasible for many sources. I have thus included scale bars where necessary.

A.2. Notes on Individual Sources

When presenting data on a sample of radio quasars, it is somewhat traditional to include a section describing interesting details in the morphology of the individual sources. As this has been done already for the low-redshift sample by Gower and Hutchings (1984) (GH84), in this section I will concentrate only on those sources for which new information was gained from the 2 cm maps.

Studies of samples made at short observing wavelengths with the VLA are quite rare in the literature, due to the smaller field of view and lower sensitivity to extended structure. Furthermore, radio lobes generally emit very little luminosity at 2 cm due to their steep spectral indices. These drawbacks are partially offset however by the large gain in resolution achieved at 2 cm (see Chapter 2). This allowed structure to be seen in the lobes and the core components that was unresolved at 6 and 20 cm wavelengths.

0041+119

The morphology of this source is interesting as the intrinsic curvature of the southern extended structure seen in the 20 cm map of GH changes sign with distance from the core. GH suggested that this may be due to either effects in the inter-galactic medium, or precession of the core. The 2 cm map reveals a distinctive 'horseshoe' structure in the northern lobe which is perhaps tracing the end of the jet as it precesses.

0137+012

This source has been discussed in detail by Gower and Hutchings (1984b), where they used a precessing jet model to reproduce the complex structure of the northern lobe. At 2 cm, I find evidence of a horseshoe structure very similar to that of 0041+119, suggesting that this may be a diagnostic feature of precession.

0100+108

There has been considerable confusion over the identification of the optical counterpart to this source. Two optical objects in the field both contain emission lines, but are located several arcseconds to the northeast of the radio structure (GH84, Hintzen *et al.*, 1983). The radio structure is unusual in that deep imaging done at 3.5 cm with the VLA has failed to reveal a core component between the radio lobes (N. Jackson, private communication). Both lobes are also present on my 2 cm map, implying that they have similar spectral indices. Without verification of the associated optical component, it is difficult to classify this object as a radio quasar or galaxy, and without a redshift, its intrinsic luminosity cannot be measured.

1020-103

The small angular size of this object (~2") makes it ideal for 2 cm observations, and my map reveals several interesting features not seen at longer wavelengths. The northern lobe appears somewhat curved, while there is no counter lobe present on the opposite side of the core. Instead, there appears to be a slight core extension to the southeast. This extension fails to show up on the 1.3 cm map, which is either due to it having a steep spectral index, or being below the noise level. A steep spectral index would be expected if we are seeing evidence of a new extended component in this source. At present it is unclear whether the absence of a counter-lobe in core-lobe sources is a result of beaming or an alternating-ejection phenomenon. Higher resolution VLBI images would allow one to look for signs that this extension is in fact a new jet.

2247+140

This source has no lobe structure, but contains an extension near the core similar to that of 1020-103. The 1.3 cm map shows that the structure changes curvature significantly as it nears the core. Such changes in curvature are predicted by the helical jet models of Conway and Murphy (1992), in which the small scale jets propagate along helical paths as

a result of precession of the core. As these authors make detailed predictions of the morphology of these sources, this source would also be a good candidate for VLBI study.

2328+167

Gower and Hutchings (1984) were unable to determine which component was the core for this source from their 6 cm data, but it is evident from the 2 cm map that the southern component is resolved into a curved structure similar to that of 2247+140. The strong curvature close to the core is strongly suggestive of a helical jet flow.

2355-082

The improvement in resolution obtained with the 2 cm data has also revealed a small scale, curved structure in this source. The reoccurrence of this similar morphology in several of the sample objects might be indicating that this is a common feature of compact radio quasars that has been missed due to a lack of resolution in previous surveys.

Table A.1: Map Characteristics

Source	λ (cm)	Peak (mJy)	Contours as a percentage of peak											
0007+106	6	554	-0.3,	0.3,	0.6,	3,	10,	30,	60,	90				
	2	1421	-0.2,	0.2,	1,	3,	10,	30,	60,	90				
	1.3	2108	-1,	1,	5,	10,	20,	40,	60,	80				
0017+257	20	223	-0.2,	0.2,	0.5,	1,	2,	5,	10,	20,	30,	40,	50,	70, 90
	6	254	-0.5,	0.5,	1,	2,	5,	10,	20,	40,	80			
	2	354	-0.25,	0.25,	0.4,	0.6,	1,	3,	10,	20,	40,	60,	80	
0041+119	6	43	-2.5,	2.5,	4,	6,	8,	15,	20,	40,	80			
	2	17	-7,	7,	10,	12,	15,	20,	30					
0100+108	2	5	-30,	30,	40,	50,	60,	70,	80,	90				
	6	107	-2,	2,	5,	10,	20,	30,	40,	50,	70,	90		
	20	48	-1,	1,	2,	5,	10,	20,	30,	40,	50,	70,	90	
0137+012	6	170	-1,	1,	2,	3,	5,	10,	20,	30,	50,	70		
	2	98	-2,	2,	3,	4,	5,	6,	15,	30,	60,	90		
0241+622	6	2.4	-0.5,	0.5,	1,	2,	5,	10,	20,	30,	50,	70,	90	
	2	1.8	-1,	1,	5,	25,	60							
	1.3	631	-4,	4,	10,	30,	60,	90						
0736+017	20	2166	-0.1,	0.1,	0.14,	0.2,	0.28,	0.4,	0.57,	...				
	6	1881	-0.08,	0.08,	1,	5,	15,	40,	70					
	2	2768	-0.1,	0.1,	1,	5,	15,	40,	70					
0742+318	20	113	-6,	6,	8,	10,	13,	17,	22,	40,	50,	70,	90	

Table A.1: Map Characteristics

Source	λ (cm)	Peak (mJy)	Contours as a percentage of peak
	6	655	-0.15, 0.15, 2, 20, 50, 80
	2	604	-0.2, 0.2, 3, 20, 70
0829+046	20	639	-0.2, 0.2, 0.28, 0.4, 0.57, 0.8, 1.13, ...
	6	1062	-0.15, 0.15, 1, 5, 25, 50, 80
	2	1586	-0.15, 0.15, 3, 25, 50, 80
0846+100	20	15	-2, 2, 5, 10, 20, 30, 40, 50, 70, 90
	6	6.3	-18, 18, 35, 60, 90
	2	6.5	-15, 15, 25, 50, 85
0952+097	6	14.3	-3, 3, 5, 7, 10, 25, 50, 75, 90
	2	6.3	-40, 40, 60, 80, 90
1004+130	20	244	-1, 1, 2, 5, 10, 20, 30, 40, 50, 70, 90
	6	30.2	-1.5, 1.5, 10, 30, 60, 90
	2	30.4	-7, 7, 25, 50, 80
1020-103	2	1.3	-0.5, 0.5, 0.7, 1, 1.5, 5, 10, 30, 50, 70, 90
	1.3	96	-60, 60, 75, 85, 95
1028+313	20	89	-1, 1, 2, 5, 10, 20, 30, 40, 50, 70, 90
	6	79	-0.5, 0.5, 0.75, 1, 2, 5, 10, 30, 60, 90
	2	110	-0.6, 0.6, 1, 5, 25, 70
1203+011	6	147	-0.4, 0.4, 1, 5, 20, 50, 80
	2	110	-1, 1, 5, 20, 50, 80
1217+023	20	53	-7, -5, 5, 7, 9, 11, 13, 18, 25, 35, 50, 70, 90

Table A.1: Map Characteristics

Source	λ (cm)	Peak (mJy)	Contours as a percentage of peak
	6	328	-0.5, 0.5, 3, 10, 30, 60, 90
	2	293	-0.7, 0.7, 5, 25, 50, 75
1223+252	6	10.4	-15, 15, 20, 30, 40, 60, 80
	2	5.2	-40, 40, 70, 95
1243-072	20	845	-0.1, 0.1, 0.2, 0.5, 1, 2, 5, 10, 20, 30, 40, 50, 70, 90
	6	867	-0.08, 0.08, 1, 5, 15, 40, 80
	2	976	-0.15, 0.15, 1.5, 10, 30, 60, 90
1302-102	6	982	-0.1, 0.1, 0.2, 5, 30, 80
	2	9.3	-0.2, 0.2, 5, 40, 90
1525+227	6	35	-1.5, 1.5, 5, 15, 50, 85
	2	60	-4, 4, 8, 20, 50, 80
1635+119	20	38	-0.5, 0.5, 1, 2, 5, 10, 20, 30, 50, 70
	6	37	-3, 3, 10, 30, 60, 90
	2	7.2	-35, 35, 50, 70, 90
1721+343	20		(Not Available)
	6	385	-3, 3, 7, 15, 30, 60, 90
	2	213	-2, 2, 7, 15, 30, 60, 90
1725+044	6	630	-0.15, 0.15, 0.25, 4, 25, 75
	2	595	-0.25, 0.25, 1, 10, 50, 85
1739+184	20	77	-2, 2, 5, 10, 20, 30, 40, 50, 70, 90
	6	33	-2.5, 2.5, 10, 30, 60, 90

Table A.1: Map Characteristics

Source	λ (cm)	Peak (mJy)	Contours as a percentage of peak
	2	11.3	-25, 25, 50, 75, 90
2135-147	20	58	-2, 2, 5, 10, 20, 30, 40, 50, 70, 90
	6	136	-3, 3, 20, 50, 80
	cm	151	-3, 3, 20, 50, 80
2141+175	6	907	-0.3, 0.3, 2, 10, 50, 90
	2	902	-0.5, 0.5, 2, 10
2201+315	20	1299	-.1, .1, .2, .5, 1, 2, 5, 10, 20, 30, 40, 50, 70, 90
	6	3623	-0.3, 0.3, 1, 5, 20, 50, 80
	2	4244	-0.2, 0.2, 1, 5, 20, 50, 80
2217+087N	6	25.5	-7.5, 7.5, 15, 30, 60, 90
	2	28.7	-7, 7, 30, 60, 90
2217+087S	20	7.5	-13, 13, 27, 40, 53, 67, 80
	6	25.5	-9, 9, 15, 20, 25
2247+140	6	1123	-0.6, 0.6, 10, 80
	2	326	-0.7, 0.7, 1.5, 5, 15, 30, 60, 90
	1.3	484	-3, 3, 10, 30, 60, 90
2305+187	6	68	-1.5, 1.5, 3, 5, 10, 30, 60, 90
	2	41	-6, 6, 15, 30, 60, 90
2328+167	6	1192	-1.5, 1.5, 7, 20, 40, 70, 90
	2	1294	-0.7, 0.7, 5, 20, 40, 70, 90

Table A.1: Map Characteristics

Source	λ (cm)	Peak (mJy)	Contours as a percentage of peak
2331-240	6	1192	-1.5, 1.5, 7, 20, 40, 70, 90
	2	1294	-0.7, 0.7, 5, 20, 40, 70, 90
2355-082	6	68	-0.75, 0.75, 1.5, 3, 10, 30, 60, 90
	2	42	-4, 4, 7, 10, 15, 30, 60, 90

0007+106

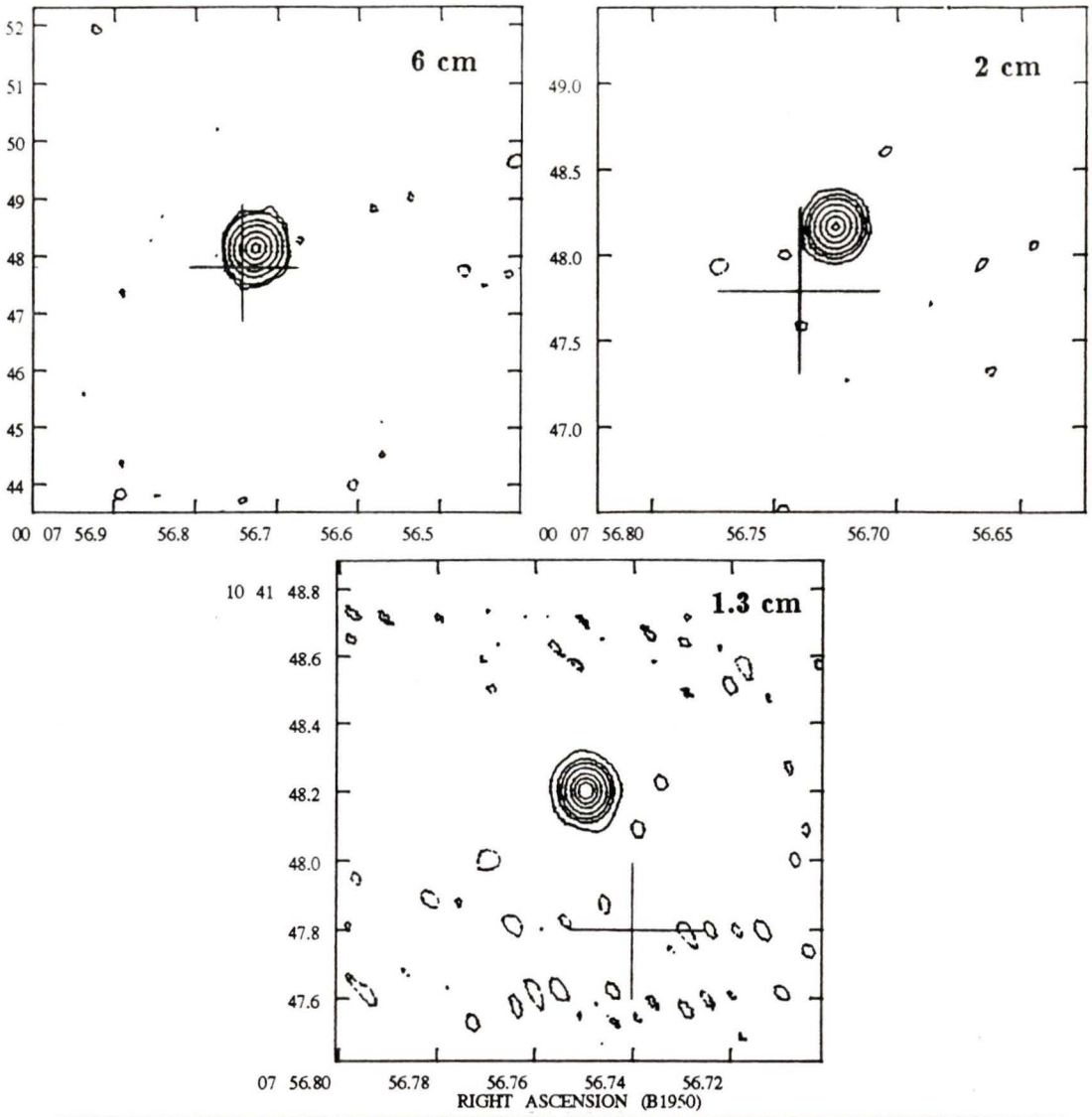

Optical images from Hutchings *et al.* (1984a)

0017+257

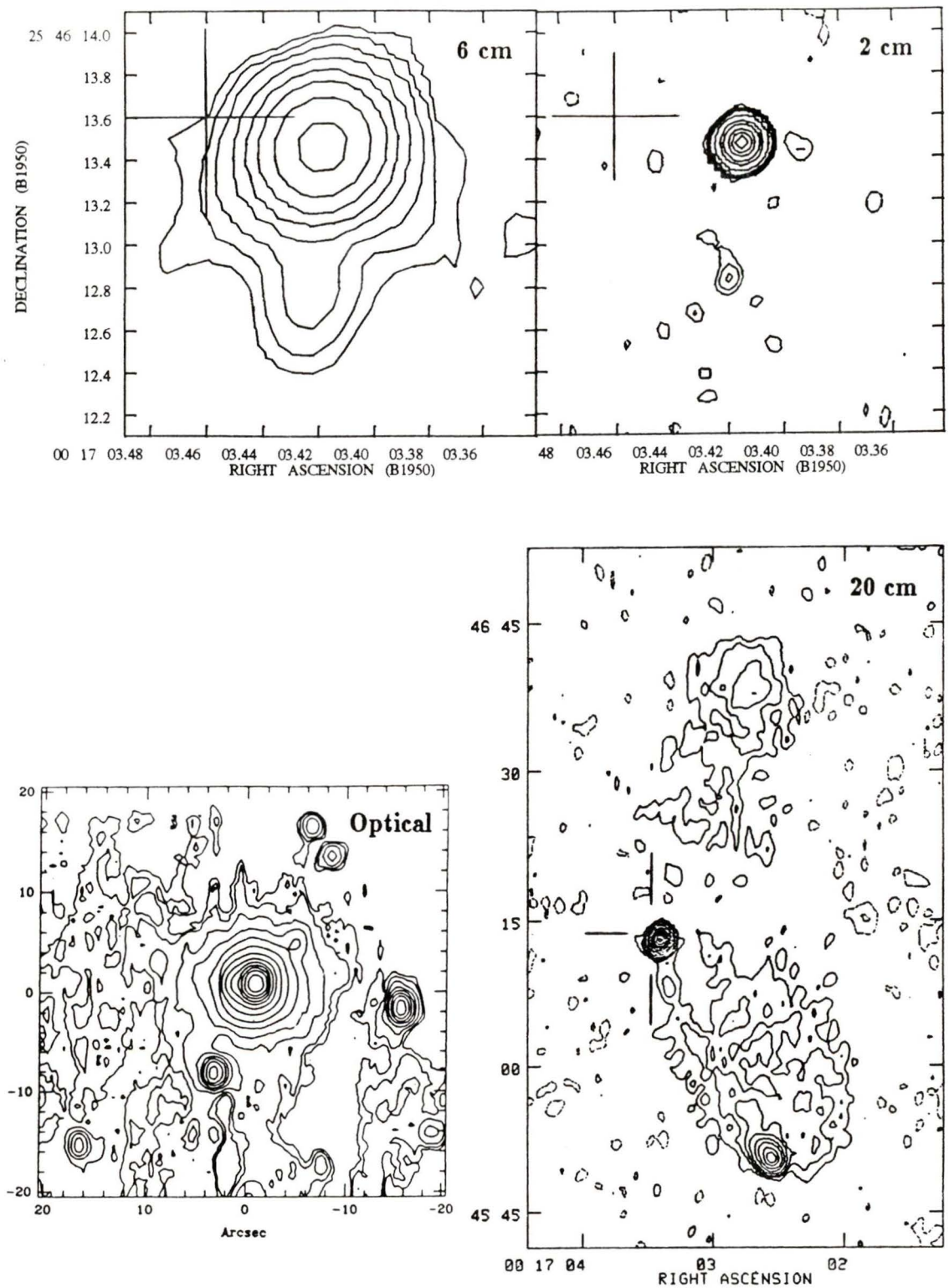

20 cm image from Gower and Hutchings (1984)

Optical image from Hutchings, Johnson and Pyke (1988)

0041+119

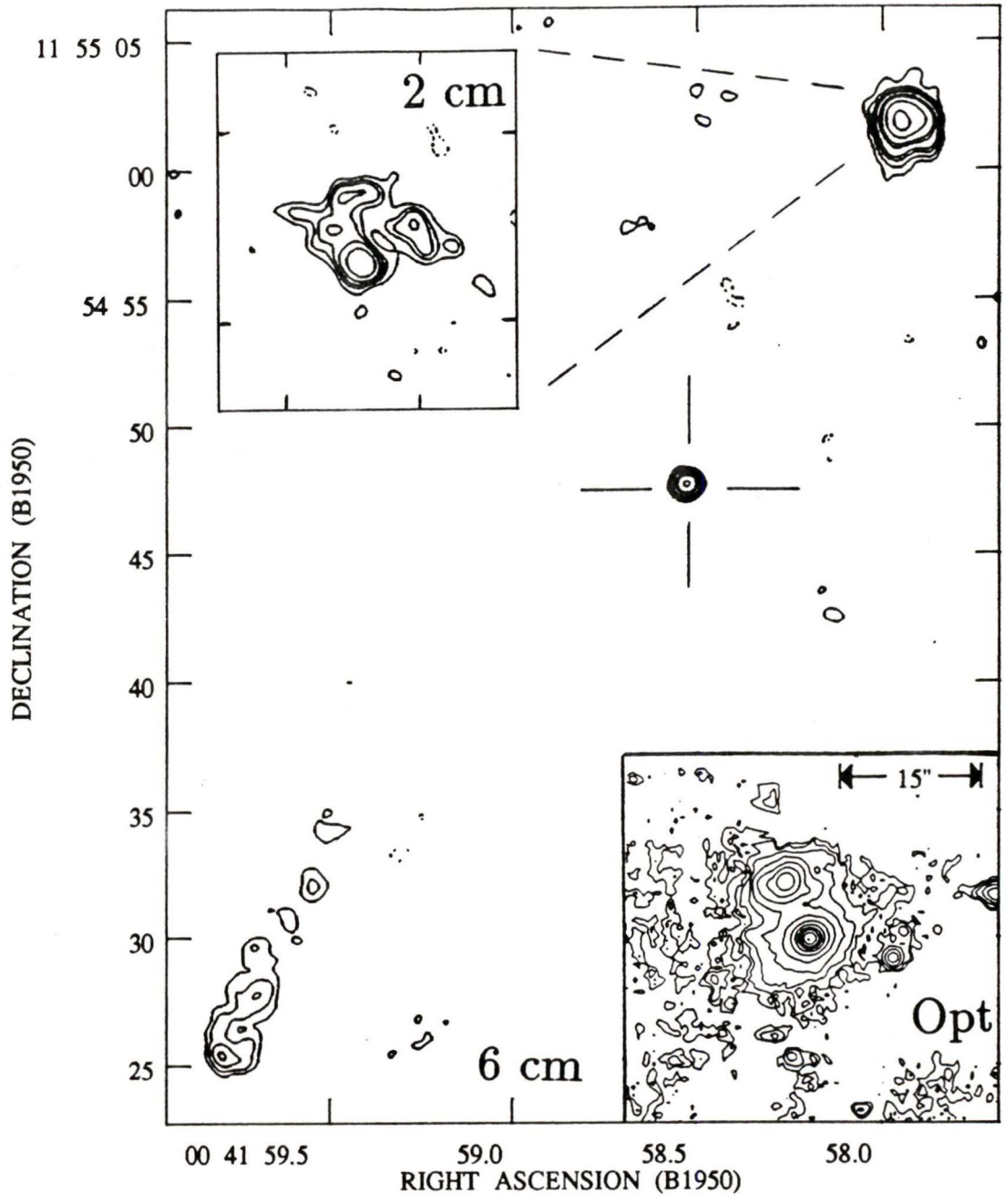

Optical image from Hutchings, Johnson and Pyke (1988)

0100+108

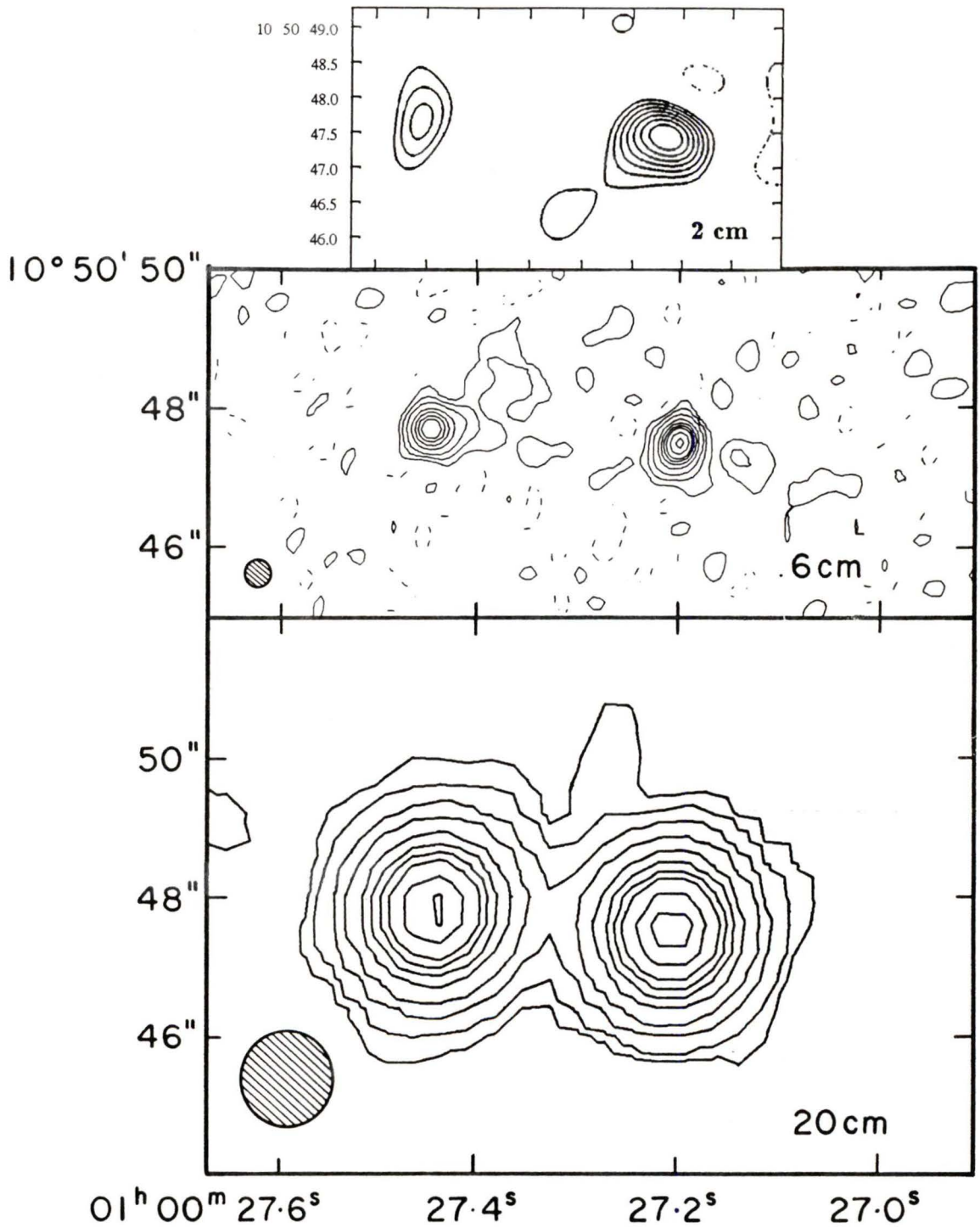

6, 20 cm images from Gower and Hutchings (1984)

0137+012

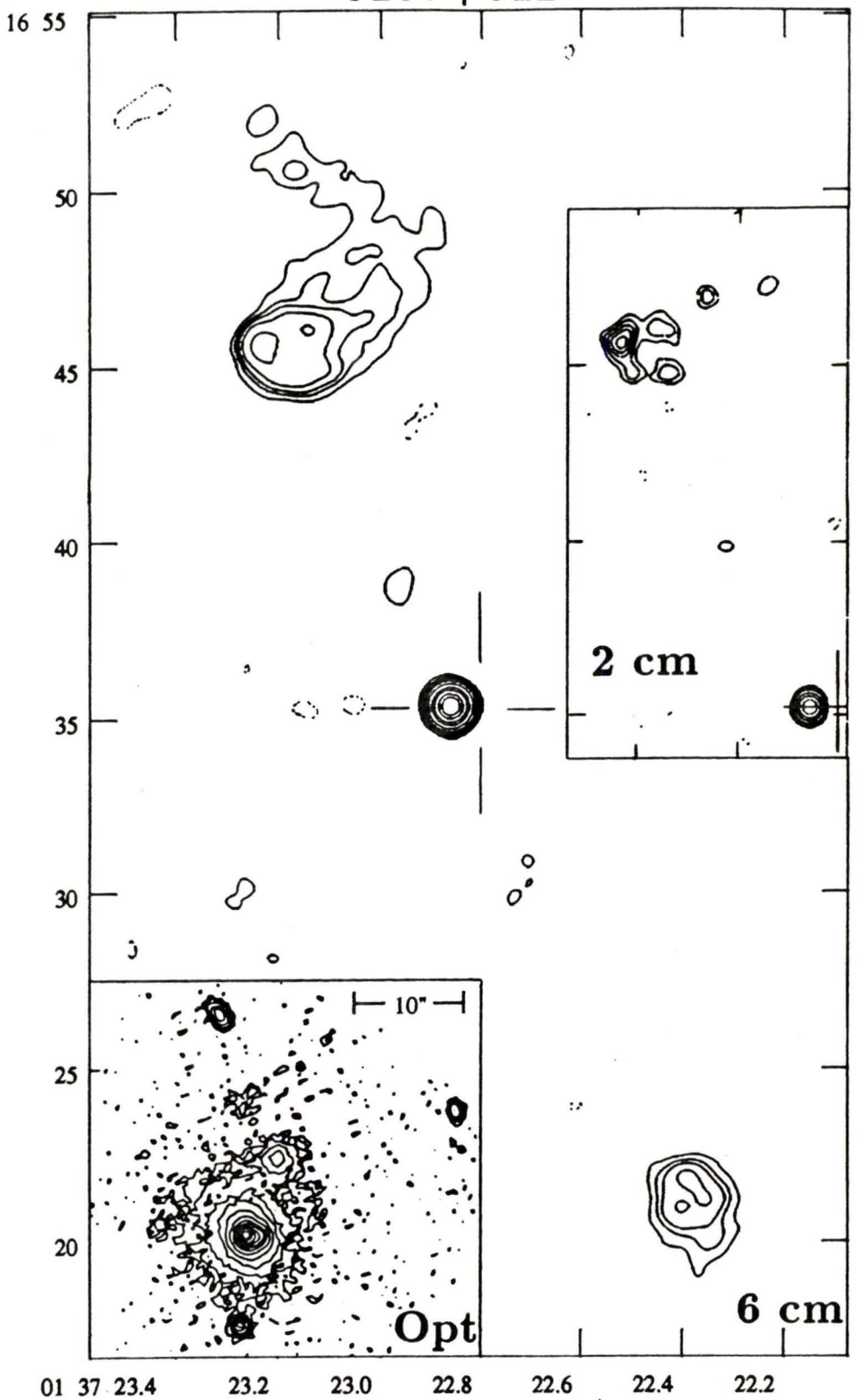

Unpublished optical image provided by J. Hutchings

0241+622

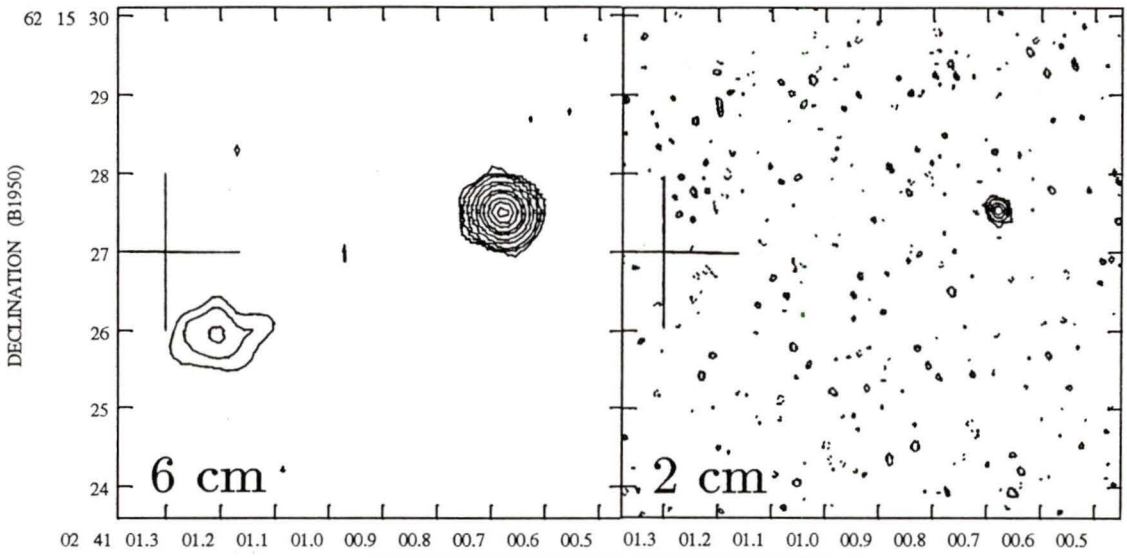

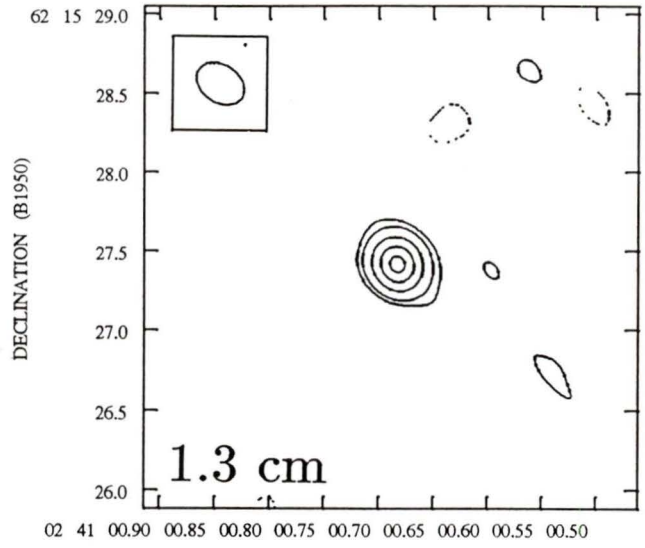

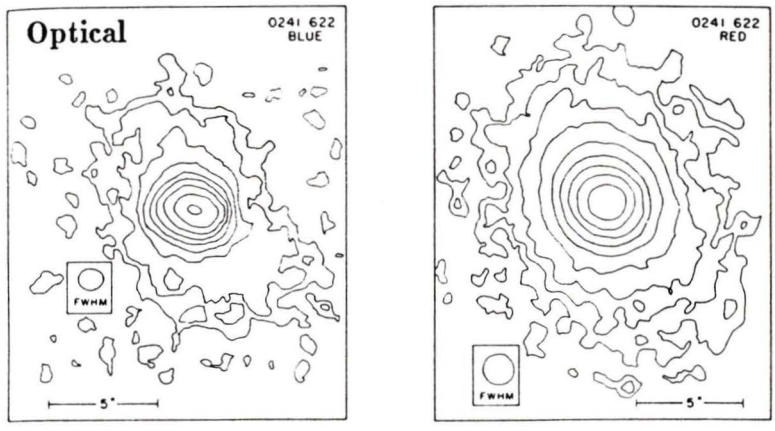

Optical images from Hutchings (1982)

0736+017

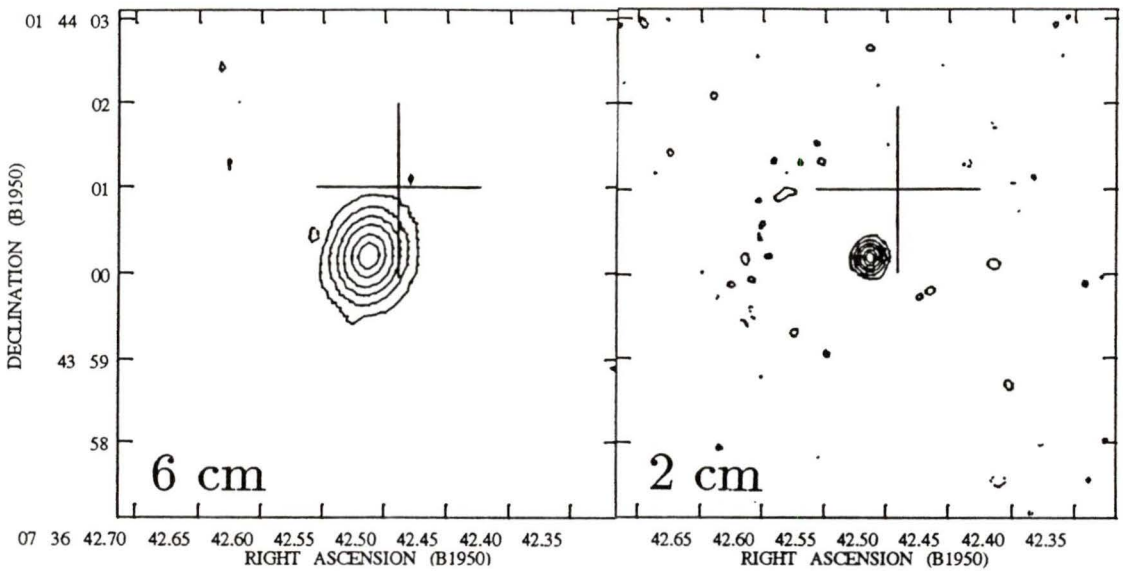

Optical

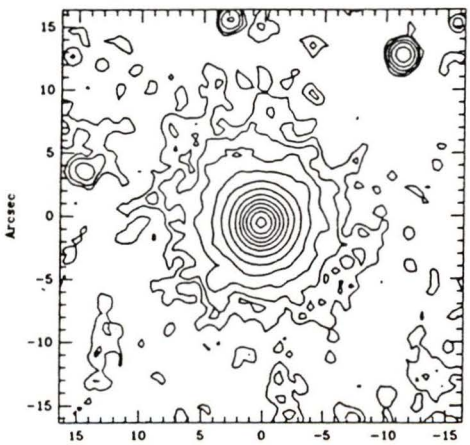

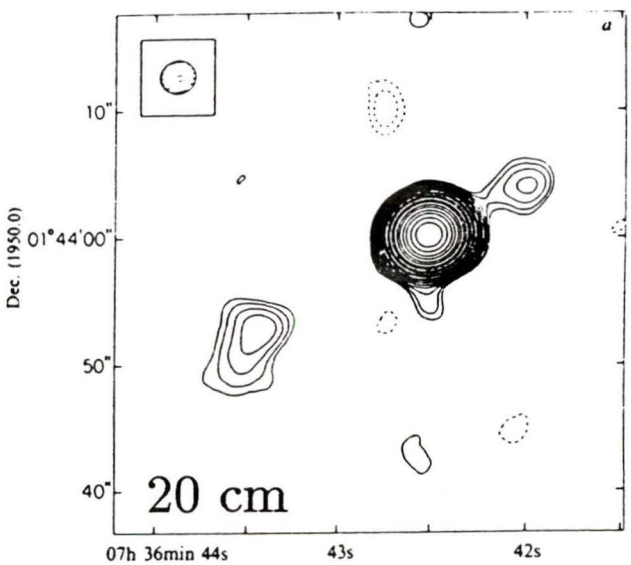

Optical image from Hutchings, Johnson and Pyke (1988)
20 cm image from Antonucci and Ulvestad (1984)

0742+318

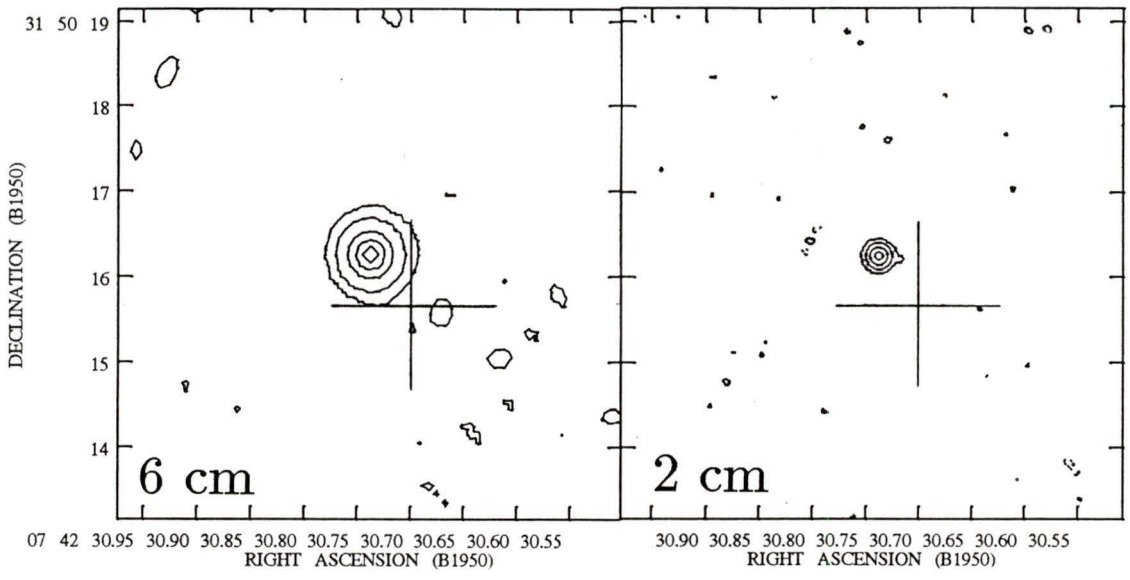

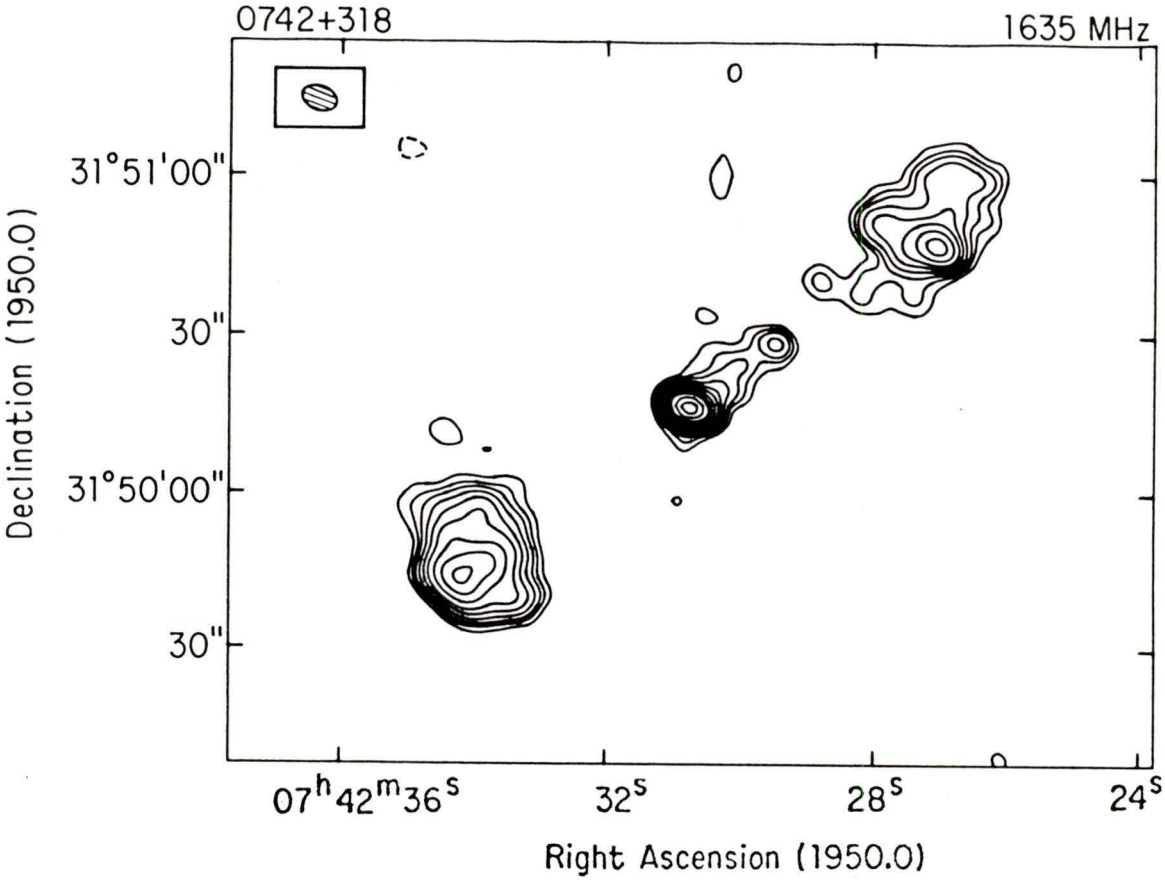

20 cm image from Neff (1982)

0829+046

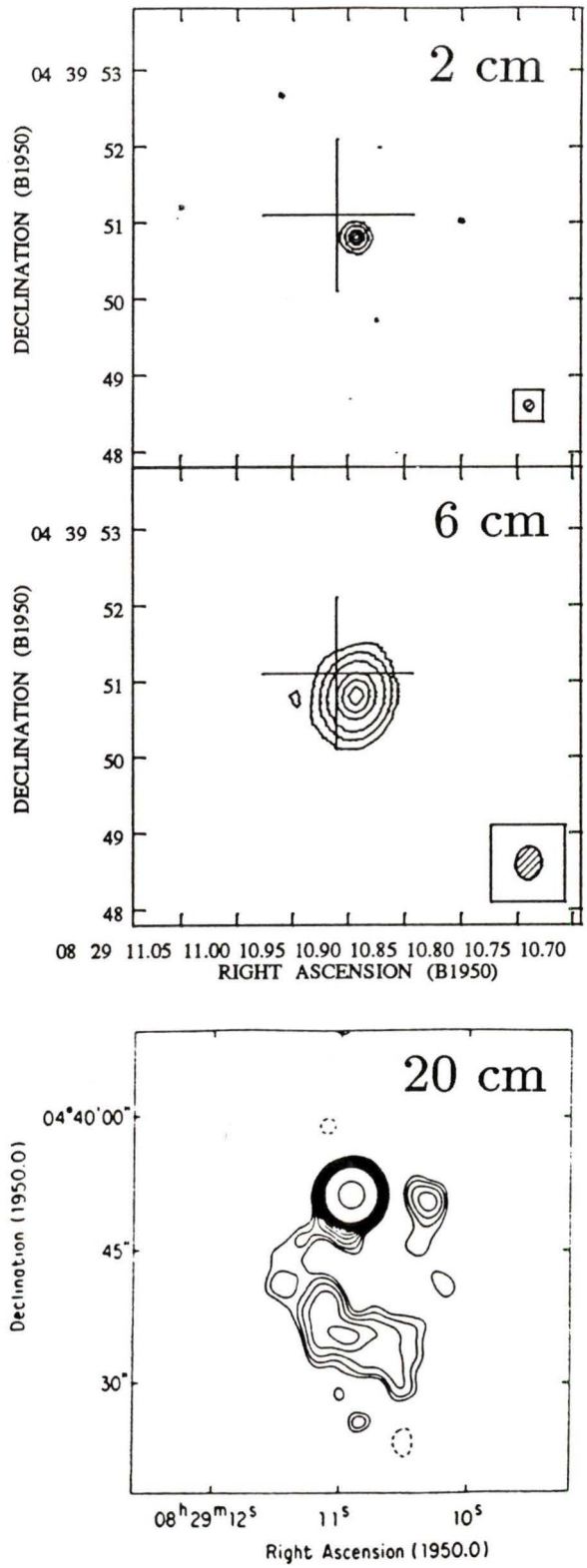

20 cm image from Antonucci and Ulvestad (1985)

0846+100

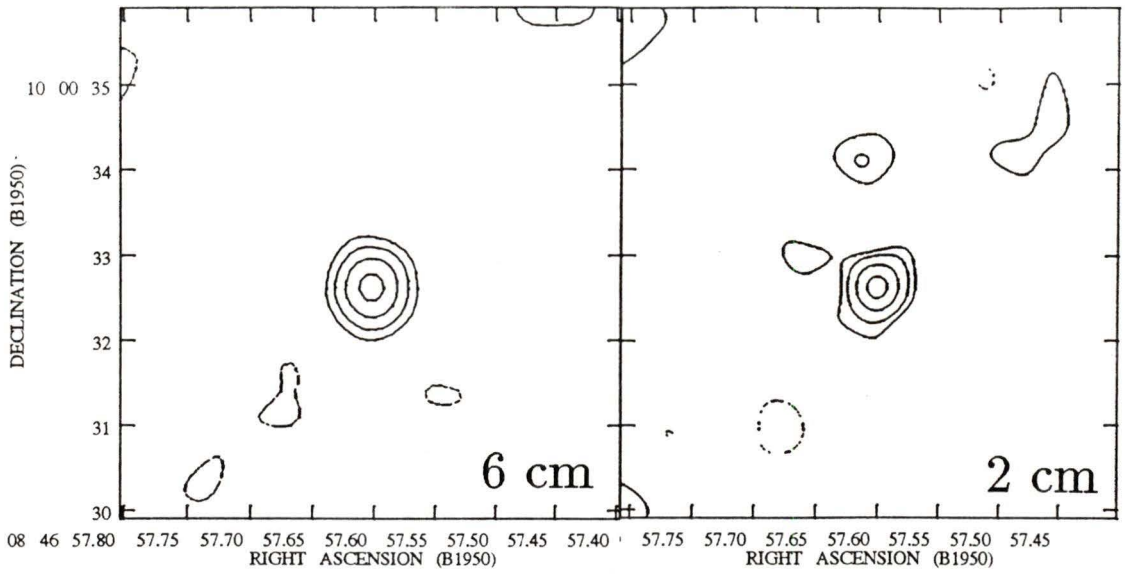

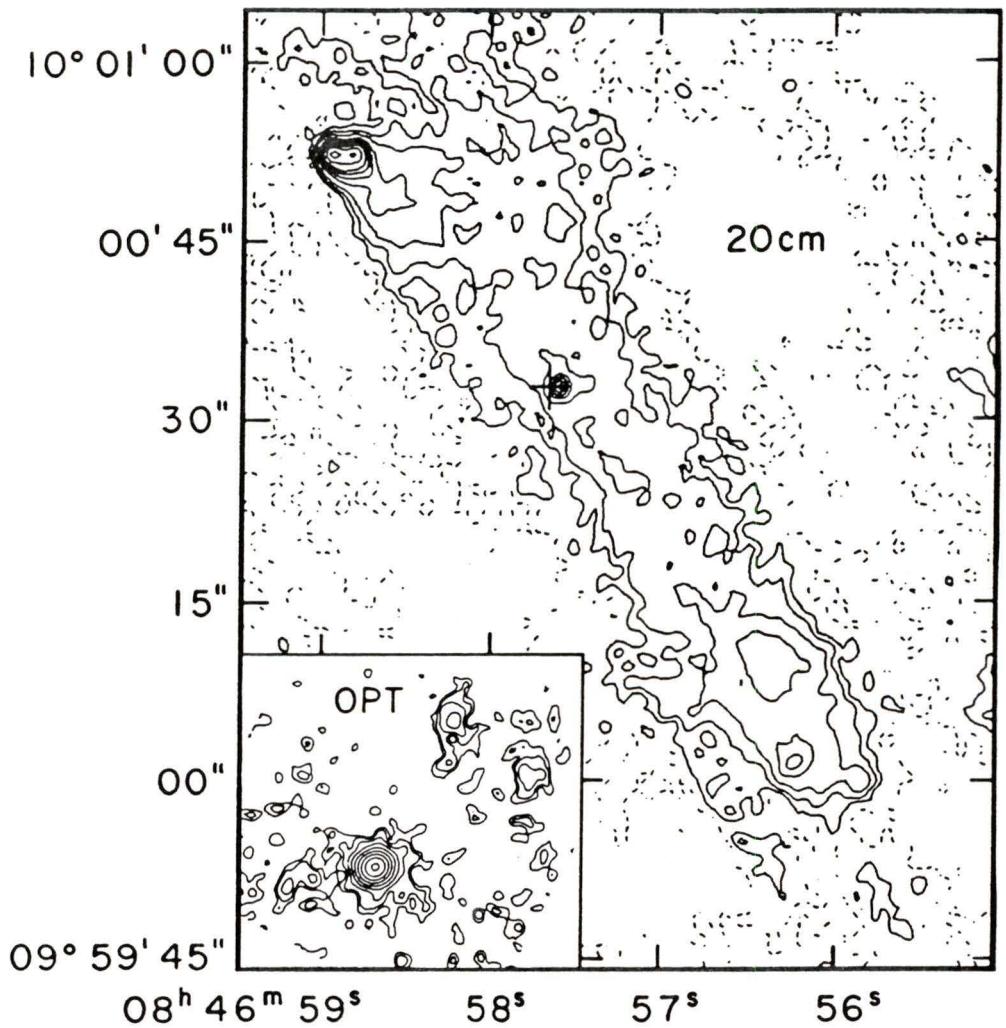

20 cm and optical images from Gower and Hutchings (1984)

0952+097

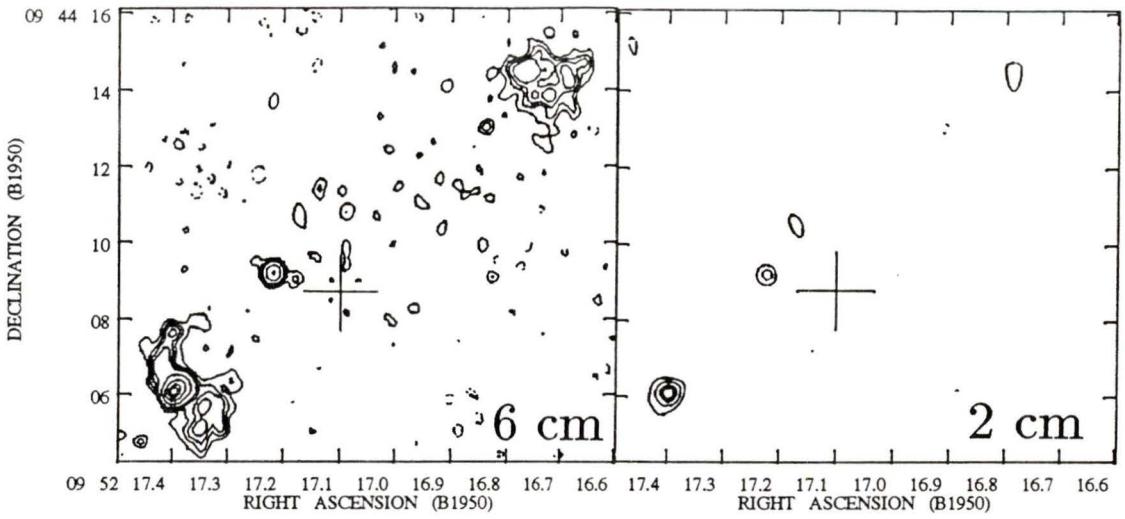

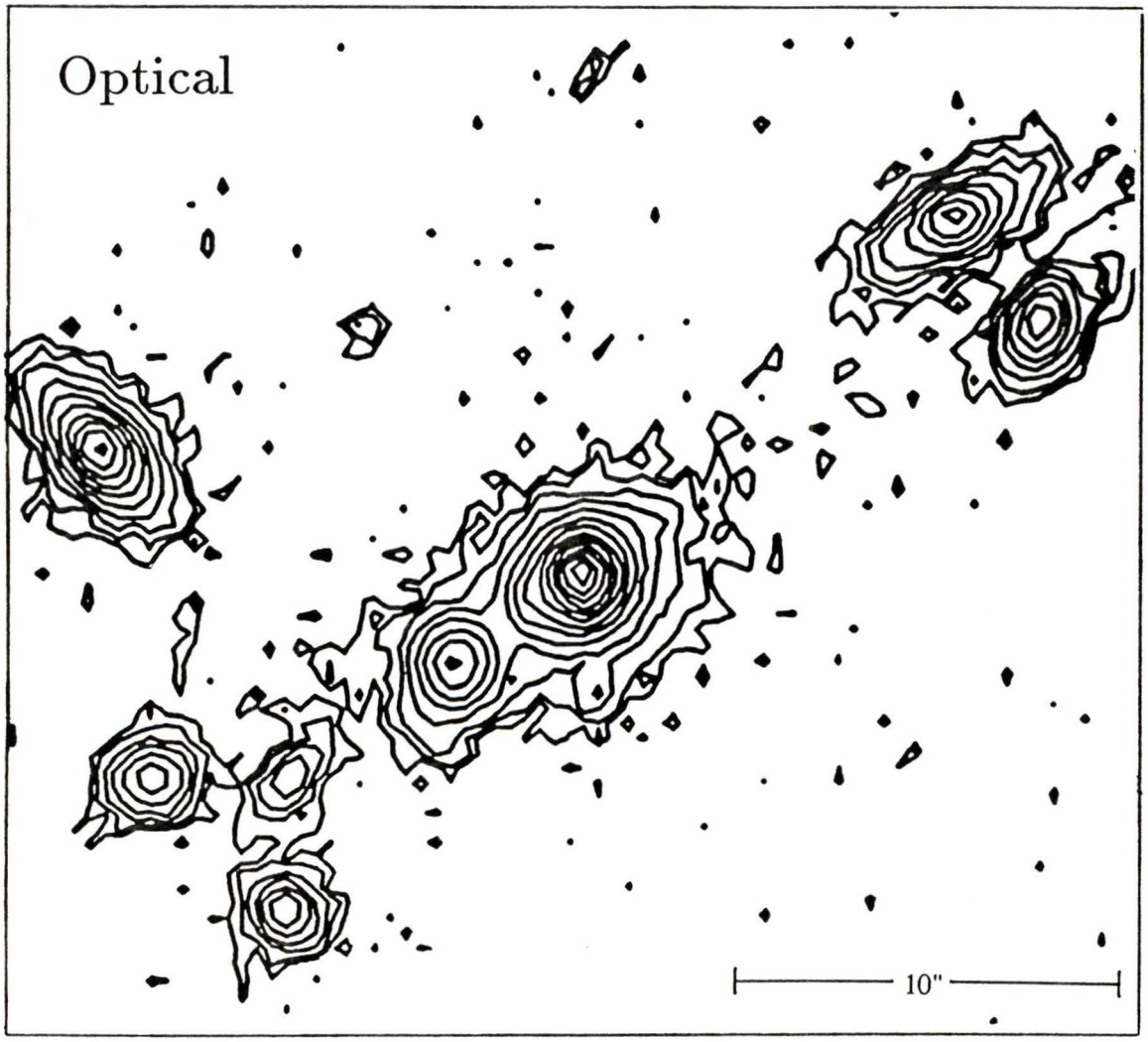

Unpublished optical image provided by J. Hutchings

1004+130

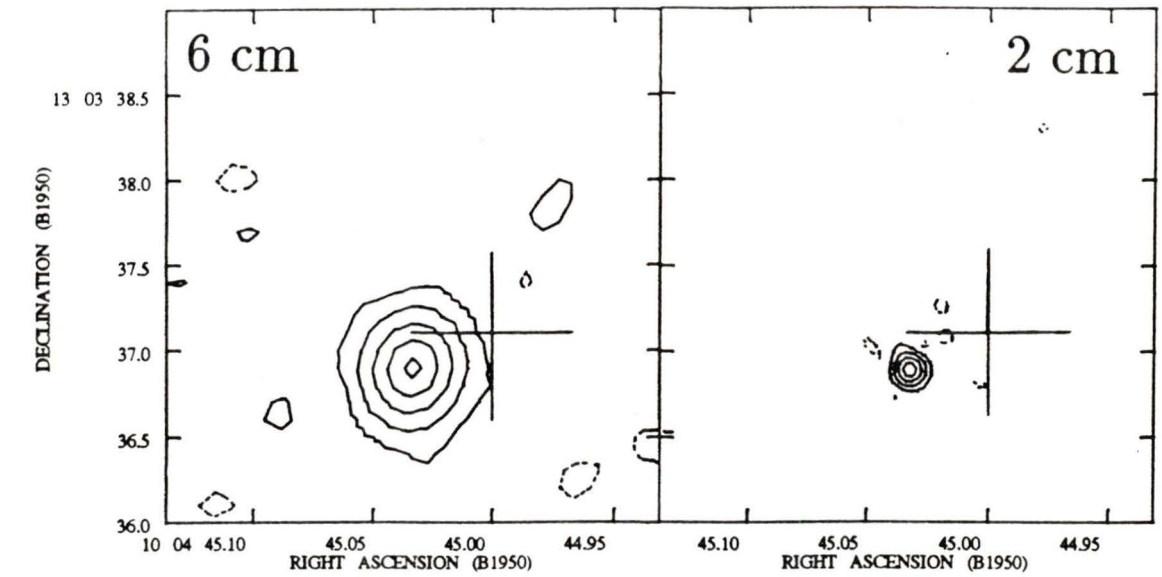

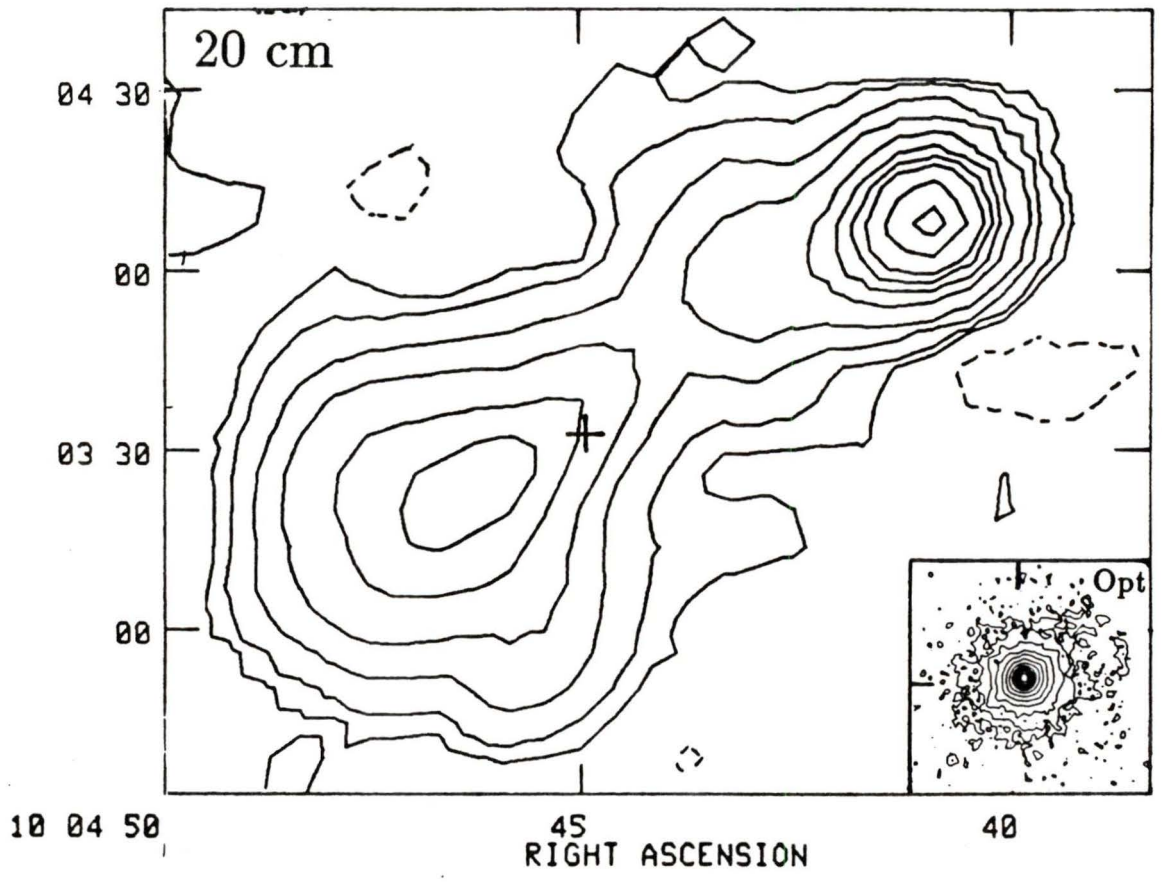

Unpublished 20 cm C configuration image provided by A Gower
Optical image from Hutchings, Johnson and Pyke (1988)

1020-103

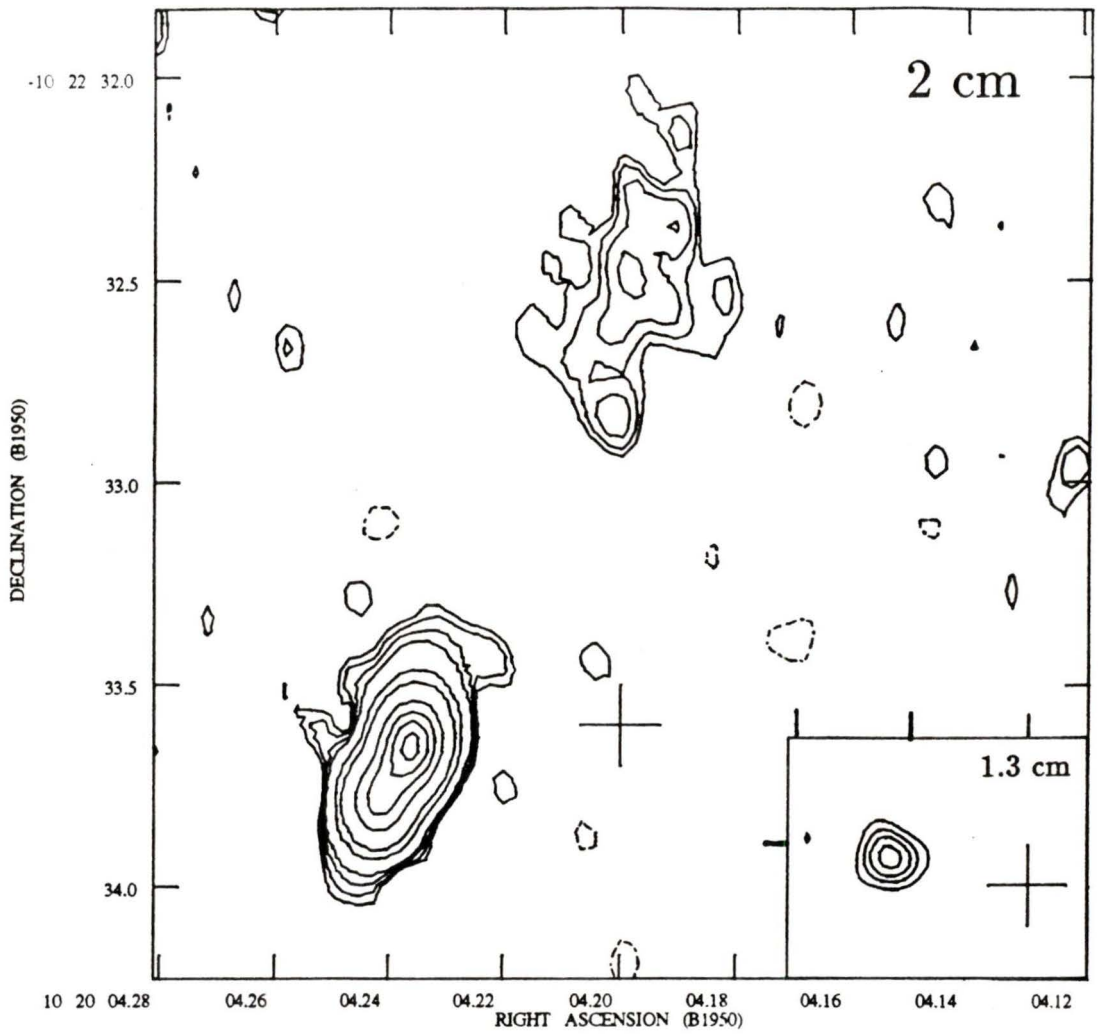

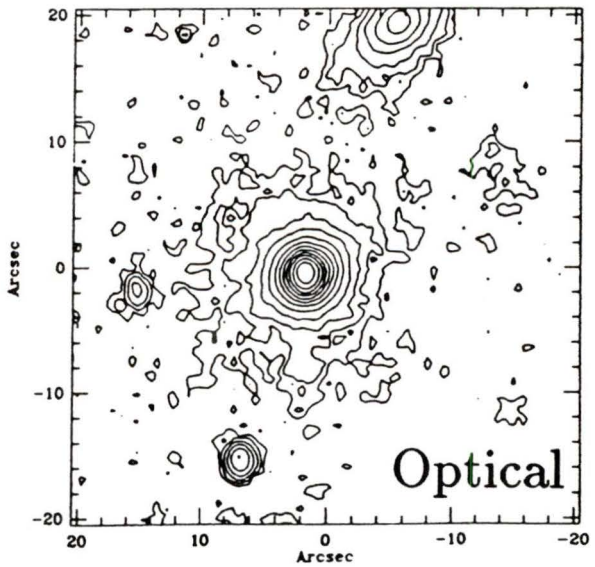

Optical image from Hutchings, Johnson and Pyke (1988)

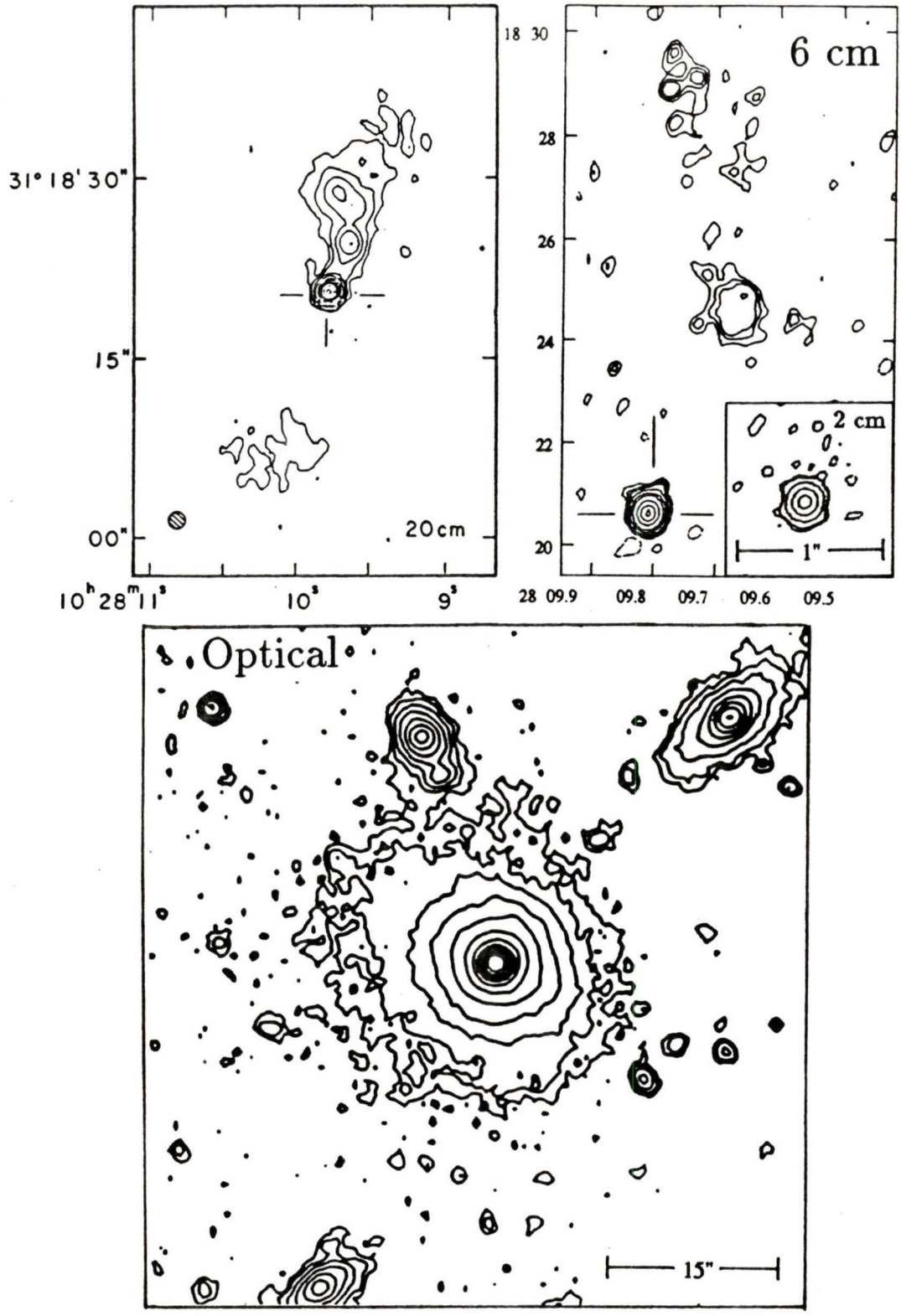

Optical image from Hutchings, Johnson and Pyke (1988)
20 cm image from Gower and Hutchings (1984)

1203+011

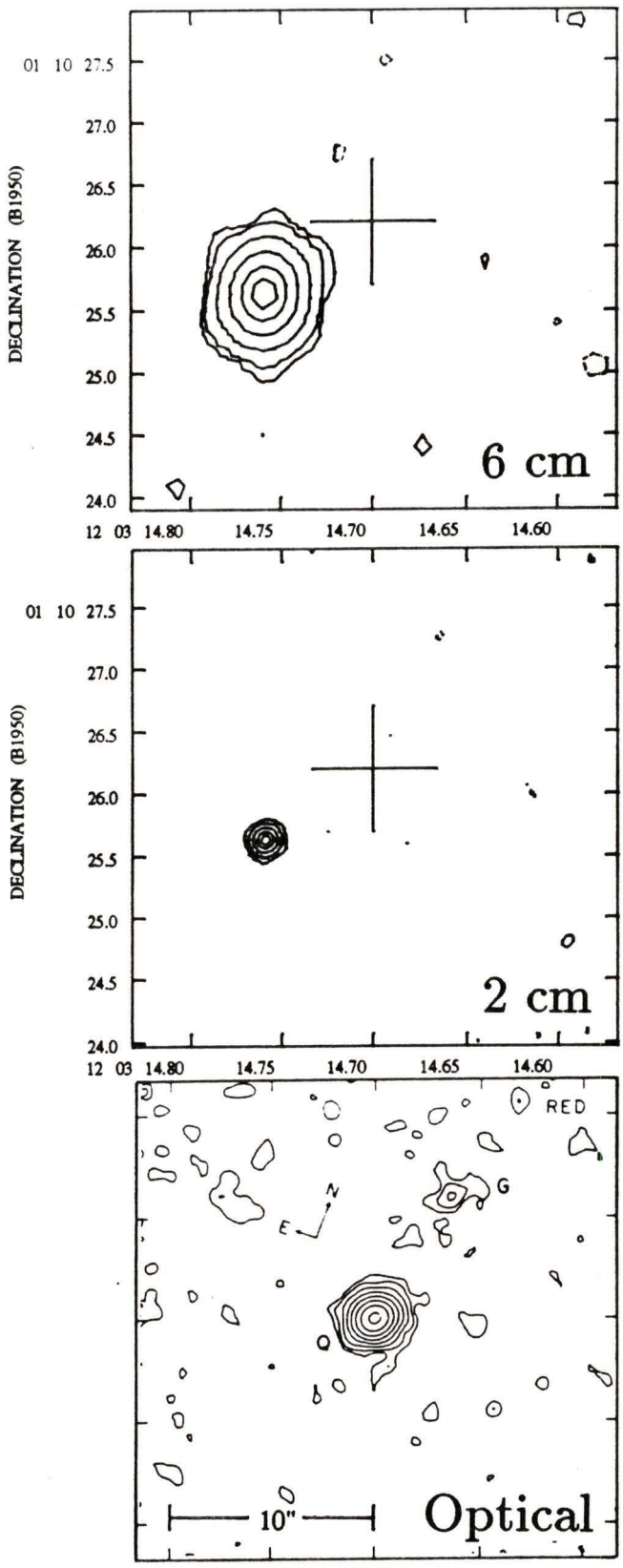

Optical image from Hutchings, Johnson and Pyke (1988)

1217+023

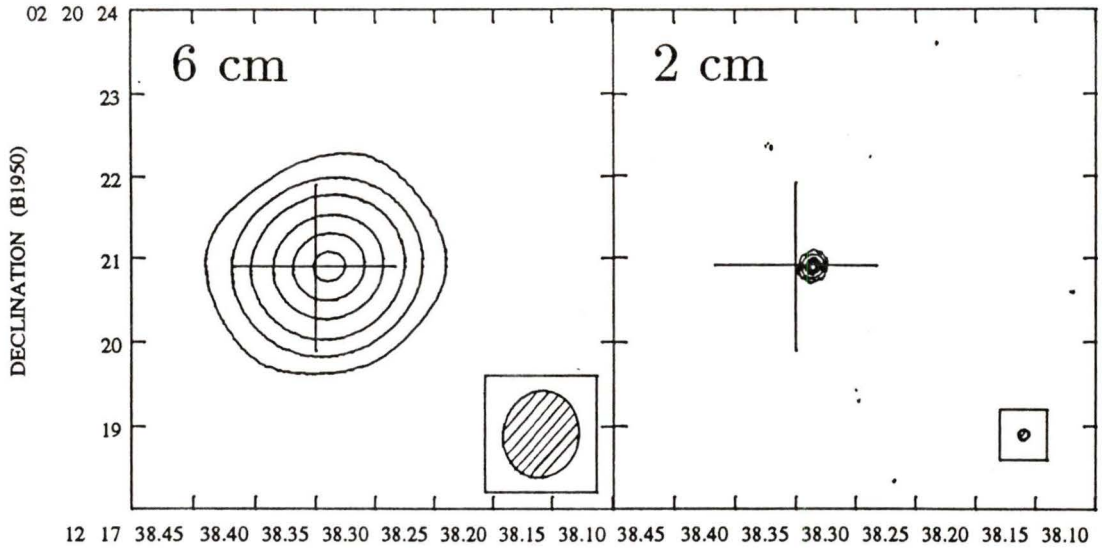

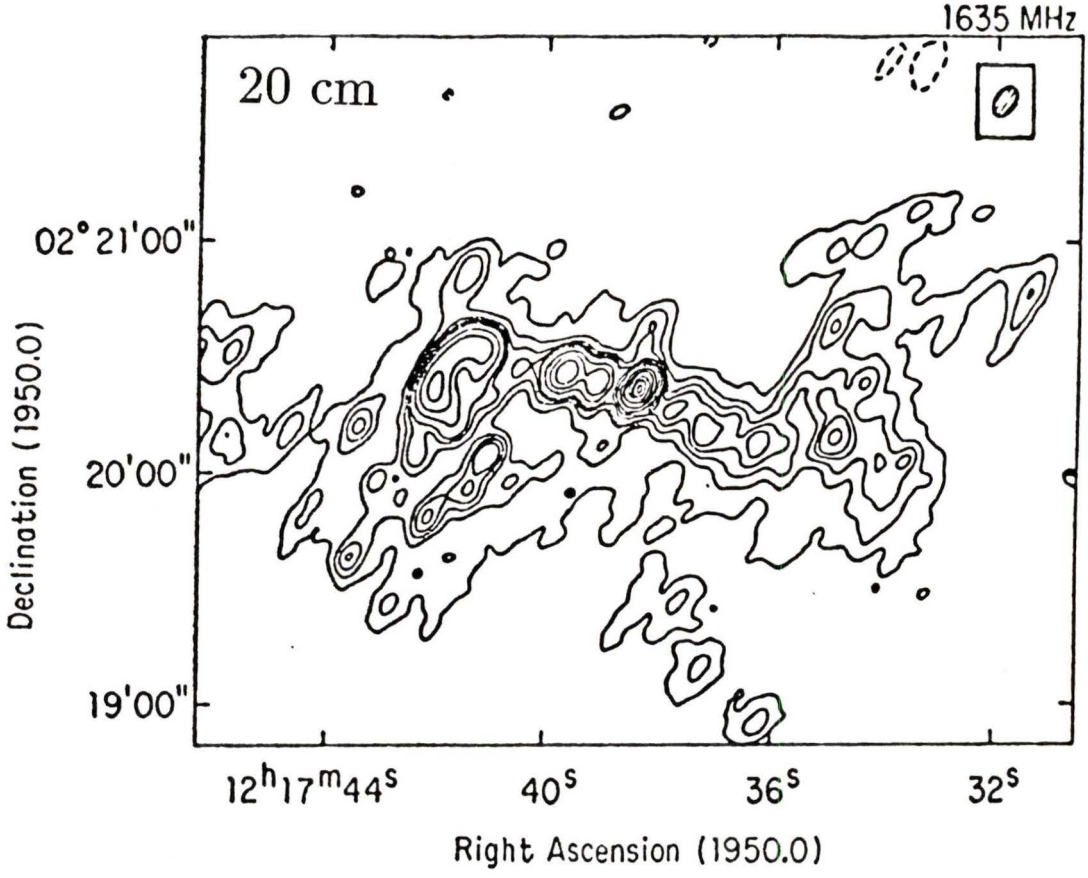

20 cm image from Neff (1982)

1223+252

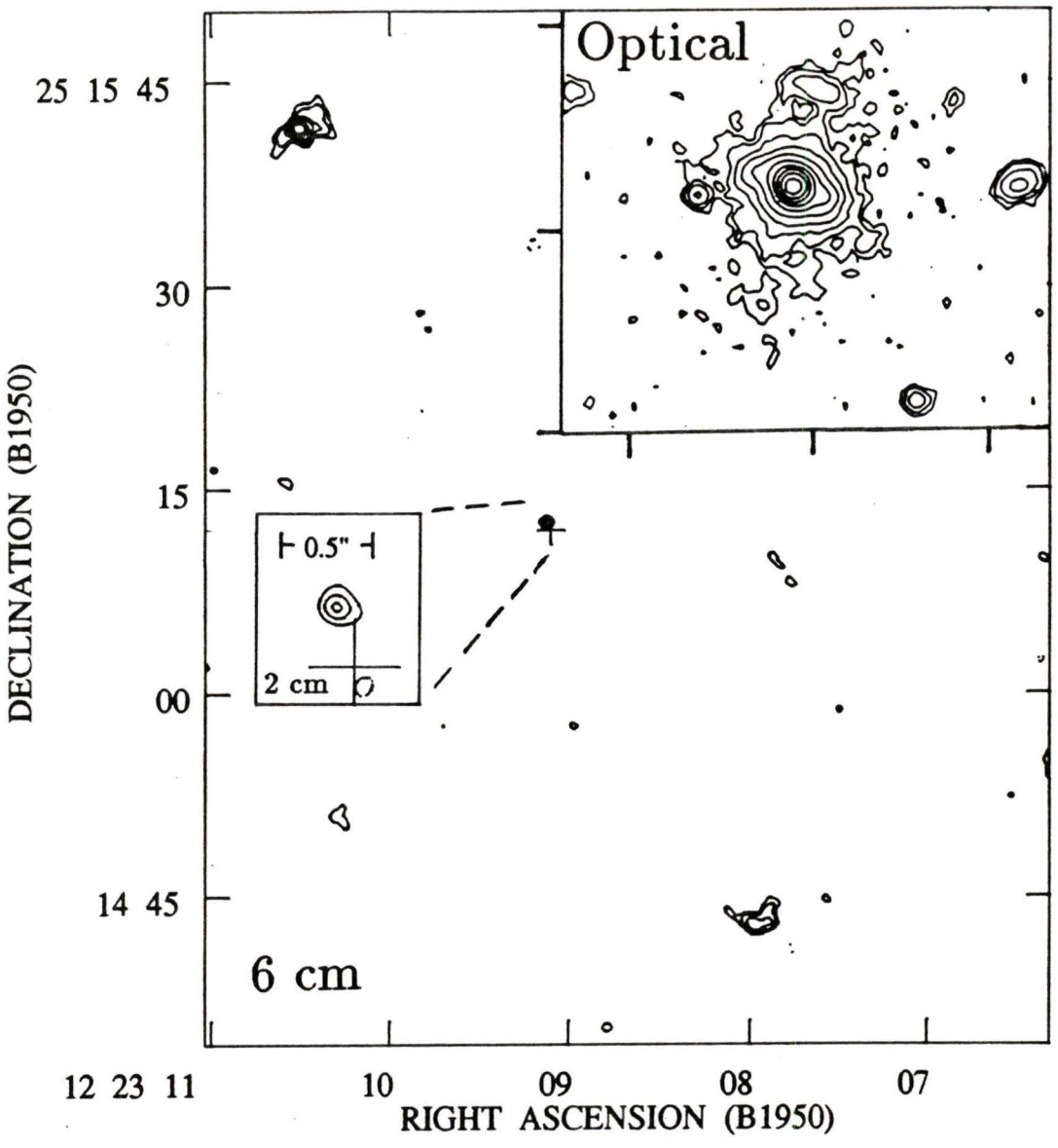

Optical image from Hutchings, Johnson and Pyke (1988)

1243-072

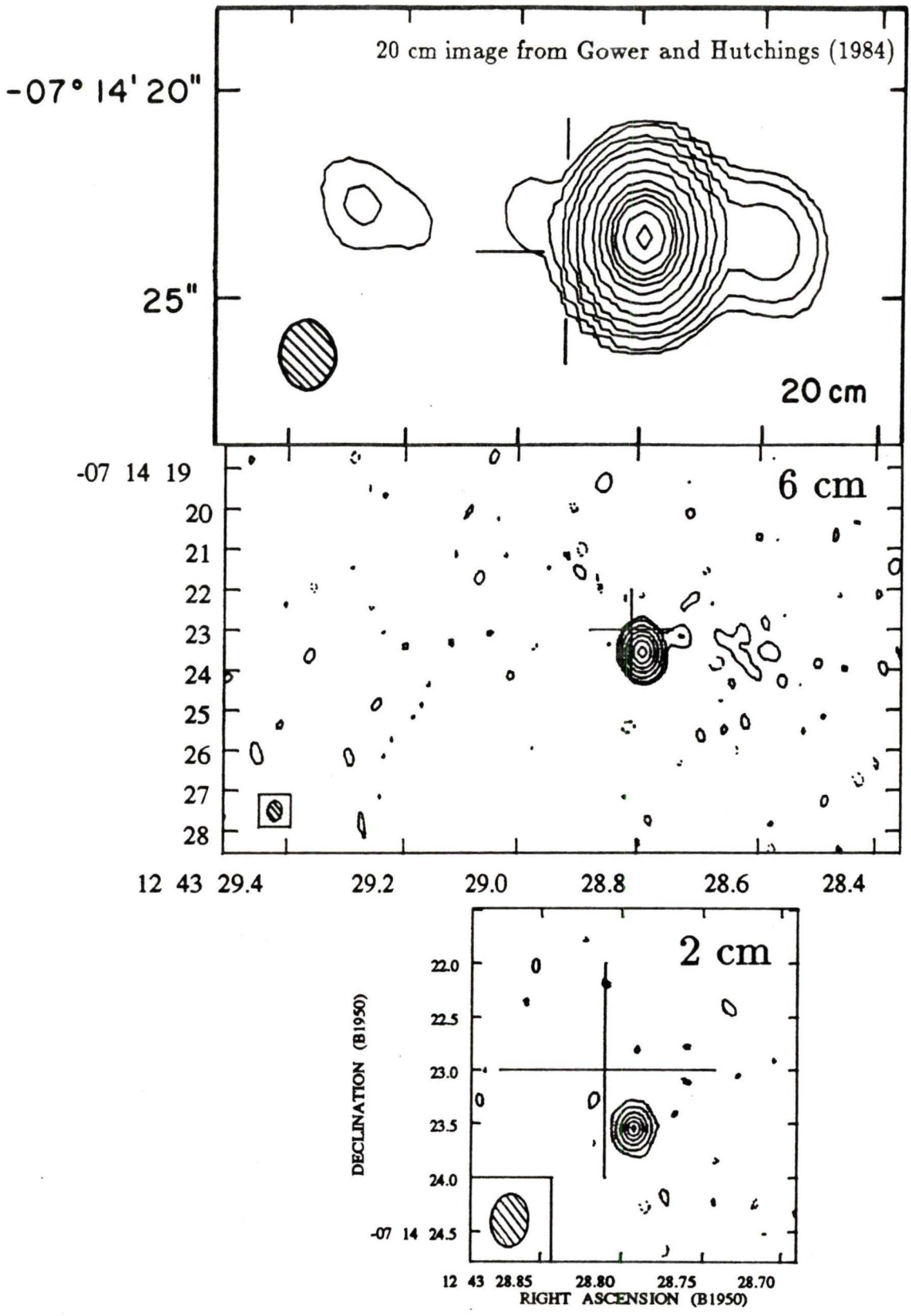
20 cm image from Gower and Hutchings (1984)
-07° 14' 20"
25"
20 cm
-07 14 19
20
21
22
23
24
25
26
27
28
6 cm
12 43 29.4
29.2
29.0
28.8
28.6
28.4
2 cm
22.0
22.5
23.0
23.5
24.0
-07 14 24.5
DECLINATION (B1950)
12 43 28.85
28.80
28.75
28.70
RIGHT ASCENSION (B1950)

1302-102

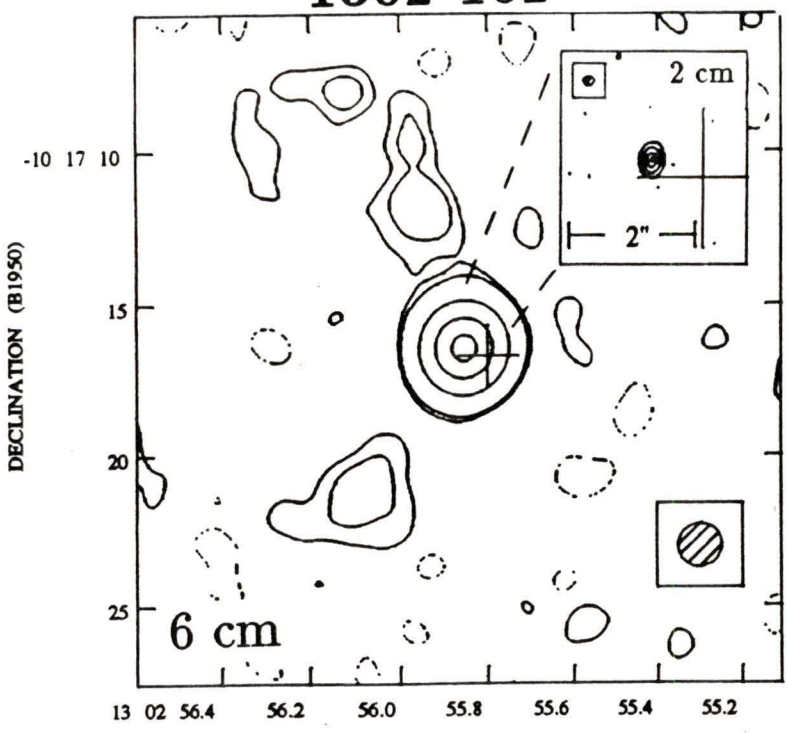

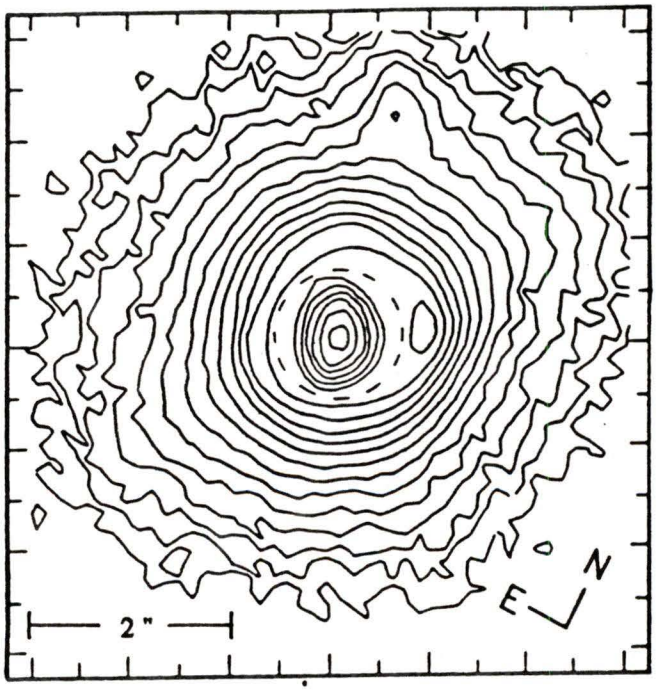

Optical image from Hutchings and Neff (1992)

1525+227

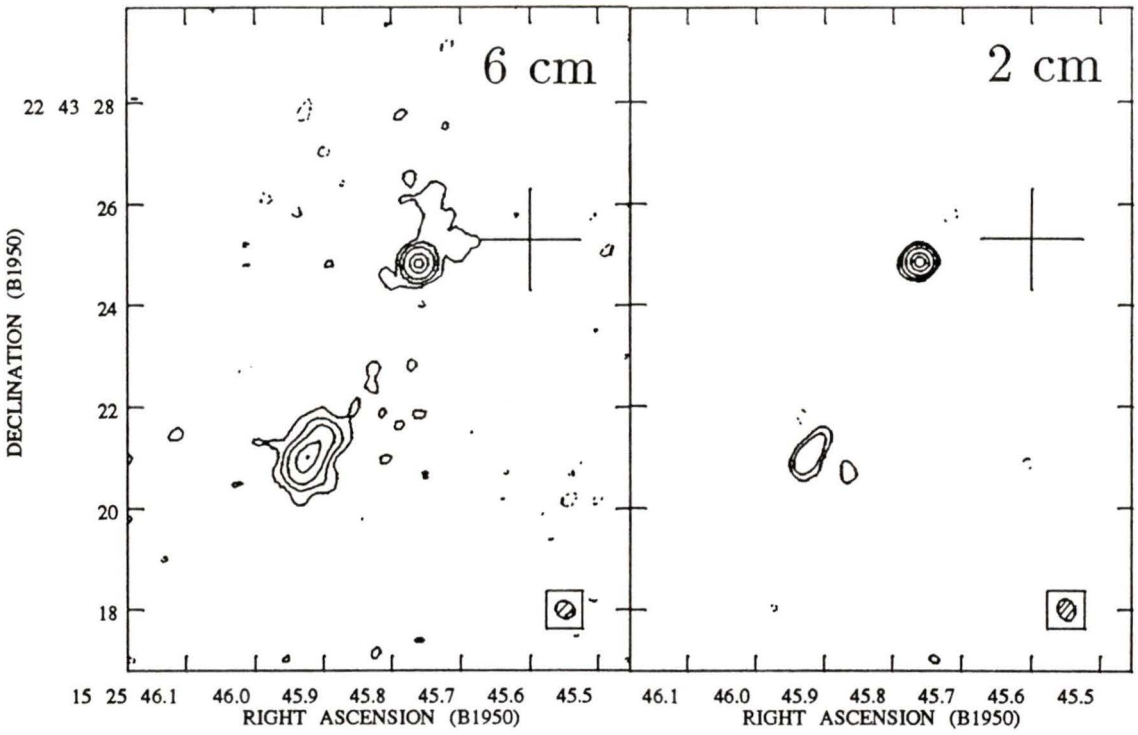

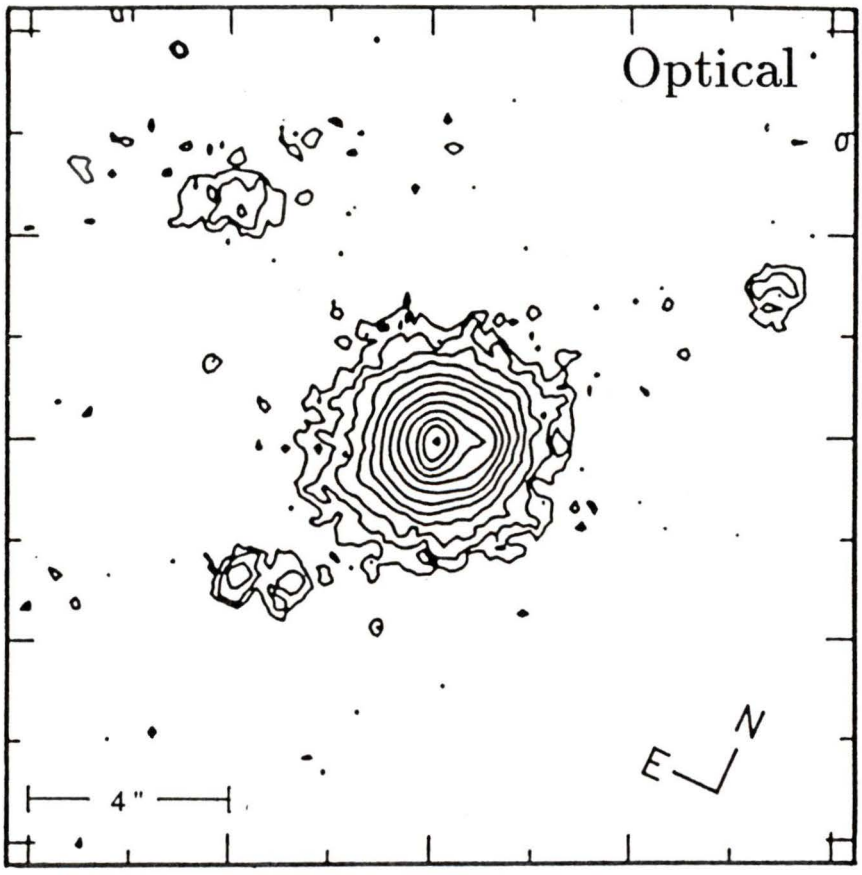

Optical image from Hutchings and Neff (1992)

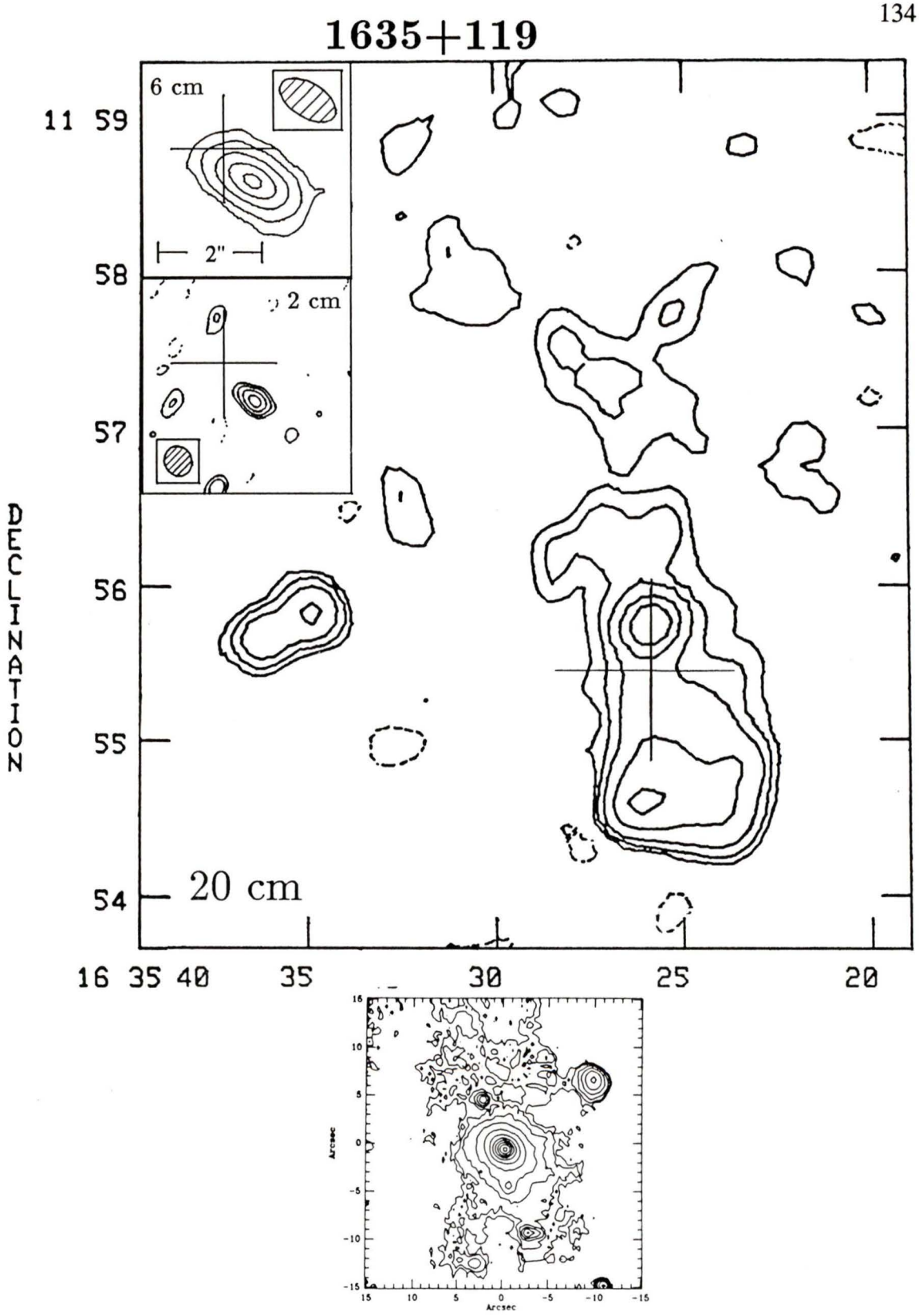

Optical image from Hutchings, Johnson and Pyke (1988)
Unpublished 20 cm image provided by A Gower

1721+343

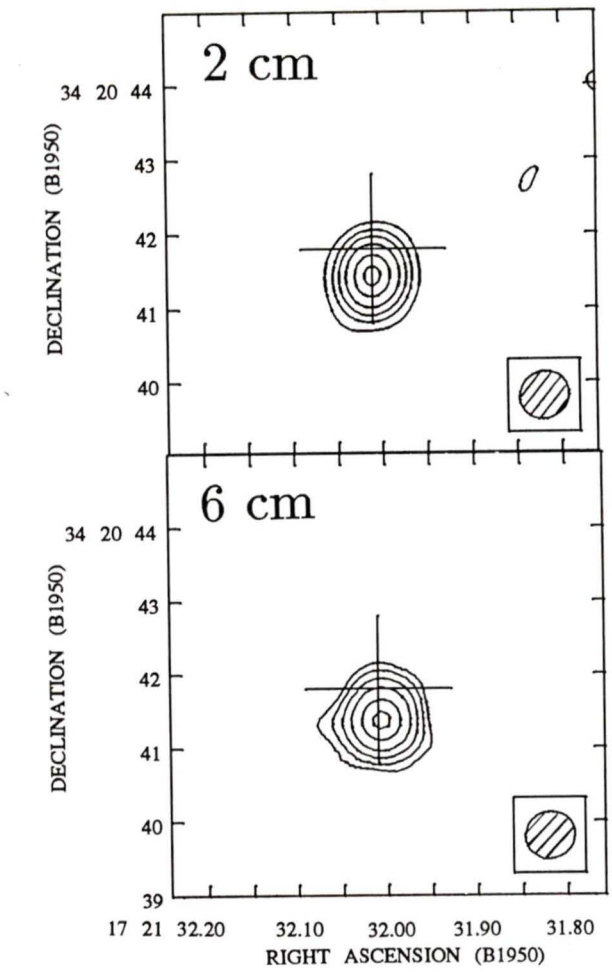

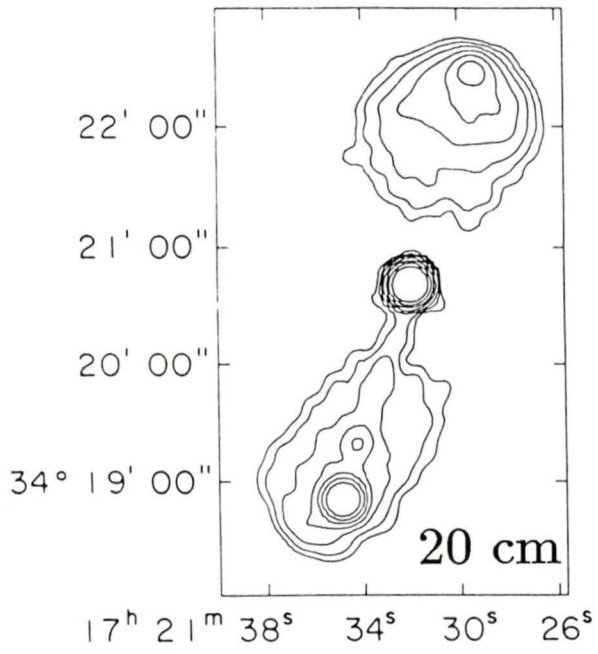

20 cm image from Barthel (1987)

1725+044

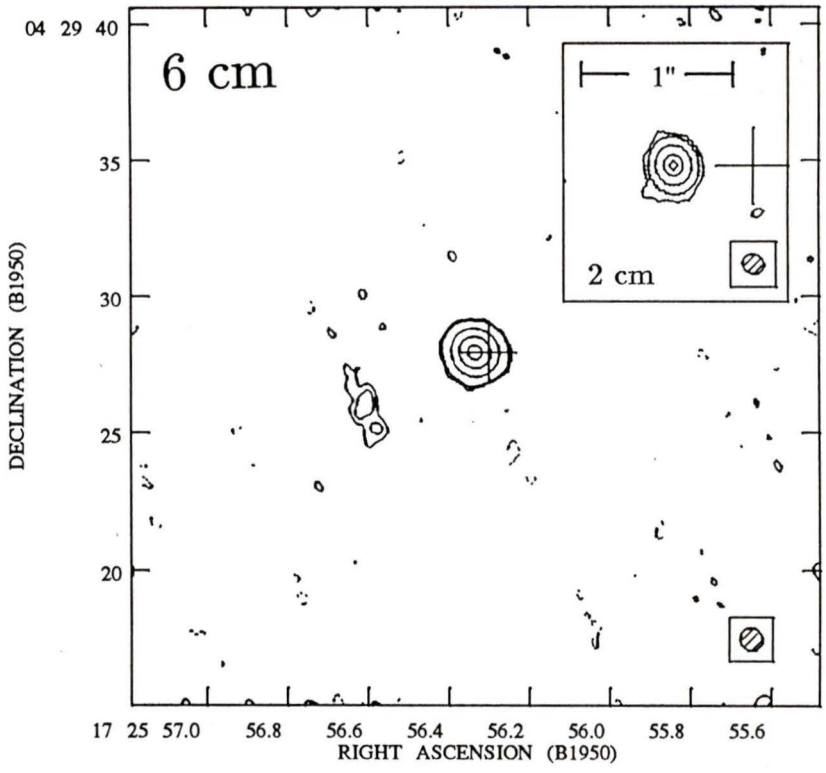

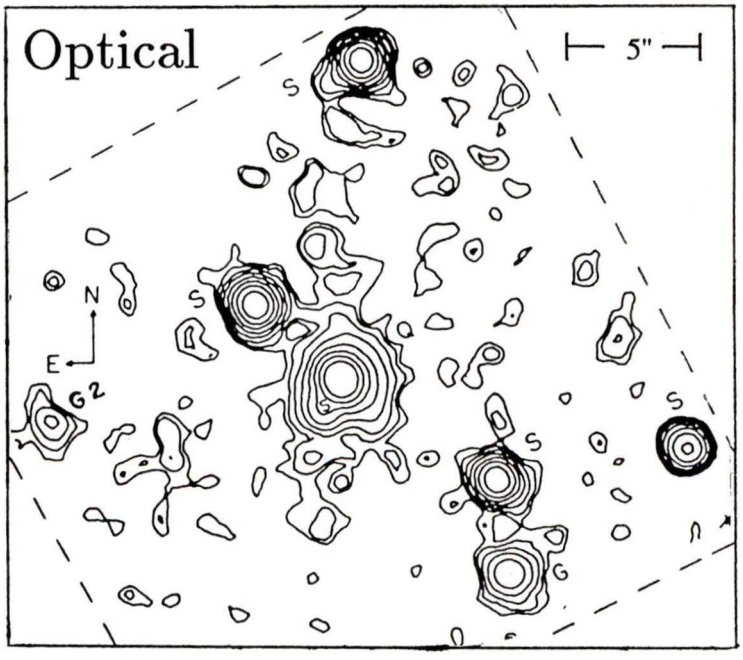

Optical image from Hutchings *et al.* (1984a)

1739+184

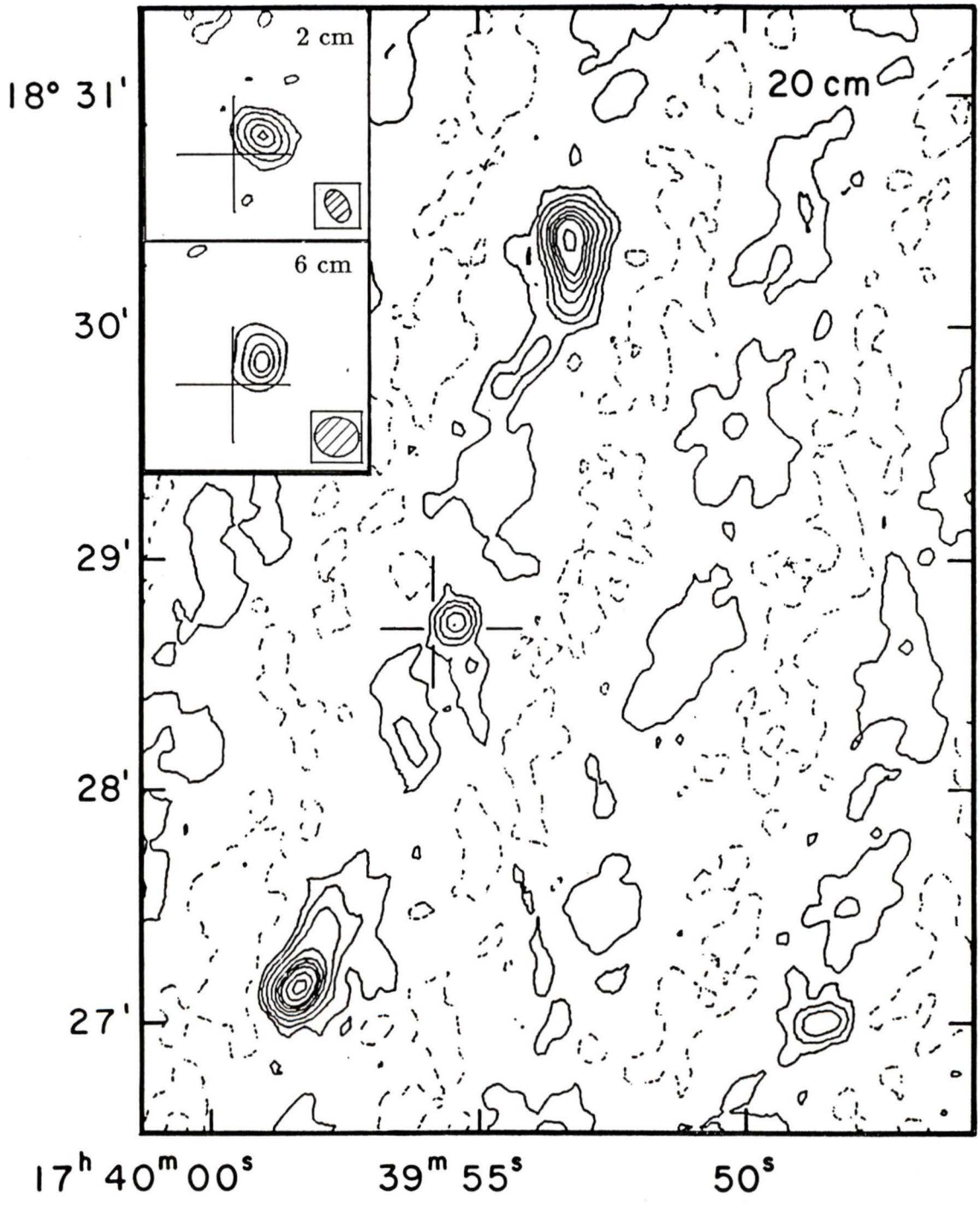

20 cm image from Gower and Hutchings (1984)

2135-147

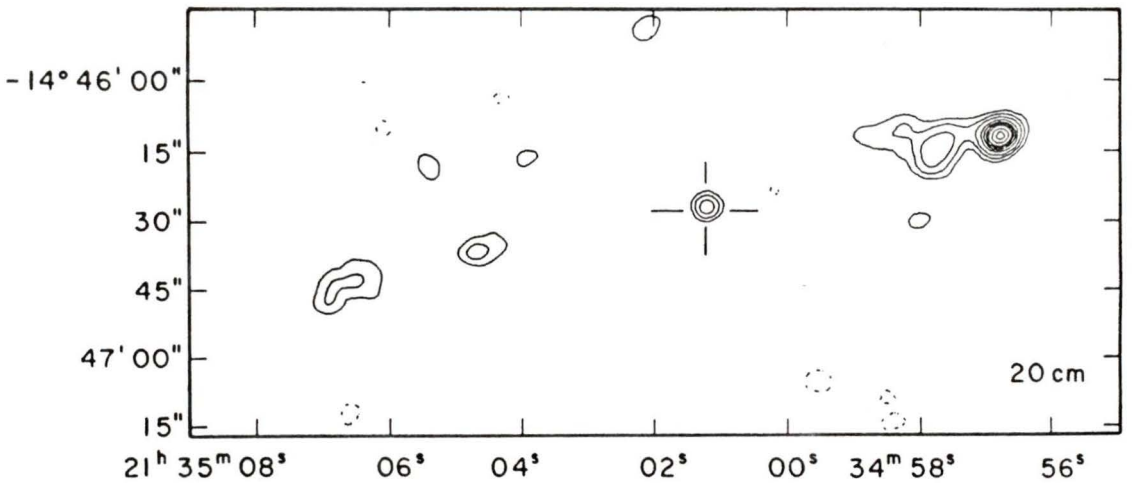

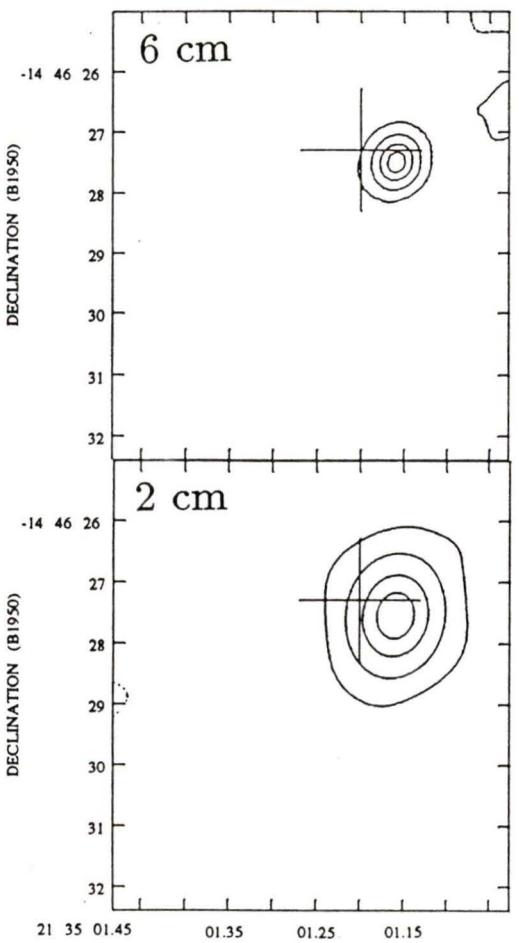

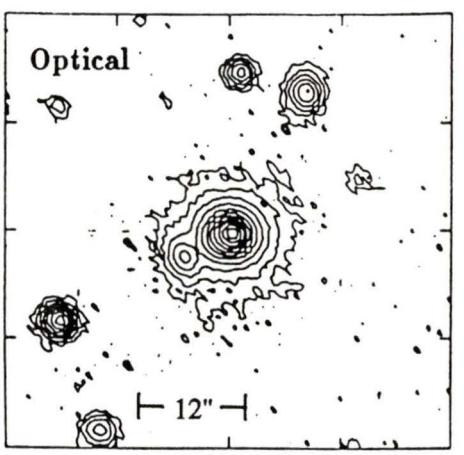

Optical image from Smith *et al.* (1986)
20 cm image from Gower and Hutchings (1984)

2141+175

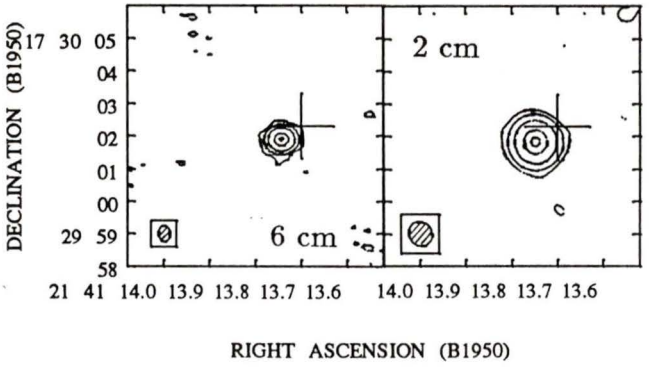

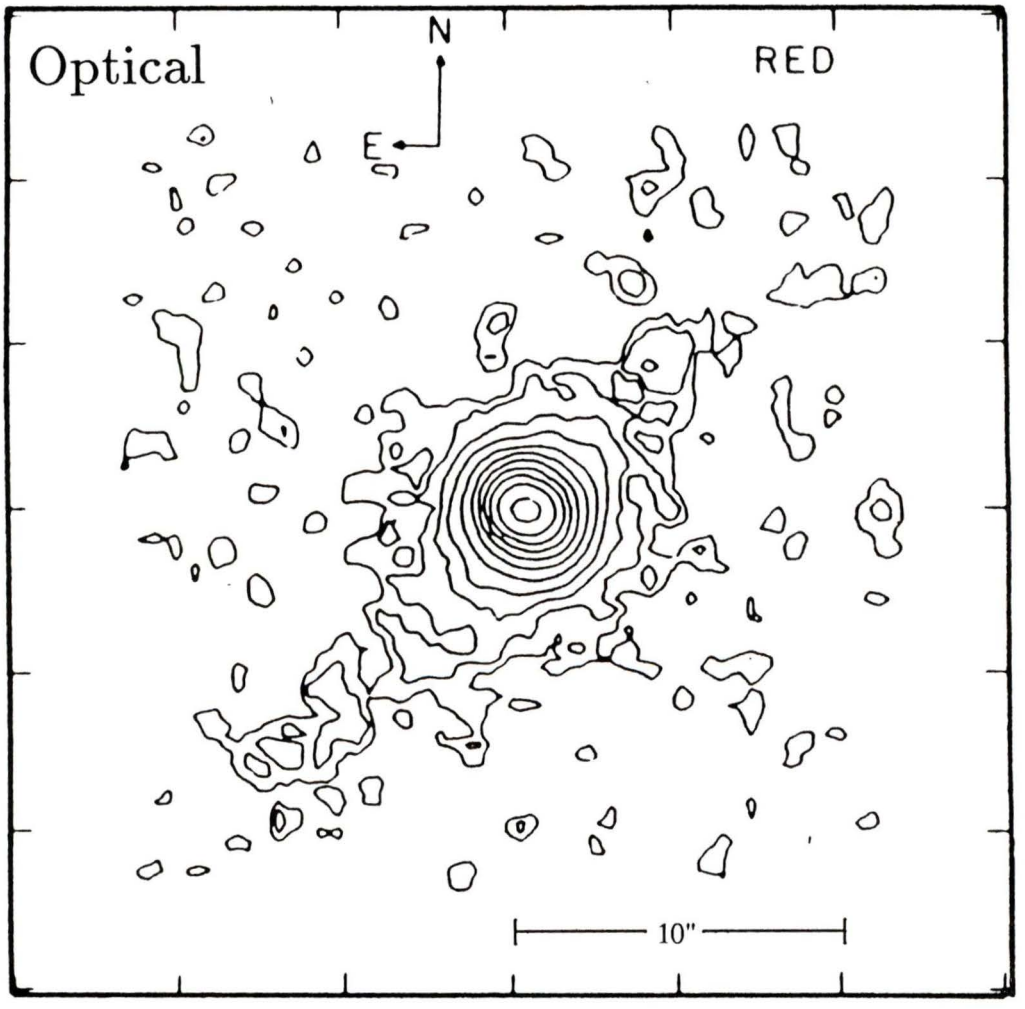

Optical image from Hutchings *et al.* (1984a)

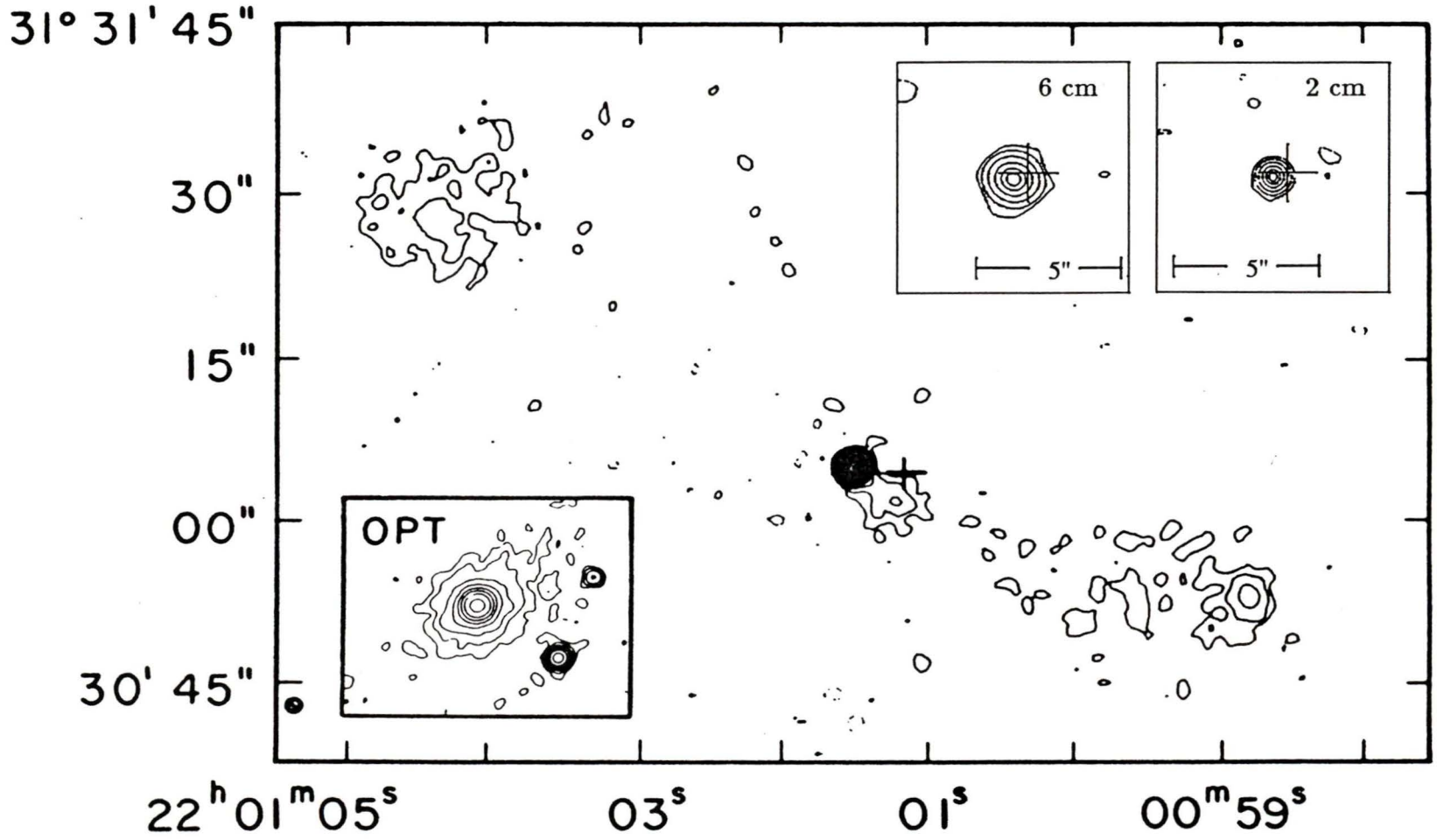

20 cm and optical images from Gower and Hutchings (1984)

2217+087N

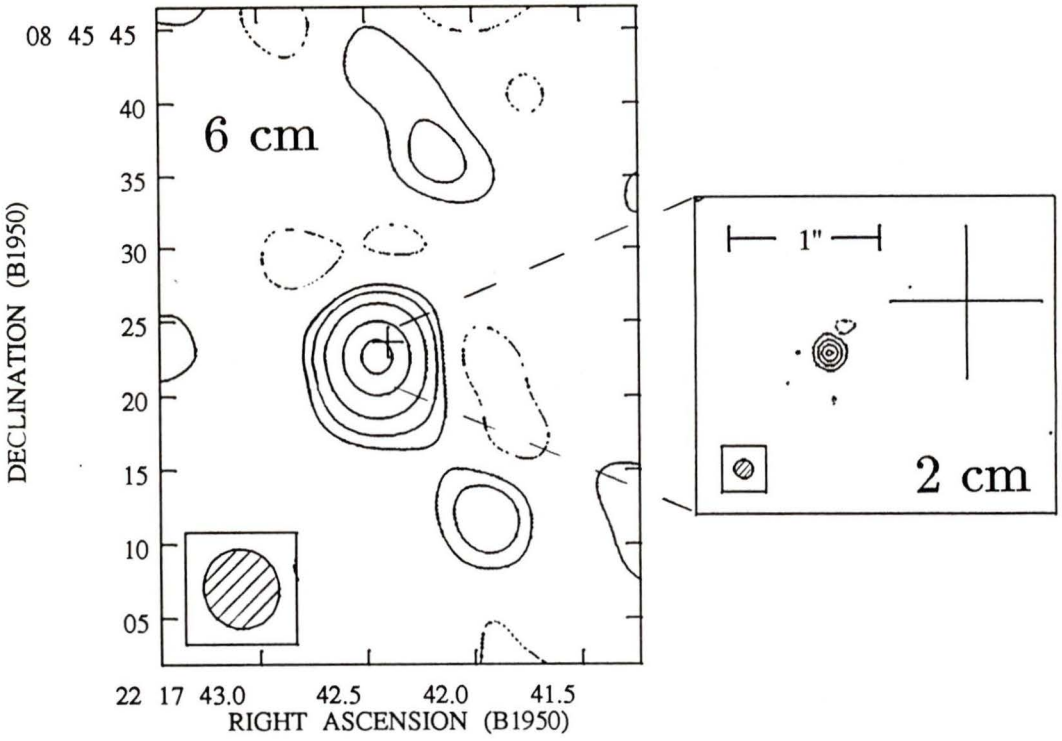

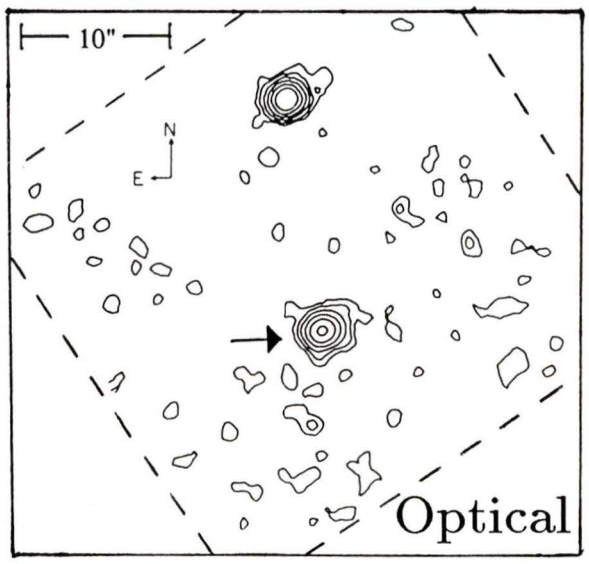

Optical image from Hutchings *et al.* (1984a)

2217+087S

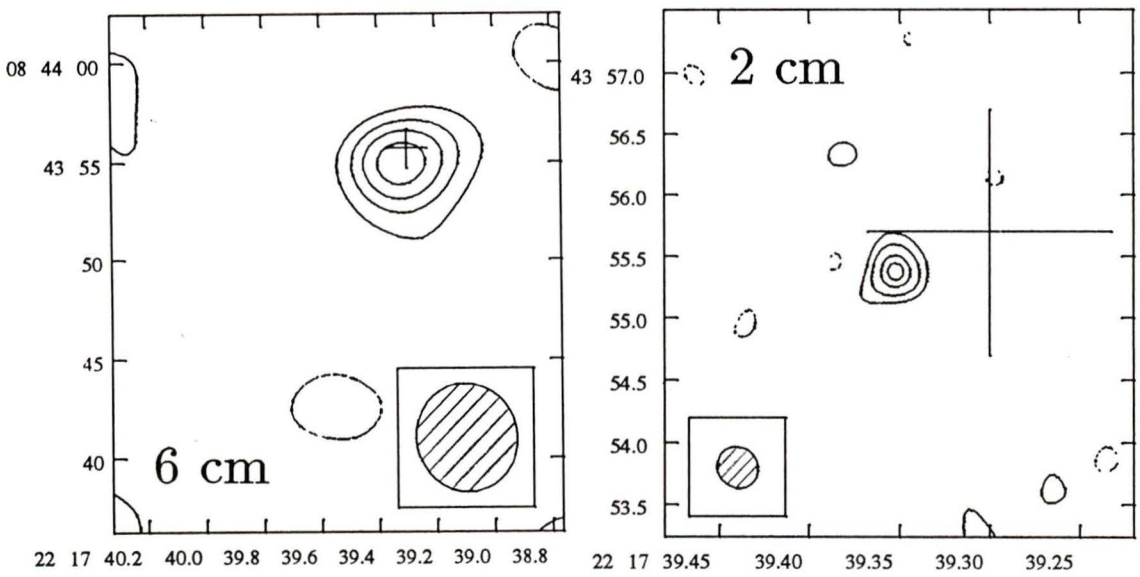

20 cm image from Harris *et al.* (1983)

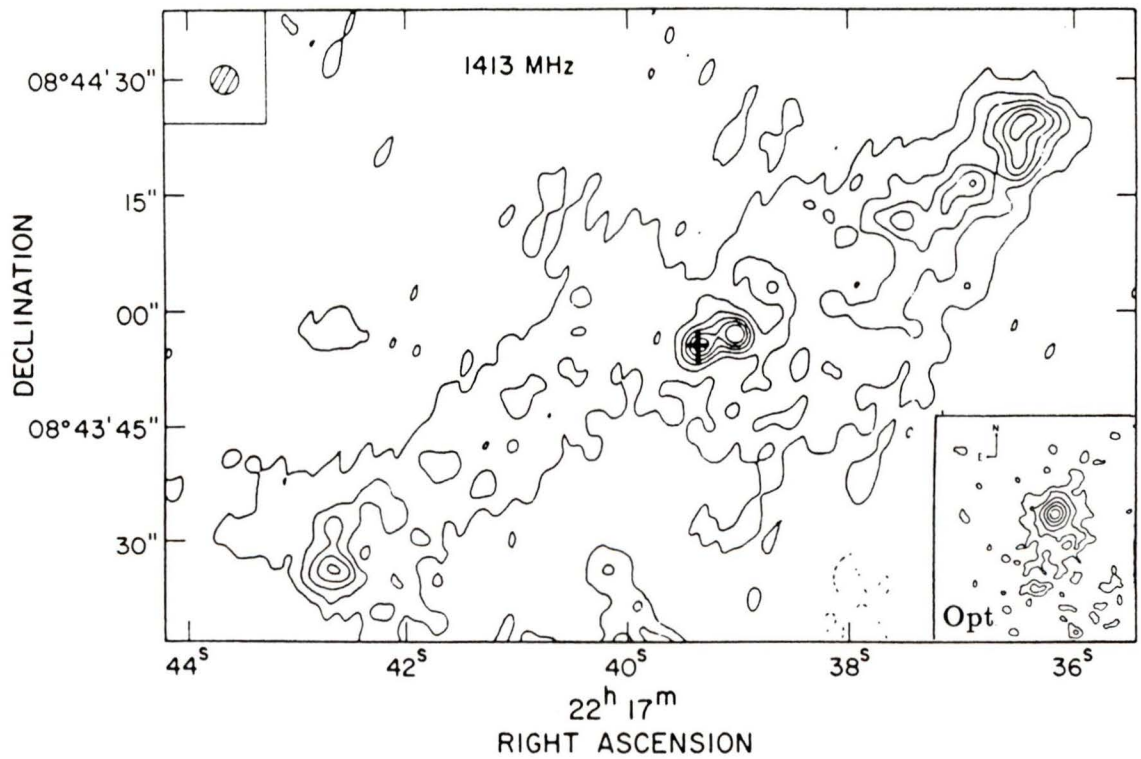

Optical image from Hutchings *et al.* (1984a)

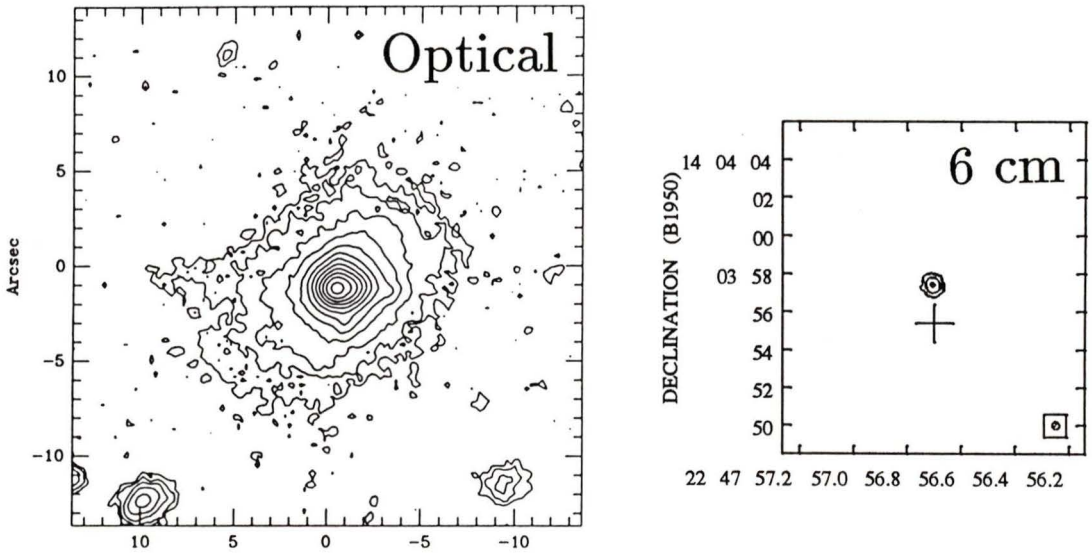

Optical image from Hutchings, Johnson and Pyke (1988)

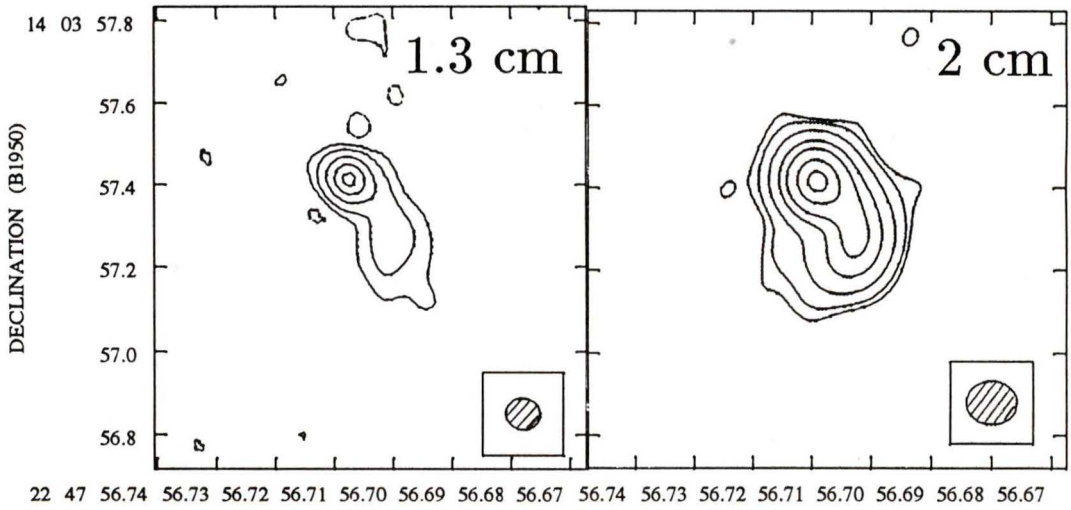

2305+187

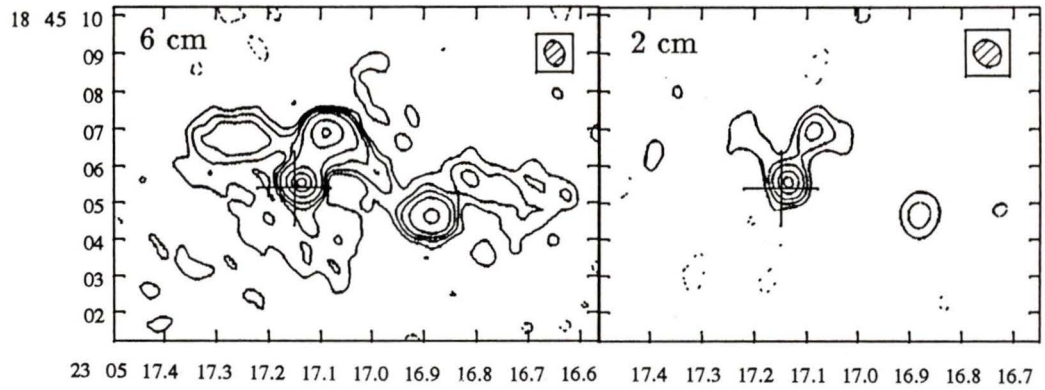

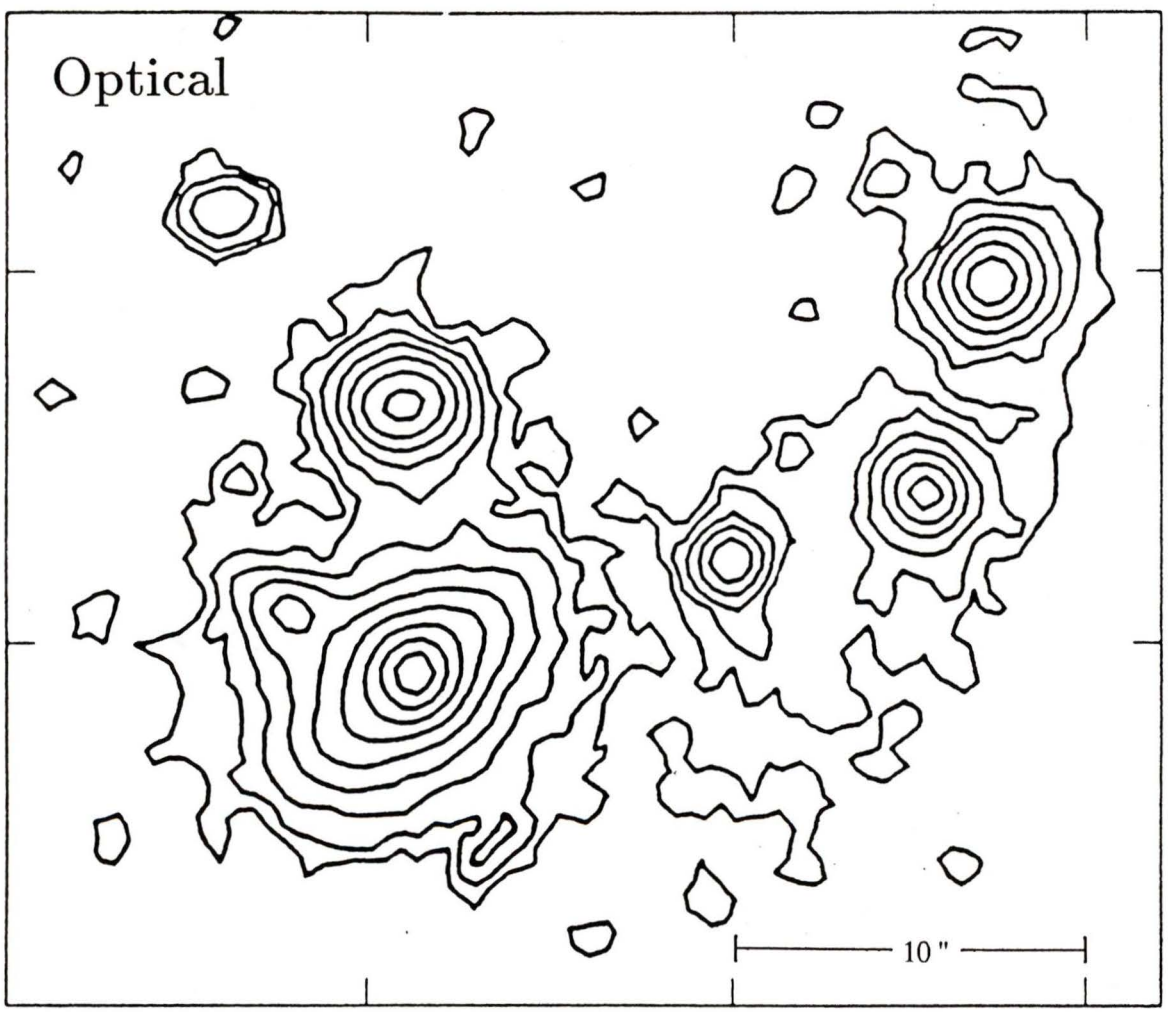

Optical image from Hutchings *et al.* (1992)

2328+167

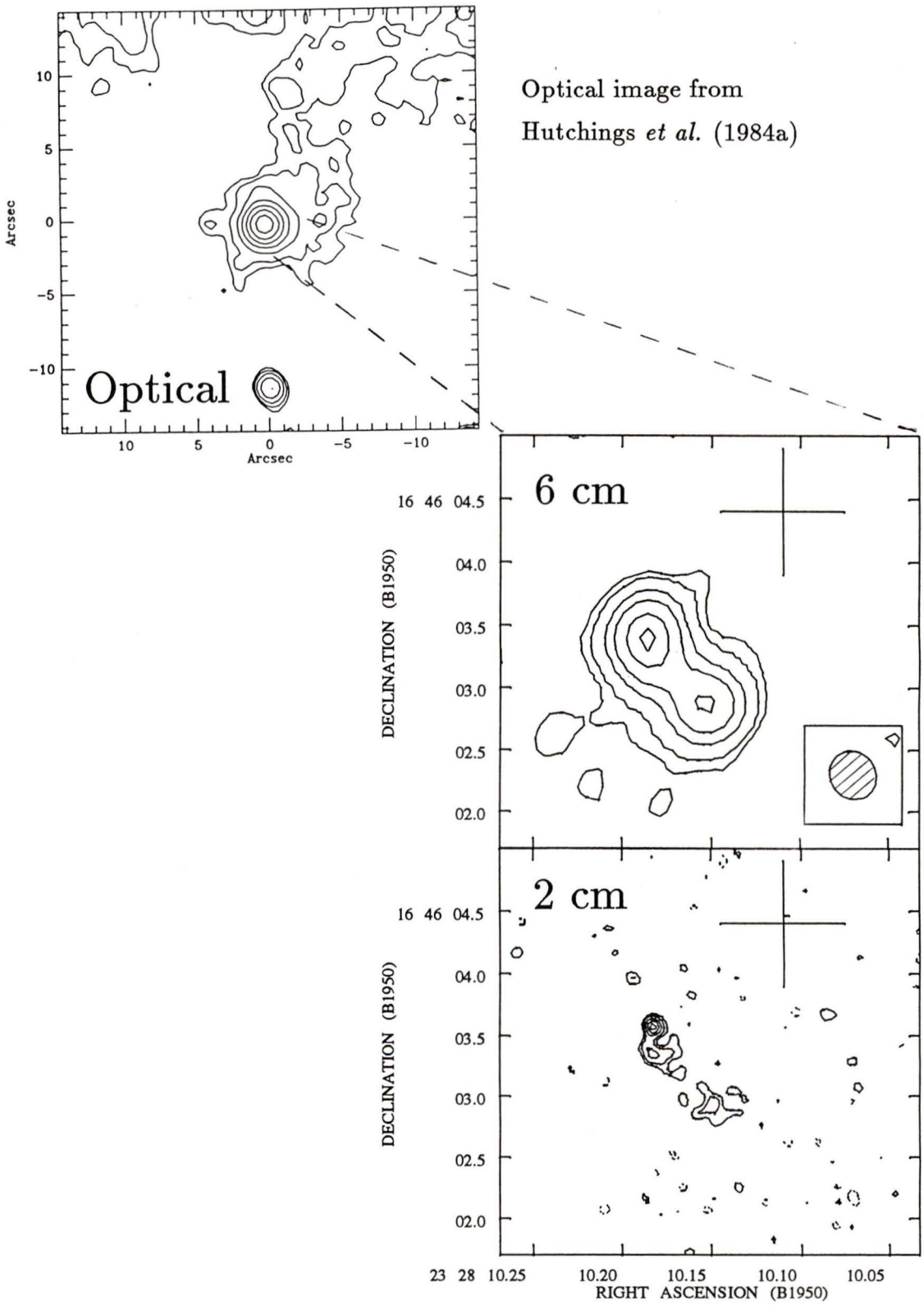
Optical
Arcsec
10
5
0
−5
−10
Optical image from
Hutchings *et al.* (1984a)
6 cm
2 cm
DECLINATION (B1950)
16 46 04.5
04.0
03.5
03.0
02.5
02.0
23 28 10.25
10.20
10.15
10.10
10.05
RIGHT ASCENSION (B1950)

2331-240

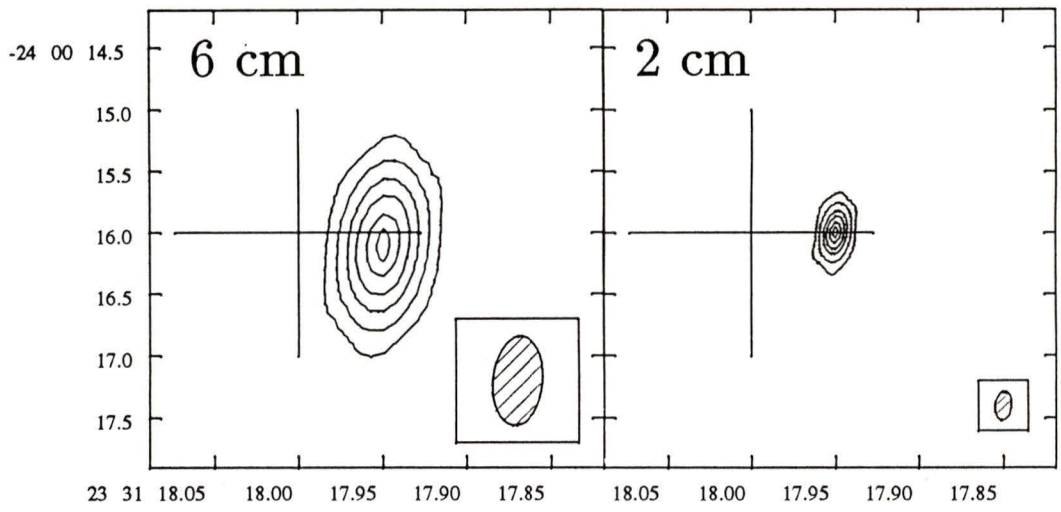

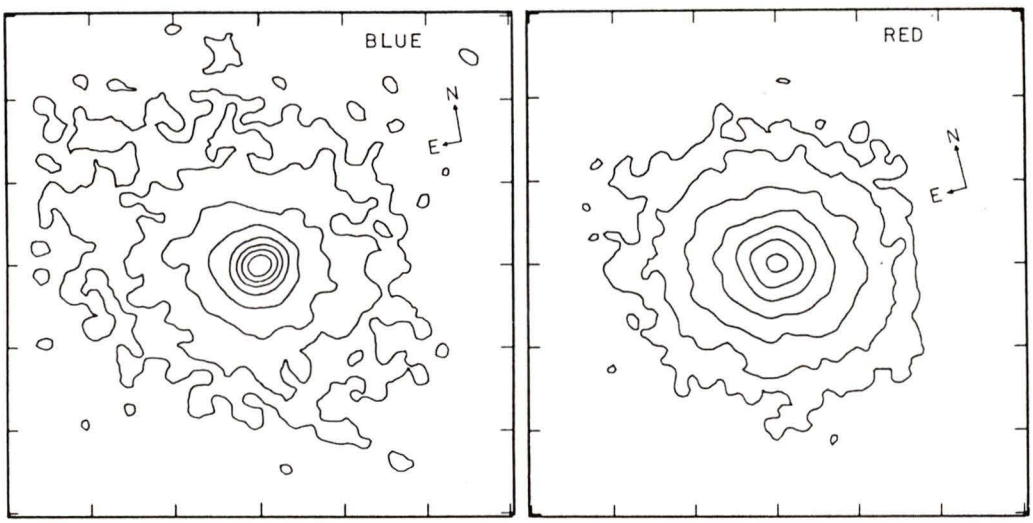

Optical images from Hutchings *et al.* (1984a)

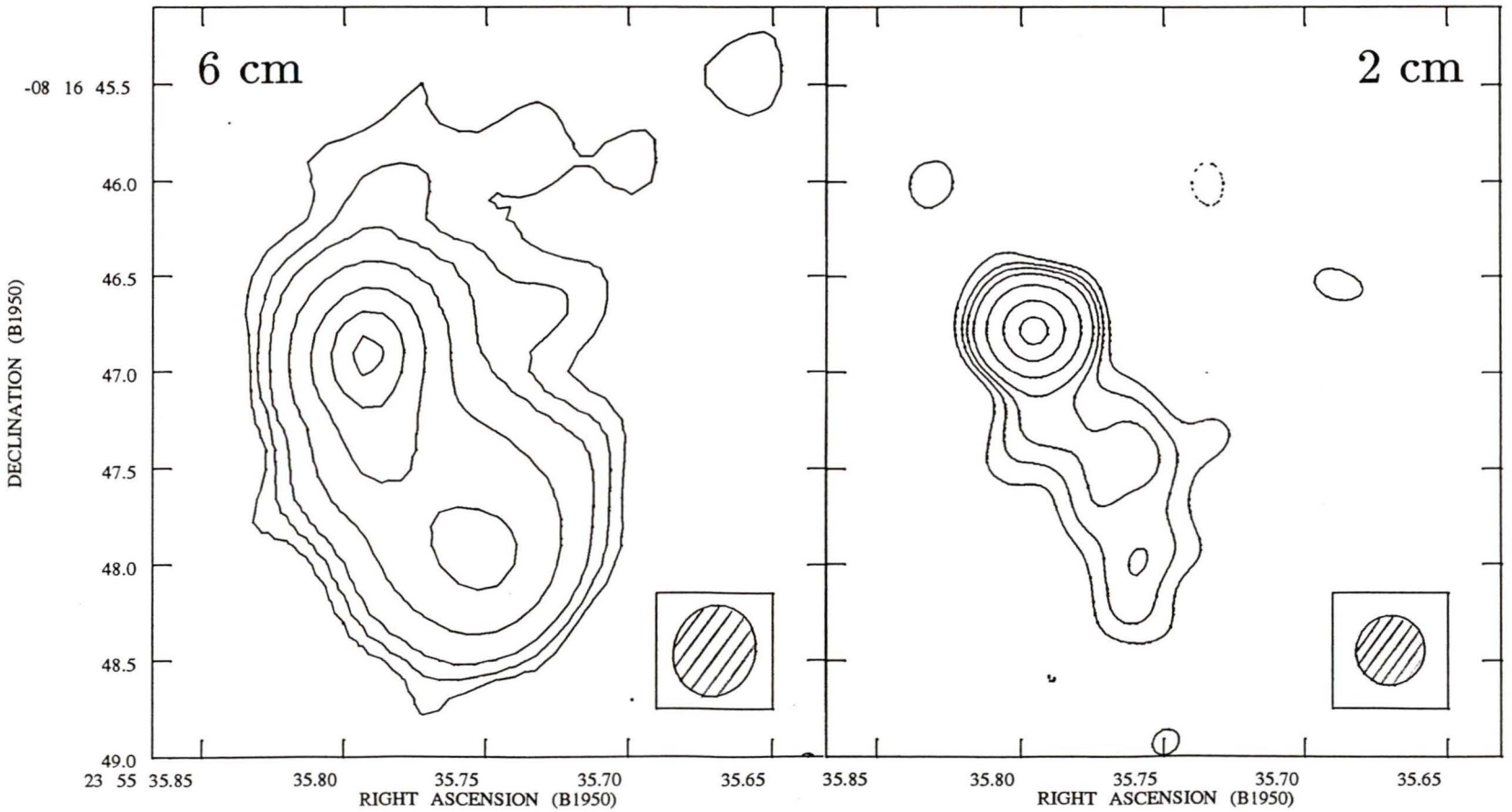
6 cm
2 cm
-08 16 45.5
46.0
46.5
47.0
47.5
48.0
48.5
49.0
DECLINATION (B1950)
23 55 35.85
35.80
35.75
35.70
35.65
RIGHT ASCENSION (B1950)

2355-082

Vita

Surname: **Lister** Given Names: **Matthew Leigh**

Place of Birth: **Ottawa, Ontario** Date of Birth: **October 25, 1969**

Educational Institutions Attended:

University of Toronto, Toronto, Ontario **1987 to 1991**

University of Victoria, Victoria , British Columbia **1991 to 1993**

Degrees Awarded:

B.Sc. in Physics and Astronomy, Magna Cum Laude, University of Toronto **1991**

Honours and Awards:

The 5T8 Scholarship, Trinity College, University of Toronto **1987**

College Scholarship, Trinity College, University of Toronto **1988**

Faculty Scholar, University of Toronto **1988**

NSERC Undergraduate Research Award **1989, 1990**

PARTIAL COPYRIGHT LICENSE

I hereby grant the right to lend my thesis to users of the University of Victoria Library, and to make single copies only for such users or in response to a request from the Library of any other university, or similar institution, on its behalf or for one of its users. I further agree that permission for extensive copying of this thesis for scholarly purposes may be granted by me or a member of the University designated by me. It is understood that copying or publication of this thesis for financial gain shall not be allowed without my written permission.

Title of Thesis:

Second-Epoch, High-Resolution Observations of a Low-Redshift Radio Quasar Sample

Author: **Matthew Leigh Lister**

May 31, 1993